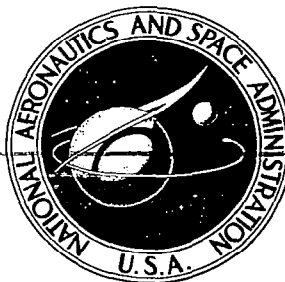




NASA CR-71



LOAN COPY: RETURN TO
AFWL (DOUL)
KIRTLAND AFB, N. M.

NASA CONTRACTOR REPORT

NASA CR-2103

CALCULATIVE TECHNIQUES FOR TRANSONIC FLOWS ABOUT CERTAIN CLASSES OF WING-BODY COMBINATIONS

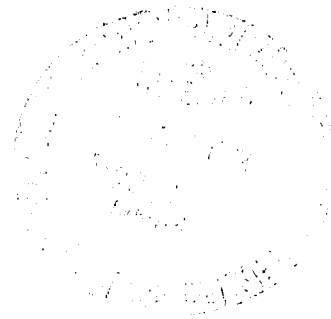
by Stephen S. Stahara and John R. Spreiter

Prepared by

NIELSEN ENGINEERING & RESEARCH, INC.

Mountain View, Calif. 94040

for Ames Research Center



NATIONAL AERONAUTICS AND SPACE ADMINISTRATION • WASHINGTON, D. C. • AUGUST 1972



0061184

1. Report No. NASA CR-2103		2. Government Accession No.		3. Recipient's Catalog No.	
4. Title and Subtitle "Calculative Techniques for Transonic Flows About Certain Classes of Wing-Body Combinations"				5. Report Date August 1972	
				6. Performing Organization Code	
7. Author(s) Stephen S. Stahara and John R. Spreiter				8. Performing Organization Report No.	
9. Performing Organization Name and Address Nielsen Engineering and Research, Inc. 850 Maude Avenue Mountain View, California 94040				10. Work Unit No.	
				11. Contract or Grant No. NAS 2-6259	
12. Sponsoring Agency Name and Address National Aeronautics & Space Administration Washington, D.C.				13. Type of Report and Period Covered Contractor Report	
				14. Sponsoring Agency Code	
15. Supplementary Notes					
16. Abstract Procedures based on the method of local linearization and transonic equivalence rule were developed for predicting properties of transonic flows about certain classes of wing-body combinations. The procedures are applicable to transonic flows with free stream Mach number in the ranges near one, below the lower critical and above the upper critical. Theoretical results are presented for surface and flow field pressure distributions for both lifting and nonlifting situations.					
17. Key Words (Suggested by Author(s)) Transonic Flow Aerodynamics Wing-Body Combinations Transonic Equivalence Rule Local Linearization				18. Distribution Statement UNCLASSIFIED - UNLIMITED	
19. Security Classif. (of this report) UNCLASSIFIED		20. Security Classif. (of this page) UNCLASSIFIED		21. No. of Pages 98	
				22. Price* 3.00	

TABLE OF CONTENTS

	<u>Page No.</u>
SUMMARY	1
INTRODUCTION	1
LIST OF SYMBOLS	4
ANALYSIS	9
General Considerations	9
Transonic Equivalence Rule	10
Local Linearization Method	11
Wing and Body Geometry	13
Finite Thickness Wing Circular-Body Combinations	14
Thickness problem	15
Lifting problem	23
Aerodynamic characteristics	24
Finite Thickness Wing Elliptic-Body Combinations	29
Thickness problem	29
Lifting problem	41
Aerodynamic characteristics	44
Bumpy and Indented Bodies	47
RESULTS AND DISCUSSION	53
Wing-Body Combinations	53
Bumpy and Indented Bodies	59
CONCLUDING REMARKS	68
REFERENCES	71
FIGURES	75

CALCULATIVE TECHNIQUES FOR TRANSONIC FLOWS
ABOUT CERTAIN CLASSES OF WING-BODY COMBINATIONS

By Stephen S. Stahara and John R. Spreiter*
Nielsen Engineering & Research, Inc.

SUMMARY

Theoretical analysis and the development of associated computer programs were carried out for the purpose of developing computational techniques for predicting properties of transonic flows about certain classes of wing-body combinations. The procedures used are based on the method of local linearization and the transonic equivalence rule and apply to transonic flows with free-stream Mach number in the ranges close to one, below the lower critical, and above the upper critical. Theoretical results are presented for surface and flow field pressure distributions for certain members of the general classes of configurations studied, for both nonlifting and lifting situations, at $M_\infty = 1$ and also at Mach numbers below the lower critical and above the upper critical.

In addition, consideration was given to developing methods for calculating flows about bodies having a bump or indentation superimposed upon an otherwise smooth profile. The results indicate that a quasi-cylindrical theory is necessary to predict accurately transonic flows about these shapes.

The computational programs developed under this report are documented and available under separate cover in a general user's manual.

INTRODUCTION

Until recently, the basic difficulty of solving the nonlinear and mixed elliptic-hyperbolic equations of transonic aerodynamics combined with the low level of interest given problems characteristic to this flight regime had resulted in little substantial advance in the

*Professor, Departments of Applied Mechanics and Aeronautics and Astronautics, Stanford University, Stanford, California. (Consultant at Nielsen Engineering & Research, Inc.).

solving of practical problems in this important area (refs. 1 and 2). However, within the past few years, the attention given to problems concerned with transonic flight has produced some encouraging results.

For example, the results of reference 3 clearly demonstrate that a theory (local linearization method) already exists that is capable of accounting for many of the properties of three-dimensional, lifting, transonic flows and that, when combined with modern computational techniques, provides aerodynamic information inexpensively and of sufficient accuracy to be of practical design use. Thus, while completely numerical studies of transonic flows will continue to improve as machine capability increases (the recent work of references 4, 5, and 6 concerning two-dimensional transonic flows, and the work of reference 7 for nonlifting axisymmetric flows provide a good indication of the current state-of-the-art), it appears that finite difference techniques for transonic flows about three-dimensional lifting configurations, such as the ones studied herein, remains a distinct (and expensive) future goal. Consequently, the parallel development of some of the already successful analytic techniques, in particular the local linearization method, is clearly warranted.

Because the analysis of three-dimensional, lifting, transonic flows (both analytical and numerical) has received scant attention--prior to the recent investigation by the present authors (ref. 3) there existed only one isolated example of an application and experimental evaluation of transonic theory to a nonaxisymmetric lifting flow at $M_\infty = 1$ (ref. 8)--the work of reference 3 provided for the first time an exhaustive systematic evaluation and comparison of theoretical and experimental results for transonic flows at $M_\infty \approx 1$ about several general classes of axisymmetric and nonaxisymmetric slender bodies, for both nonlifting and lifting situations. It confirmed in depth the initial conclusions of references 9 and 10 regarding the accuracy of the local linearization method as applied to slender axisymmetric shapes and, in addition, demonstrated the capability of the transonic equivalence rule (1) to account for change in flow properties on the surface of slender bodies due to moderate nonaxisymmetric effects of body shape and lift and (2) to predict transonic flow-field properties at field points removed by moderate lateral distances from the body surface. In addition, an application was made to two simple wing-body combinations (see figs. 20

and 21, ref. 3) having zero thickness wings in order to demonstrate the present capability of these techniques.

The current study extends the work of reference 3 to include several general classes of more complex wing-body combinations, in which the wings have finite thickness and the bodies are area-rule indented so that the resultant equivalent bodies remain smooth. Both the axisymmetric and nonaxisymmetric body shapes studied in reference 3 are considered. In addition, axisymmetric shapes having bumpy and indented midsections are studied in order to assess the applicability of the method to finite thickness wing-circular body combinations for which the actual body is smooth but the equivalent body is bumpy.

While the ultimate goal of the present investigation is to develop computational techniques for the prediction of the flow field, pressure distribution, and aerodynamic characteristics of three-dimensional, lifting, wing-body combinations, the purposes of this study are (1) to apply the local linearization method together with the transonic equivalence rule to various classes of wing-body combinations for which the equivalent body is smooth in order to examine the effectiveness of the theory to these classes of shapes, and (2) to apply these same techniques to axisymmetric shapes having bumps (or indentations) in order to assess their applicability to finite thickness wing-smooth body combinations for which the equivalent body is bumpy.

LIST OF SYMBOLS

a	major axis of elliptic cross section of indented parabolic-arc body
a _{sb}	major axis of elliptic cross section of smooth (non-indented) parabolic-arc body
AR	aspect ratio
b	minor axis of elliptic cross section of indented parabolic-arc body
c	equal to $\sqrt{a^2 - b^2}$
c _w	wing chord
C	Euler's constant
C _{D_{eb}}	drag coefficient of equivalent body of revolution, $D_{eb}/q_{\infty}S_m$ eq. (44)
C _{D_t}	total drag coefficient, $D_t/q_{\infty}S_m$
C _{D_{α=0}}	drag coefficient at zero lift, $D_{α=0}/q_{\infty}S_m$
C _L	lift coefficient, $L/q_{\infty}S_m$
C _p	pressure coefficient, $(p - p_{\infty})/\frac{1}{2}\rho_{\infty}U_{\infty}^2$
C _{p_{eb}}	pressure coefficient due to equivalent body of revolution
C _m	pitching moment coefficient about nose, $M_y/q_{\infty}S_m\ell$ (positive nose-up)
D	maximum diameter of equivalent body of revolution
D _{eb}	drag of equivalent body of revolution
D _i	drag due to lift
D _t	total drag
D _{α=0}	total drag at zero lift
F	source distribution on wing of wing-elliptic body combination
g	quantity defined by eq. (6)

$\hat{i}, \hat{j}, \hat{k}$	unit vectors parallel to the x, y, z axes
J_m	Bessel function of first kind of order m
k	equal to $M_\infty^2(\gamma + 1)/U_\infty$
K	complete elliptic integral of first kind
K_m	modified Bessel function of second kind of order m
l	body length
L	lift
m	exponent describing wing ordinates, eqs. (16), (17)
$M_{cr, l}$	lower critical Mach number on equivalent body of revolution
$M_{cr, u}$	upper critical Mach number on equivalent body of revolution
M_y	pitching moment about nose, positive nose-up
M_∞	free-stream Mach number
n	exponent describing equivalent body ordinates and related to location of point of maximum thickness, eqs. (12), (13), (14), (15)
n_1, n_2, n_3	direction cosines with respect to x, y, z axes
p_∞	free-stream pressure
q_1, q_2, q_3 q_4, q_5, q_6	quantities defined by eqs. (71), (72), (73)
q_∞	free-stream dynamic pressure
r	radial distance in crossflow plane, $\sqrt{y^2 + z^2}$
r_c	radius of cylinder
r_o	radius of axisymmetric distortion on cylindrical surface
R	radius of body of revolution
R_b	radius of indented body of revolution
R_{eb}	radius of equivalent body of revolution
R_1	radius of circular body in transformed (σ_1) plane, eq. (62)
\bar{R}	radius of the basic body of a bumpy or indented body of revolution

s	seimspan of wing
s_1	semispan of wing in transformed (σ_1) plane, eq. (63)
S	area distribution of body of revolution
S_b	area distribution of indented body of revolution
S_{eb}	area distribution of equivalent body of revolution
S_m	maximum area distribution of equivalent body of revolution, $\pi D^2/4$
\bar{S}	area distribution of the basic body of a bumpy or indented body of revolution
t	maximum thickness of wing profile
u, v, w	perturbation velocity components parallel to the x, y, z axes, respectively
u_B, v_B, w_B	perturbation velocity components associated with solution for transonic flow about equivalent body of revolution
u_ℓ	linearized longitudinal perturbation velocity component
u_s	longitudinal perturbation velocity component on the surface of a slender body of revolution
$u_{2,B}, v_{2,B}, w_{2,B}$	perturbation velocity components associated with two-dimensional incompressible solution of expansion or contraction of equivalent cross section in cross-flow plane
$u_{2,t}, v_{2,t}, w_{2,t}$	perturbation velocity components associated with two-dimensional incompressible solution of expanding or contracting cross section in crossflow plane
$u_{2,\alpha}, v_{2,\alpha}, w_{2,\alpha}$	perturbation velocity components associated with two-dimensional incompressible solution of translating cross section in crossflow plane
U_∞	free-stream velocity
\underline{V}	total velocity vector
$W_{2,t}$	complex potential describing two-dimensional incompressible flow about expanding or contracting cross section in crossflow plane
$W_{2,\alpha}$	complex potential describing two-dimensional incompressible flow about translating cross section in crossflow plane
$W_{2,\alpha}^{(1)}$	complex potential describing two-dimensional incompressible flow about translating cross section in crossflow plane having zero normal velocity at surface

x, y, z	body-fixed Cartesian coordinate system with x axis direction rearward and aligned with longitudinal axis of body, y axis directed to the right facing forward, and z axis directed vertically upward
x_s	location of point closest to origin where $S''(x) = 0$
x_1	axial location of start of bump or indentation eq. (99)
x_2	axial location of end of bump or indentation eq. (99)
x_b	axial location of body base
x_{rle}	axial location of wing leading edge root chord
x_{rle_1}	axial location of point where wing leading edge pierces body surface
x_{rte}	axial location of wing trailing-edge root chord
x_{rte_1}	axial location of point where wing trailing edge pierces body surface
x_{sm}	axial location of the point of maximum span
\bar{x}	axial distance from wing leading edge
\bar{y}	lateral distance from wing leading edge
z_w	wing ordinates, eqs. (16), (17)
α	angle of attack
β	quantity defined by $\sqrt{M_\infty^2 - 1 + ku}$
β_l	quantity defined by $\sqrt{M_\infty^2 - 1}$
β_{le}	wing leading-edge sweep angle
β_{te}	wing trailing-edge sweep angle
γ	ratio of specific heats
ΔR	increment of radius due to a bump or indentation of a body of revolution
ΔR_{max}	maximum value of ΔR
ΔS	incremental area distribution due to the bump or indentation of a body of revolution

θ	polar angle in crossflow plane
λ	ratio of major to minor axes of elliptic cross section, a/b
ξ, ξ_1	dummy variables
ρ_∞	free-stream density
σ	complex variable in crossflow plane, $y + iz$
σ_1	complex variable in transformed crossflow plane, $y_1 + iz_1$
τ_{eb}	thickness ratio of equivalent body of revolution, D/ℓ
τ_w	thickness-to-chord ratio of wing, eqs. (16), (17)
ϕ	perturbation velocity potential
ϕ_B	perturbation velocity potential associated with transonic flow about equivalent body of revolution
ϕ_2	perturbation velocity potential associated with two-dimensional incompressible solutions to translation and growth of cross section in crossflow plane
$\phi_{2,B}$	perturbation velocity potential associated with two-dimensional incompressible solution for expansion or contraction of equivalent cross section in crossflow plane
$\phi_{2,t}$	perturbation velocity potential associated with two-dimensional incompressible solution for expansion or contraction of cross section in crossflow plane
$\phi_{2,\alpha}$	perturbation velocity potential associated with two-dimensional incompressible solution for translation of cross section in crossflow plane
Φ	total velocity potential
$\psi_{2,\alpha}$	perturbation stream function associated with two-dimensional incompressible solution for translation of cross section in crossflow plane

ANALYSIS

General Considerations

For all of the three-dimensional flows considered herein, the analysis presented is expressed in terms of a body-fixed Cartesian coordinate system centered at the nose with the x -axis directed rearward and aligned with the longitudinal axis of the body, the y -axis directed to the right facing forward, and the z -axis directed vertically upward so that the x - z plane is a plane of symmetry of the body and in the case of a wing-body combination, is perpendicular to the plane of the wing, as shown in figure 1. For lifting situations, the free-stream direction is taken to be inclined at any arbitrary small angle α to the x axis but confined to the x - z plane so that there is no side-slip. With the assumption that the configurations under consideration are such that the resulting flows can be adequately treated within the framework of inviscid small disturbance theory, the velocity \mathbf{V} can be expressed as the gradient of a potential Φ which may, in turn, be related to a perturbation velocity potential ϕ according to (ref. 11)

$$\Phi(x, y, z) = U_{\infty}(x + \alpha z) + \phi(x, y, z) \quad (1)$$

where U_{∞} represents the free-stream velocity, and α the angle of attack. The governing partial differential equation for ϕ is given by

$$(1 - M_{\infty}^2)\phi_{xx} + \phi_{yy} + \phi_{zz} = \frac{M_{\infty}^2(\gamma + 1)}{U_{\infty}} \phi_x \phi_{xx} \quad (2)$$

and is invariant with respect to small rotations of the coordinate system. Consequently, the differential equation applies whether the x -axis is parallel to the direction of the free stream, as in most derivations (refs. 12, 13), or inclined a small angle to it as in the present applications to lifting configurations. The expression for the pressure coefficient C_p is not invariant and in the above reference frame is given (ref. 11)

$$C_p = \frac{p - p_{\infty}}{\frac{1}{2} \rho_{\infty} U_{\infty}^2} = - \frac{2}{U_{\infty}} (\phi_x + \alpha \phi_z) - \frac{1}{U_{\infty}^2} (\phi_y^2 + \phi_z^2) \quad (3)$$

The boundary conditions require that

$$\underline{V} = iU_{\infty} + k\alpha U_{\infty} \quad (4)$$

far from the body, where i , j , and k are unit vectors parallel to the x , y , and z axes, and that the velocity component V_n normal to the configuration be zero at the surface. Thus, the boundary conditions for the perturbation potential ϕ for configurations consisting of slender bodies and thin wings are (ref. 11)

$$\left. \begin{aligned} \phi(\infty) &= 0 \\ \left[U_{\infty}(n_1 + \alpha n_3) + \phi_n \right]_{\text{surface}} &= 0 \end{aligned} \right\} \quad (5)$$

where $\hat{n} = \hat{i}n_1 + \hat{j}n_2 + \hat{k}n_3$ is the unit normal to the surface and n_1 , n_2 , and n_3 are the direction cosines of \hat{n} with respect to the x , y , and z axes.

Transonic Equivalence Rule

The transonic equivalence rule first proposed by Oswatitsch (ref. 14) for flows past thin nonlifting wings, and later extended to lifting wings (ref. 15) and slender wing-body combinations of arbitrary cross section (ref. 11) provides an important means for studying a complex transonic flow by reducing it to a number of component flows more easily evaluated. The rule was used with great success in reference 3 and will be briefly described here. For more details, references 3, 11, 14, and 15 should be consulted. Specifically, the rule relates the transonic flow around a slender configuration of general cross section to that past an "equivalent" nonlifting body of revolution having the same distribution of cross sectional area. Figure 1 summarizes the theoretical essentials of the equivalence rule and also indicates one of the more important results of slender body theory which states that in the neighborhood of a slender body the perturbation potential ϕ is approximately of the form

$$\phi = \phi_2(x, y, z) + g(x) \quad (6)$$

where ϕ_2 is the solution of Laplace's equation

$$(\phi_2)_{yy} + (\phi_2)_{zz} = 0 \quad (7)$$

for the given boundary conditions in the yz plane at each x station, and $g(x)$ is an additional contribution dependent upon M_∞ and $S(x)$ but not on the shape of the cross section. It is thus possible to determine $g(x)$ from the solution of the simpler problem of nonlifting axisymmetric flow at the same M_∞ past the equivalent body.

It is convenient to express the equivalence rule mathematically as

$$\phi = \phi_{2,\alpha} + \phi_{2,t} - \phi_{2,B} + \phi_B \quad (8)$$

where $\phi_{2,\alpha}$, $\phi_{2,t}$, and $\phi_{2,B}$ are solutions of the two-dimensional Laplace equation as shown in figure 1. Hence, $\phi_{2,\alpha}$ is the two-dimensional incompressible flow solution for the translation of the cross section (lifting problem), $\phi_{2,t}$ the corresponding solution for expansion (or contraction) of the cross section (thickness problem), and $\phi_{2,B}$ the solution for the expansion (or contraction) of a circular cylinder having identical cross sectional area. Finally, ϕ_B is the three-dimensional solution to the full transonic equation for the equivalent body of revolution. The order of error inherent in the equivalence rule has been established in reference 11 and it appears that the rule ought to be applicable to wings to greater aspect ratio at $M_\infty = 1$ than at any other Mach number.

With the solution for ϕ in hand, the pressure distribution on or near a slender body of arbitrary cross section is provided by equation (3). This result may be integrated to obtain the total forces, including lift and drag, and moments for these configurations. Since the aerodynamic loading, lift, and all lateral forces and moments are expressed in terms of differences in pressure between pairs of points at the same longitudinal station, these quantities depend only on ϕ_2 and not M_∞ , and therefore can be calculated by using linearized slender body theory even though $M_\infty = 1$ (ref. 3, 16, 17).

Local Linearization Method

The original derivation and application of the local linearization method to axisymmetric flows about slender bodies of revolution is described in references 9 and 10.

The more detailed and extensive application and experimental comparison of the method carried out in reference 3 reinforced those initial conclusions regarding the accuracy and versatility of this technique as applied to smooth slender bodies. As shown in reference 9, the method provides the following results for the perturbation velocity component u/U_∞ on the body surface. For purely subsonic flows

$$\frac{d}{dx} \left(\frac{u}{U_\infty} \right) = \frac{S'''(x)}{4\pi} \ln (1 - M_\infty^2 - ku) + \frac{d}{dx} \left[\frac{S''(x)}{4\pi} \ln \frac{S(x)}{4\pi x (\ell - x)} + \frac{1}{4\pi} \int_0^\ell \frac{S''(x) - S''(\xi)}{|x - \xi|} d\xi \right] \quad (9)$$

for purely supersonic flows

$$\frac{d}{dx} \left(\frac{u}{U_\infty} \right) = \frac{S'''(x)}{4\pi} \ln (M_\infty^2 - 1 + ku) + \frac{d}{dx} \left[\frac{S''(x)}{4\pi} \ln \frac{S(x)}{4\pi x^2} + \frac{1}{2\pi} \int_0^x \frac{S''(x) - S''(\xi)}{x - \xi} d\xi \right] \quad (10)$$

and for accelerating transonic flows with $M_\infty \approx 1$

$$\frac{d}{dx} \left(\frac{u}{U_\infty} \right) = \frac{S'(x)S''(x)}{4\pi S(x)} + \exp \left\{ \frac{4\pi}{S''(x)} \left[\frac{u}{U_\infty} + \frac{M_\infty^2 - 1}{M_\infty^2(\gamma + 1)} - \frac{S''(x)}{4\pi} \ln \frac{M_\infty^2(\gamma + 1)S(x)e^C}{4\pi x} - \frac{1}{4\pi} \int_0^x \frac{S''(x) - S''(\xi)}{x - \xi} d\xi \right] \right\} \quad (11)$$

where k in equations (9) and (10) is equal to $M_\infty^2(\gamma + 1)/U_\infty$, C in equation (11) is Euler's constant ≈ 0.5772 , $S(x)$ represents the area distribution, and primes indicate differentiation with respect to the appropriate variable. These differential equations have been programmed for rapid computation in reference 3 where all details regarding starting conditions, numerical techniques, accuracy, limitations, etc. are provided.

Wing and Body Geometry

Because experimental verification of the theory was considered essential, primary attention was directed in reference 3 toward shapes for which data (refs. 18, 19, 20) was available.

Consequently, all of the axisymmetric bodies, or in the case of nonaxisymmetric bodies, the "equivalent" bodies of revolution considered in reference 3 have profiles described by the equations

$$\frac{R}{\ell} = \frac{\tau_{eb} n^{n/(n-1)}}{2(n-1)} \left[\frac{x}{\ell} - \left(\frac{x}{\ell} \right)^n \right] \quad (12)$$

$$\left(\frac{x}{\ell} \right)_{R_{\max}} = \left(\frac{1}{n} \right)^{1/(n-1)} \quad (13)$$

$$\frac{R}{\ell} = \frac{\tau_{eb} n^{n/(n-1)}}{2(n-1)} \left[1 - \frac{x}{\ell} - \left(1 - \frac{x}{\ell} \right)^n \right] \quad (14)$$

$$\left(\frac{x}{\ell} \right)_{R_{\max}} = 1 - \left(\frac{1}{n} \right)^{1/(n-1)} \quad (15)$$

with $n = \text{constant} \geq 2$. Since the theory and the computer programs developed in reference 3 are used as a starting point for the present work, the classes of wing-body combinations examined in this report consist of bodies indented at the wing junction so that the total cross sectional area distribution (i.e., body plus the wing) remains identical to that of smooth bodies having the profiles described above. Therefore, the wing-body combinations considered herein are composed of indented bodies derived from the two basic types of smooth body shapes, i.e.

- Bodies of revolution having $R \sim x/\ell - (x/\ell)^n$ or $1 - x/\ell - (1 - x/\ell)^n$
- Parabolic-arc bodies having elliptic cross sections which maintain a constant ratio $\lambda (= a/b)$ of major/minor axes along the entire body length

These classes of body shapes are illustrated in figures 2 and 3 on typical wing-body combinations together with the general class of wings to be studied. The wing planform consists of symmetric straight leading and trailing edges, swept at arbitrary angles β_{le} and β_{te} respectively, to the y axis. The positions of the leading and trailing edges of the wing root-chord are at arbitrary locations X_{rle} and X_{rte} along the body axis. The wing profiles are taken to be of the same class as the airfoils studied in references 3 and 21 so that in terms of the local chord, c_w , and the distance from the leading edge, \bar{x} , they are represented by expressions of the form

$$\frac{z_w}{c_w} = \frac{\tau_w^{m(m/m-1)}}{2(m-1)} \left(\frac{\bar{x}}{c_w} - \left(\frac{\bar{x}}{c_w} \right)^m \right) \quad (16)$$

or

$$\frac{z_w}{c_w} = \frac{\tau_w^{m(m/m-1)}}{2(m-1)} \left(1 - \frac{\bar{x}}{c_w} - \left(1 - \frac{\bar{x}}{c_w} \right)^m \right) \quad (17)$$

where m is a constant ≥ 2 . In addition, the wings are assumed to maintain a constant thickness-to-chord ratio across the span, with the consequence that the wing profiles at all spanwise locations are geometrically similar.

Finite Thickness Wing Circular-Body Combinations

The ingredients necessary to solve, by using the method of local linearization and the transonic equivalence rule, lifting transonic flows past wing-body combinations having the above classes of bodies are:

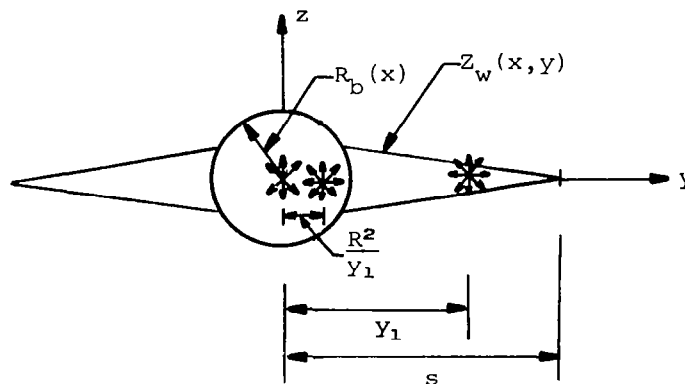
1. Solution of the two-dimensional Laplace equation describing growth of the cross section.
2. Solution of the two-dimensional Laplace equation describing translation of the cross section.
3. Solution of the two-dimensional Laplace equation describing growth of the equivalent area circular cylinder.
4. Solution of the nonlinear transonic equation for nonlifting flow past the equivalent body of revolution.

The solution of item (3) is represented by a two-dimensional source located on the x -axis whose strength is related to the first derivative of the equivalent area distribution. Thus,

$$\phi_{2,B} = \frac{U_{\infty} S'_{eb}(x)}{2\pi} \ln r \quad (18)$$

Since the previously developed computational programs (ref. 3) provide the local linearization solutions for ϕ_B (item 3), it remains to calculate $\phi_{2,t}$ (item 1) and $\phi_{2,\alpha}$ (item 2) for the particular wing-body configurations described above.

Thickness problem.— While no previous theoretical work is available on the thickness problem for finite thickness wing-body combinations at transonic speeds, the work of references 22, 23, and 24 concerned with supersonic slender-body flow is, nonetheless, applicable to the present problem. In particular, the method developed by Stocker (ref. 24) is most directly related to this study. That technique is based upon the method of singularities and models the wing thickness by placing a continuous distribution of two-dimensional incompressible sources (or sinks) along the wing chordal plane together with their appropriate images within the circular cylinder. The body is, of course, represented by a source (or sink) at the origin.



The method is a powerful one and applicable to a wide range of configurations. It provides the following expression for the complex potential $W_{2,t}(x,y,z)$:

$$\frac{w_{2,t}}{U_\infty} = \frac{1}{\pi} \int_{R_b}^S \frac{dz_w(x,\xi)}{dx} \ln \left[\frac{(\sigma^2 - \xi^2)(\sigma^2 - \frac{R_b^4}{\xi^2})}{\sigma^2} \right] d\xi + \frac{S'_b(x)}{2\pi} \ln \sigma \quad (19)$$

where σ is the complex variable in the crossflow plane

$$\sigma = y + iz \quad (20)$$

$S'_b(x)$ is the first derivative of the cross sectional area $S_b(x)$ of the body, i.e.

$$S_b(x) = \pi R_b^2(x) \quad (21)$$

and $\frac{dz_w(x,y)}{dx}$ is the first derivative in the longitudinal direction of the wing ordinates $Z_w(x,y)$. Since the equivalent body area distribution and the actual body area distribution are related through the expression

$$S_{eb}(x) = S_b(x) + 4 \int_{R_b}^S Z_w(x,y) dy \quad (22)$$

we can write the alternate form

$$\begin{aligned} \frac{w_{2,t}}{U_\infty} = \frac{1}{\pi} \int_{R_b}^S \frac{dZ_w(x,\xi)}{dx} \ln \left[\frac{(\sigma^2 - \xi^2)(\sigma^2 - \frac{R_b^4}{\xi^2})}{\sigma^4} \right] d\xi \\ + \frac{1}{2\pi} \left[S'_{eb}(x) + 4 Z_w(x, R_b) \frac{dR_b}{dx} \right] \ln \sigma \end{aligned} \quad (23)$$

The velocity components associated with this flow are given by

$$u_{2,t} = \frac{\partial \phi_{2,t}}{\partial x} = \text{R.P.} \frac{\partial w_{2,t}}{\partial x} \quad (24)$$

$$(v - iw)_{2,t} = \frac{dw_{2,t}}{d\sigma} \quad (25)$$

where $\phi_{2,t}$ represents the velocity potential and R.P. signifies the real part of a complex function.

Although the above expression for $w_{2,t}$ is quite compact, the resulting expressions for the velocity components are not. Because the evaluation of each velocity component generally involves the determination of at least one integral, care must be taken to assure proper treatment of the familiar Cauchy singularity that appears on the wing surface in several of these integrals. In addition to those singularities, the junction of the wing and body also requires special treatment since at those points the velocity components are continuous but their derivatives are not.

It is convenient to restrict attention to points located in the first quadrant of the crossflow plane ($y \geq 0, z \geq 0$) since from the assumed symmetry of the wing-body configurations we have

$$\left. \begin{aligned} u_{2,t}(x, -y, z) &= u_{2,t}(x, y, z) \\ v_{2,t}(x, -y, z) &= -v_{2,t}(x, y, z) \\ w_{2,t}(x, -y, z) &= w_{2,t}(x, y, z) \end{aligned} \right\} \quad (26)$$

and

$$\left. \begin{aligned} u_{2,t}(x, y, -z) &= u_{2,t}(x, y, z) \\ v_{2,t}(x, y, -z) &= v_{2,t}(x, y, z) \\ w_{2,t}(x, y, -z) &= -w_{2,t}(x, y, z) \end{aligned} \right\} \quad (27)$$

With this in mind, the following results are provided by equations (23), (24), and (25).

For a point at any general location but not on the wing surface,

$$\begin{aligned}
\frac{u_{z,t}}{U_\infty} &= \frac{1}{2\pi} \left(\int_{R_b}^s \frac{d^2 Z_w(x, \xi)}{dx^2} \times \right. \\
&\quad \ln \left\{ \frac{[z^2 + (y - \xi)^2] [z^2 + (y + \xi)^2] [z^2 + (y - \frac{R_b^2}{\xi})^2] [z^2 + (y + \frac{R_b^2}{\xi})^2]}{(z^2 + y^2)^4} \right\} d\xi \\
&\quad + 4R_b \frac{dR_b}{dx} \int_{R_b}^s \frac{dZ_w(x, \xi)}{dx} \frac{1}{\xi} \left[\frac{y + \frac{R_b^2}{\xi}}{z^2 + (y + \frac{R_b^2}{\xi})^2} - \frac{y - \frac{R_b^2}{\xi}}{z^2 + (y - \frac{R_b^2}{\xi})^2} \right] d\xi \\
&\quad + \frac{dZ_w(x, s)}{dx} \frac{ds}{dx} \times \\
&\quad \ln \left\{ \frac{[z^2 + (y - s)^2] [z^2 + (y + s)^2] [z^2 + (y - \frac{R_b^2}{s})^2] [z^2 + (y + \frac{R_b^2}{s})^2]}{(z^2 + y^2)^4} \right\} \\
&\quad - 2 \frac{dZ_w(x, R_b)}{dx} \frac{dR_b}{dx} \ln \left\{ \frac{[z^2 + (y - R_b)^2] [z^2 + (y + R_b)^2]}{(z^2 + y^2)^2} \right\} \\
&\quad + \left\{ \frac{S''_{eb}(x)}{2} + 2 \left[\left(\frac{dZ_w(x, R_b)}{dx} + \frac{dZ_w(x, R_b)}{dy} \frac{dR_b}{dx} \right) \frac{dR_b}{dx} \right. \right. \\
&\quad \left. \left. + Z_w(x, R_b) \frac{d^2 R_b}{dx^2} \right] \right\} \ln (z^2 + y^2) \Bigg) \quad (28)
\end{aligned}$$

$$\begin{aligned}
\frac{v_{2,t}}{U_\infty} = \frac{1}{\pi} \left\{ \int_{R_b}^s \frac{dZ_w(x, \xi)}{dx} \left[\frac{y - \xi}{z^2 + (y - \xi)^2} + \frac{y + \xi}{z^2 + (y + \xi)^2} + \frac{y - \frac{R_b^2}{\xi}}{z^2 + (y - \frac{R_b^2}{\xi})^2} \right. \right. \\
\left. \left. + \frac{y + \frac{R_b^2}{\xi}}{z^2 + (y + \frac{R_b^2}{\xi})^2} \right] d\xi + \frac{y}{z^2 + y^2} \left(-4 \int_{R_b}^s \frac{dZ_w(x, \xi)}{dx} d\xi + \frac{S'_{eb}(x)}{2} \right. \right. \\
\left. \left. + 2 Z_w(x, R_b) \frac{dR_b}{dx} \right) \right\} \quad (29)
\end{aligned}$$

$$\begin{aligned}
\frac{w_{2,t}}{U_\infty} = \frac{1}{\pi} \left\{ z \int_{R_b}^s \frac{dZ_w(x, \xi)}{dx} \left[\frac{1}{z^2 + (y - z)^2} + \frac{1}{z^2 + (y + \xi)^2} + \frac{1}{z^2 + (y - \frac{R_b^2}{\xi})^2} \right. \right. \\
\left. \left. + \frac{1}{z^2 + (y + \frac{R_b^2}{\xi})^2} \right] d\xi + \frac{z}{z^2 + y^2} \left(-4 \int_{R_b}^s \frac{dZ_w(x, \xi)}{dx} d\xi + \frac{S'_{eb}(x)}{2} \right. \right. \\
\left. \left. + 2 Z_w(x, R_b) \frac{dR_b}{dx} \right) \right\} \quad (30)
\end{aligned}$$

For points on the wing surface but not at the wing-body junction,
i.e. $z = 0$, and $R_b < y < s$:

$$\begin{aligned}
\frac{u_{2,t}}{U_\infty} = \frac{1}{2\pi} \left\{ \int_{R_b}^s \frac{d^2 Z_w(x, \xi)}{dx^2} \ln \left[\frac{(y + \xi)^2 (y + \frac{R_b^2}{\xi})^2}{y^4} \right] d\xi \right. \\
\left. + \int_{R_b}^s \left(\frac{d^2 Z_w(x, \xi)}{dx^2} - \frac{d^2 Z_w(x, y)}{dx^2} \right) \ln \left[\left(\frac{y - \xi}{y} \right)^2 \right] d\xi \right\}
\end{aligned}$$

(Continued on next page)

$$\begin{aligned}
& + \int_{R_b}^s \left(\frac{d^2 Z_w(x, \xi)}{dx^2} - \frac{d^2 Z_w(x, R_b)}{dx^2} \right) \ln \left[\left(\frac{y - \frac{R_b^2}{\xi}}{y} \right)^2 \right] d\xi \\
& + 4 R_b \frac{dR_b}{dx} \frac{1}{y} \left[\int_{R_b}^s \frac{\frac{dZ_w(x, \xi)}{dx}}{\xi + \frac{R_b^2}{y}} d\xi - \int_{R_b}^s \frac{\left(\frac{dZ_w(x, \xi)}{dx} - \frac{dZ_w(x, R_b)}{dx} \right)}{z - \frac{R_b^2}{y}} d\xi \right. \\
& \quad \left. - \frac{dZ_w(x, R_b)}{dx} \ln \left(\frac{s - \frac{R_b^2}{y}}{R_b - \frac{R_b^2}{y}} \right) \right] \\
& + 2 \frac{d^2 Z_w(x, y)}{dx^2} \left\{ (s - y) \left[\ln \left(\frac{s - y}{y} \right) - 1 \right] + (y - R_b) \left[\ln \left(\frac{y - R_b}{y} \right) - 1 \right] \right\} \\
& + 2 \frac{d^2 Z_w(x, R_b)}{dx^2} \left[s \ln \left(\frac{s - \frac{R_b^2}{y}}{s} \right) - R_b \ln \left(\frac{R_b - \frac{R_b^2}{y}}{R_b} \right) - \frac{R_b^2}{y} \ln \left(\frac{s - \frac{R_b^2}{y}}{R_b - \frac{R_b^2}{y}} \right) \right] \\
& + \frac{dZ_w(x, s)}{dx} \frac{ds}{dx} \ln \left[\frac{(s - y)^2 (s + y)^2 (y - \frac{R_b^2}{s})^2 (y + \frac{R_b^2}{s})^2}{y^8} \right] \\
& - 2 \frac{dZ_w(x, R_b)}{dx} \frac{dR_b}{dx} \ln \left[\frac{(y - R_b)^2 (y + R_b)^2}{y^4} \right] \\
& + \left\{ \frac{S''_{eb}(x)}{2} + 2 \left[\left(\frac{dZ_w(x, R_b)}{dx} + \frac{dZ_w(x, R_b)}{dy} \frac{dR_b}{dx} \right) + Z_w(x, R_b) \frac{d^2 R_b}{dx^2} \right] \right\} \ln(y^2) \Bigg\}
\end{aligned}$$

(31)

$$\begin{aligned}
\frac{v_{2,t}}{U_\infty} = & \frac{1}{\pi} \left[\int_{R_b}^s \frac{dZ_w(x,\xi)}{dx} \left(\frac{1}{y+\xi} + \frac{1}{y + \frac{R_b^2}{\xi}} \right) d\xi \right. \\
& - \int_{R_b}^s \frac{\left(\frac{dZ_w(x,\xi)}{dx} - \frac{dZ_w(x,y)}{dx} \right)}{\xi - y} d\xi + \frac{1}{y} \int_{R_b}^s \frac{\xi \left(\frac{dZ_w(x,\xi)}{dx} - \frac{dZ_w(x,R_b)}{dx} \right)}{\xi - \frac{R_b^2}{y}} d\xi \\
& - \frac{dZ_w(x,y)}{dx} \ln \left(\frac{s-y}{y-R_b} \right) + \frac{1}{y} \frac{dZ_w(x,R_b)}{dx} \left[s - R_b + \frac{R_b^2}{y} \ln \left(\frac{s - \frac{R_b^2}{y}}{R_b - \frac{R_b^2}{y}} \right) \right] \\
& \left. + \frac{1}{y} \left(-4 \int_{R_b}^s \frac{dZ_w(x,\xi)}{dx} + \frac{S'_{eb}(x)}{2} + 2 Z_w(x,R_b) \frac{dR_b}{dx} \right) \right] \quad (32)
\end{aligned}$$

$$\frac{w_{2,t}}{U_\infty} = \frac{dZ_w(x,y)}{dx} \quad (33)$$

And for points along the wing-body junction, i.e. $z = 0$, $y = R_b$

$$\begin{aligned}
\frac{u_{2,t}}{U_\infty} = & \frac{1}{2\pi} \left\{ \int_{R_b}^s \frac{d^2 Z_w(x,\xi)}{dx^2} \ln \left[\frac{(R_b + \xi)^2 (R_b + \frac{R_b^2}{\xi})^2}{R_b^4} \right] d\xi \right. \\
& + \int_{R_b}^s \left(\frac{d^2 Z_w(x,\xi)}{dx^2} - \frac{d^2 Z_w(x,R_b)}{dx^2} \right) \ln \left[\left(\frac{R_b - \xi}{R_b} \right)^2 \right] d\xi \\
& \left. + \int_{R_b}^s \left(\frac{d^2 Z_w(x,\xi)}{dx^2} - \frac{d^2 Z_w(x,R_b)}{dx^2} \right) \ln \left[\left(\frac{R_b - \frac{R_b^2}{\xi}}{R_b} \right)^2 \right] d\xi \right\}
\end{aligned}$$

(Continued on next page)

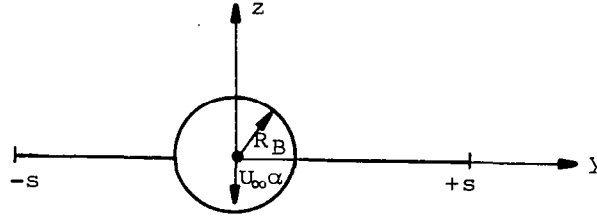
$$\begin{aligned}
& + 4 \frac{dR_b}{dx} \left[\int_{R_b}^s \frac{\frac{dZ_w(x, \xi)}{dx}}{\xi + R_b} - \int_{R_b}^s \frac{\left(\frac{dZ_w(x, \xi)}{dx} - \frac{dZ_w(x, R_b)}{dx} \right)}{\xi - R_b} d\xi \right] \\
& + 2 \frac{d^2 Z_w(x, R_b)}{dx^2} \left\{ (s - R_b) \left[\ln \left(\frac{s - R_b}{R_b} \right) - 1 \right] \right. \\
& + s \ln \left(\frac{s - R_b}{s} \right) - R_b \ln \left(\frac{s - R_b}{R_b} \right) \left. \right\} \\
& - 4 \frac{dZ_w(x, R_b)}{dx} \frac{dR_b}{dx} \ln \left[\frac{2(s - R_b)}{R_b} \right] \\
& + \frac{dZ_w(x, s)}{dx} \frac{ds}{dx} \ln \left[\frac{(s - R_b)^2 (s + R_b)^2 (R_b - \frac{R_b^2}{s})^2 (R_b + \frac{R_b^2}{s})^2}{R_b^8} \right] \\
& + \left\{ \frac{S''_{eb}(x)}{2} + 2 \left[\left(\frac{dZ_w(x, R_b)}{dx} + \frac{dZ_w(x, R_b)}{dy} \frac{dR_b}{dx} \right) \frac{dR_b}{dx} \right. \right. \\
& + \left. \left. Z_w(x, R_b) \frac{d^2 R_b}{dx^2} \right] \ln(R_b^2) \right\} \quad (34)
\end{aligned}$$

$$\begin{aligned}
\frac{v_{2,t}}{U_\infty} &= \frac{1}{\pi} \left\{ \int_{R_b}^s \frac{dZ_w(x, \xi)}{dx} \left[\frac{1}{R_b + \xi} + \frac{1}{R_b + \frac{R_b^2}{\xi}} \right] d\xi \right. \\
& - \int_{R_b}^s \frac{\left(\frac{dZ_w(x, \xi)}{dx} - \frac{dZ_w(x, R_b)}{dx} \right)}{\xi - R_b} d\xi + \frac{1}{R_b} \int_{R_b}^s \xi \frac{\left(\frac{dZ_w(x, \xi)}{dx} - \frac{dZ_w(x, R_b)}{dx} \right)}{\xi - R_b} d\xi \\
& + \frac{dZ_w(x, R_b)}{dx} \left(\frac{s - R_b}{R_b} \right) \\
& + \left. \frac{1}{R_b} \left(-4 \int_{R_b}^s \frac{dZ_w(x, \xi)}{dx} d\xi + \frac{S'_{eb}(x)}{2} + 2 Z_w(x, R_b) \frac{dR_b}{dx} \right) \right\} \quad (35)
\end{aligned}$$

$$\frac{w_{2,t}}{U_\infty} = \frac{dZ_w(x, R_b)}{dx} \quad (36)$$

It is clear from these expressions that, except for the very simplest wing profile shapes, analytical evaluation of the thickness velocity components is not possible and numerical means must be resorted to.

Lifting problem.— The cross flow problem for lifting flows at small angles of attack α about wing circular-body combinations has been studied previously, for example in references 25 and 26. The complex potential describing the downward translation at a constant rate $U_\infty \alpha$ of the wing circular-body cross section shown below



is given by

$$W_{2,\alpha} = -iU_\infty \alpha \left\{ \left[\left(\sigma + \frac{R_b^2}{\sigma} \right)^2 - \left(s + \frac{R_b^2}{s} \right)^2 \right]^{1/2} - \sigma \right\} \quad (37)$$

where it is assumed that the wing thickness is sufficiently small that the boundary condition on the wing surface can be satisfied on the y axis, i.e. at $z = 0$. The velocity components associated with this flow are found by operations similar to those used for the thickness problem. Thus,

$$\frac{u_{2,\alpha}}{U_\infty} = \text{R.P.} \left(-i\alpha \left\{ \frac{2 \left[\left(\sigma + \frac{R_b^2}{\sigma} \right) \frac{R_b}{\sigma} - \left(s + \frac{R_b^2}{s} \right) \frac{R_b}{s} \right] \frac{dR_b}{dx} - \left(s + \frac{R_b^2}{s} \right) \left(1 - \frac{R_b^2}{s^2} \right) \frac{ds}{dx}}{\left[\left(\sigma + \frac{R_b^2}{\sigma} \right)^2 - \left(s + \frac{R_b^2}{s} \right)^2 \right]^{1/2}} \right\} \right) \quad (38)$$

$$\frac{(v - iw)_{z,\alpha}}{U_\infty} = -i\alpha \left[\frac{(\sigma + \frac{R_b^2}{\sigma})(1 - \frac{R_b^2}{\sigma^2})}{\left[(\sigma + \frac{R_b^2}{\sigma})^2 - (s + \frac{R_b^2}{s})^2 \right]^{1/2}} - 1 \right] \quad (39)$$

where, unlike the thickness case, no distinction is necessary between a general point and points on the wing surface or at the wing-body junction since the velocity components contain no Cauchy singularities and are uniformly continuous at all points (except, of course, at the familiar square root singularity at the wing tip) in the flow field and at the solid boundaries. For these flows, the velocity components possess the following symmetries:

$$\begin{aligned} u_{2,\alpha}(x, -y, z) &= u_{2,\alpha}(x, y, z) \\ v_{2,\alpha}(x, -y, z) &= -v_{2,\alpha}(x, y, z) \\ w_{2,\alpha}(x, -y, z) &= w_{2,\alpha}(x, y, z) \end{aligned} \quad (40)$$

and

$$\begin{aligned} u_{2,\alpha}(x, y, -z) &= -u_{2,\alpha}(x, y, z) \\ v_{2,\alpha}(x, y, -z) &= -v_{2,\alpha}(x, y, z) \\ w_{2,\alpha}(x, y, -z) &= w_{2,\alpha}(x, y, z) \end{aligned} \quad (41)$$

Aerodynamic characteristics.— Because of the symmetry of the class of wing-body combinations considered herein, nonlifting flows produce no lateral forces or moments. Thus, the only force will be the longitudinal drag force which can be determined through the general formula,

$$D_{\alpha=0} = D_{eb} - \frac{\rho_\infty}{2} \left(\oint_{c_t} \phi_{2,t} \frac{\partial \phi_{2,t}}{\partial n} d\sigma_t - \oint_{c_B} \phi_{2,B} \frac{\partial \phi_{2,B}}{\partial n} d\sigma_B \right) \quad (42)$$

where D_{eb} represents the drag of the equivalent body while the other two terms involve the line integral along their respective contours (C_t is the contour defined by the cross section of the wing-body combination while C_B is the contour about the equivalent area circular cylinder) of the product of the appropriate velocity potential and the normal velocity associated with it. We note that the drag indicated by equation (42) refers to the inviscid drag of the configuration minus the base pressure drag. As pointed out in references 1, 2, 3, and 11, there exist many shapes of aerodynamic interest for which the two integrals involved cancel. In particular, we note that if the equivalent body and the original body have the same shape and surface slope at the base, as is the case for the configurations studied here, then since both integrals are carried out over the same contour along which $\phi_{2,t} = \phi_{2,B}$ and $\partial\phi_{2,t}/\partial n = \partial\phi_{2,B}/\partial n$, the integrals cancel and $D_{\alpha=0} = D_{eb}$. If we define a drag coefficient C_D based upon the maximum cross-sectional area of the equivalent body, S_m , we have for the body shapes described by equations 12 and 14 that

$$\frac{S_m}{\ell^2} = \frac{\pi \tau_{eb}^2}{4} \quad (43)$$

and so

$$C_{D_{eb}} = \frac{D_{eb}}{\frac{\rho_\infty}{2} U_\infty^2 S_m} = \frac{1}{S_m} \int_0^{X_b} C_{P_{eb}} S'_{eb}(x) dx \quad (44)$$

where $C_{P_{eb}}$ is defined by the formula

$$C_{P_{eb}} = -\frac{2u_B}{U_\infty} - \left(\frac{dR_{eb}(x)}{dx} \right)^2 \quad (45)$$

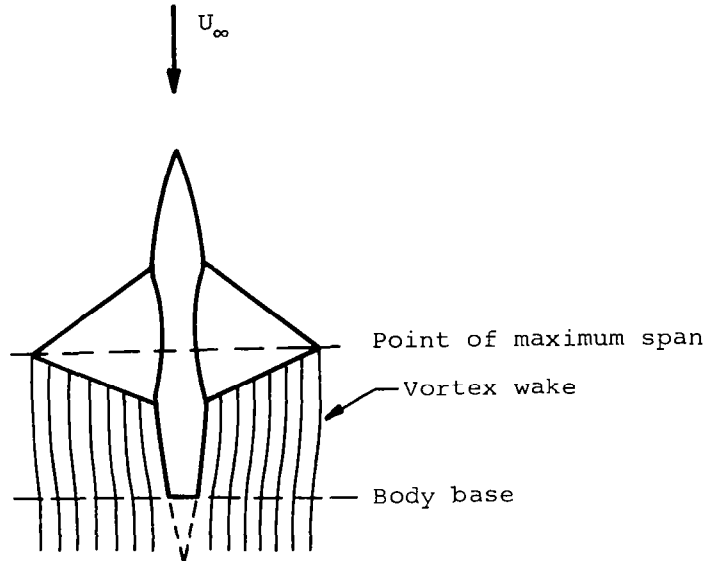
For the lifting situation, an exact analysis of the aerodynamic forces and moments, even within the framework of small disturbance theory, becomes quite formidable. The general formulas for determining the coefficients of lift, pitching moment, and drag are given by

$$C_L = \frac{L}{S_m q_\infty} \oint_C \phi_{2,\alpha} d\sigma_C \quad (46)$$

$$C_m = \frac{M_y}{q_\infty \cdot S_m \cdot \ell} = \frac{-1}{q_\infty \cdot S_m \cdot \ell} \int_0^x \xi \frac{dL(\xi)}{d\xi} d\xi \quad (47)$$

$$C_{D_t} = \frac{D_t}{q_\infty S_m} = \frac{D_{eb}}{q_\infty S_m} - \frac{1}{S_m U_\infty^2} \left(\oint_C \phi_{2,\alpha} \frac{\partial \phi_{2,\alpha}}{\partial n} d\sigma_C + \oint_C \phi_{2,t} \frac{\partial \phi_{2,t}}{\partial n} d\sigma_t - \oint_B \phi_{2,B} \frac{\partial \phi_{2,B}}{\partial n} d\sigma_B \right) \quad (48)$$

where now the contour C , while still taken at the base of the body, must now account for the vortex wake which springs from the wing trailing edge and, as before, the drag given by equation (48) represents the inviscid drag minus the base pressure drag. Because the vortex lines near the body surface must follow the streamlines of the flow around the body, the vortex wake will not proceed parallel to the x -axis, in general, as it does in many simpler cases considered in slender body theory; but will move away from or toward the body axis to follow the lateral expansion or contraction of the flow field near the body as shown below.



The resulting flow at the body base is influenced by the wake and, consequently, is no longer independent of the flow at cross sections preceding it. The solution of problems of this type, is discussed briefly in reference 27. In general, they are quite difficult to solve and since they are by no means unique to transonic slender body flows, their exact solution is clearly beyond the scope of the present investigation. Because the analysis presented here, however, remains valid up to the point of maximum span (i.e. as long as the edge of the wing remains a leading edge) a rough estimate can be made of these quantities by making the assumption that beyond the point of maximum span X_{sm} the vortex sheet remains parallel to the x -axis and does not vary with x . With this premise in mind, we can proceed to evaluate equation (46) for the lift by replacing $\phi_{2,\alpha}$ by $W_{2,\alpha}$, carrying out the complex integral along the cross section at $x = X_{sm}$, and then taking the real part of the result. Care must be exercised in carrying this out however, since as pointed out in reference 28 direct replacement of $\phi_{2,\alpha}$ by $W_{2,\alpha} = \phi_{2,\alpha} + i\psi_{2,\alpha}$, while reducing the problem to one of evaluating a closed contour complex integral, will generally lead to a spurious result unless the stream function $\psi_{2,\alpha}$ happens to be zero or a constant along the cross section contour.

This point seems to have been overlooked in references 29 and 30. Introduction of the potential $W_{2,\alpha}^{(1)}$ for the related flow having zero normal velocity at the contour and a velocity component at infinity proportional to the angle of attack avoids this problem. Thus,

$$\phi_{2,\alpha} = \text{R.P.} \left\{ W_{2,\alpha}^{(1)} \right\} - \alpha z U_\infty \quad (49)$$

where

$$W_{2,\alpha}^{(1)}(\sigma) = -iU_\infty \alpha \left[\left(\sigma + \frac{R_b^2}{\sigma} \right)^2 - \left(s + \frac{R_b^2}{s} \right)^2 \right]^{1/2} \quad (50)$$

Hence,

$$C_L = - \frac{2}{q_\infty S_m} \oint_C W_{2,\alpha}^{(1)} d\sigma_c - \frac{2\alpha}{S_m} \oint_C z d\sigma \quad (51)$$

These integrals are readily evaluated (see ref. 24 for details) providing the result that

$$C_L = \frac{2\pi\alpha}{S_m} \left[s^2 + \frac{R_b^4}{s^2} - \frac{1}{\pi} \left(S_b(x) + 4 \int_{R_b}^s Z_w(x, \xi) d\xi \right) \right] \Bigg|_{x = X_{sm}} \quad (52)$$

or by using equation (22),

$$C_L = \frac{2\pi\alpha}{S_m} \left(s^2 + \frac{R_b^4}{s^2} - R_{eb}^2 \right) \Bigg|_{x = X_{sm}} \quad (53)$$

With this result the pitching moment can be determined in a straight forward fashion. First, integrating equation (47) by parts, we have

$$C_m = \frac{1}{q_\infty \cdot S_m \cdot \ell} \left\{ -xL(x) \Big|_{x = X_{sm}} + \int_0^{X_{sm}} L(\xi) d\xi \right\} \quad (54)$$

or

$$C_m = \frac{2\pi\alpha}{S_m \cdot \ell} \left[-x \left(s^2 + \frac{R_b^4}{s^2} - R_{eb}^2 \right) \Bigg|_{x = X_{sm}} + \int_0^{X_{sm}} \left(s^2 + \frac{R_b^4}{s^2} - R_{eb}^2 \right) d\xi \right] \quad (55)$$

where it is understood in the integral that until the wing leading edge pierces the body surface, i.e. until $x = X_{rle_1}$ (see fig. 2), $s = R_b = R_{eb}$, so that

$$C_m = \frac{2\pi\alpha}{S_m \cdot \ell} \left[-x \left(s^2 + \frac{R_b^4}{s^2} - R_{eb}^2 \right) \Bigg|_{x = X_{sm}} + \int_0^{X_{rle_1}} R_{eb}^2 d\xi + \int_{X_{rle_1}}^{X_{sm}} \left(s^2 + \frac{R_b^4}{s^2} - R_{eb}^2 \right) d\xi \right] \quad (56)$$

As far as the drag is concerned, the first term in equation (48) is simply the induced vortex drag associated with lift and is given by (ref. 11)

$$D_i = \frac{\alpha}{2} L \quad (57)$$

Consequently, if the thickness and lifting drags can be considered independently we can use the result first stated by Ward (ref. 29) that

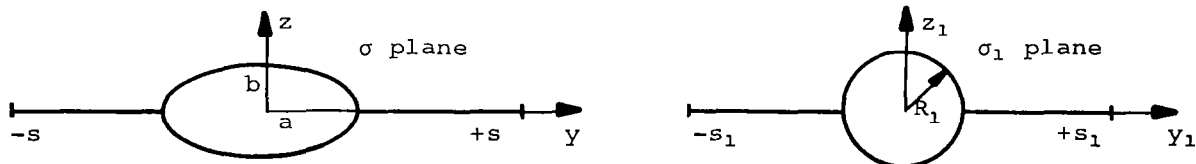
$$C_{D_t} = C_{D_{\alpha=0}} + \frac{\alpha}{2} C_L \quad (58)$$

where the drag coefficient at zero lift is given by equation (44).

Finite Thickness Wing Elliptic-Body Combinations

The analysis of wing-body combinations comprised of parabolic-arc bodies having indented elliptic cross sections such that the total cross sectional area distribution (i.e., body plus wing) equals the area of the original smooth body with elliptic cross section proceeds in a manner analogous to that of the circular body shapes. Because the solutions to the nonlinear transonic equation for nonlifting flow past the equivalent body of revolution and the two-dimensional Laplace equation describing growth of the equivalent area circular cylinder are again known, it remains to determine the potentials $W_{2,t}$ and $W_{2,\alpha}$ of the respective thickness and lifting problems. The most direct technique for determining these potentials consists of reducing the elliptic cross section to a circular one by use of an appropriate Joukowski transformation and then applying directly the preceding methods developed for the circular shapes.

Thickness problem.— The transformation of the elliptic cross section into a circular one is accomplished through the following relation;



$$\sigma_1 = \frac{1}{2} \left(\sigma + \sqrt{\sigma^2 - c^2} \right) \quad (59)$$

where

$$c^2 = a^2 - b^2 \quad (60)$$

and

$$\sigma_1 = y_1 + iz_1 \quad (61)$$

This takes the ellipse into a circle of radius

$$R_1 = \frac{(a + b)}{2} \quad (62)$$

and the semispan s into the shortened semispan

$$s_1 = \frac{s + \sqrt{s^2 - c^2}}{2} \quad (63)$$

Consequently, with reference to equation (19), we can write the complex thickness potential $w_{2,t}$ in the transformed σ_1 plane, as

$$\frac{w_{2,t}(\sigma_1)}{U_\infty} = \int_{R_1}^{s_1} F(\xi_1) \ln \left[\frac{(\sigma_1^2 - \xi_1^2)(\sigma_1^2 - \frac{R_1^4}{\xi_1^2})}{\sigma_1^2} \right] d\xi_1 + \frac{S'_b(x)}{2\pi} \ln \sigma_1 \quad (64)$$

where the source distribution $F(\xi_1)$ must be related to the boundary condition on the wing in the physical plane, i.e.

$$\frac{w_{2,t}(x,y,0)}{U_\infty} = \frac{dZ_w(x,y)}{dx} \quad a < y < s \quad (65)$$

Now since

$$\frac{(v - iw)_{2,t}}{U_\infty} = \frac{dw_{2,t}(\sigma_1)}{d\sigma_1} \frac{d\sigma_1}{d\sigma} \quad (66)$$

we have

$$\lim_{z \rightarrow 0} \left[- \text{I.P.} \left(\frac{dW_{2,t}(\sigma_1)}{d\sigma_1} \frac{d\sigma_1}{d\sigma} \right) \right] = \frac{dZ_w(x,y)}{dx} \quad a < y < s \quad (67)$$

Inserting equation (64) into equation (67), carrying through the indicated operations, and taking proper account of the Cauchy singularity we find that

$$F(\xi_1) = \frac{1}{\pi} \frac{dZ_w(x, \xi_1 + \frac{c^2}{4\xi_1^2})}{dx} \left(1 - \frac{c^2}{4\xi_1^2} \right) \quad (68)$$

Hence, by using equation (22) the expression for $W_{2,t}$ becomes

$$\begin{aligned} \frac{W_{2,t}(\sigma_1)}{U_\infty} &= \frac{1}{\pi} \int_{R_1}^{s_1} \frac{dZ_w(x, \xi_1 + \frac{c^2}{4\xi_1^2})}{dx} \ln \left[\frac{(\sigma_1^2 - \xi_1^2)(\sigma_1^2 - \frac{R_1^4}{\xi_1^2})}{\sigma_1^4} \right] \left(1 - \frac{c^2}{4\xi_1^2} \right) d\xi_1 \\ &+ \frac{1}{\pi} \left(\frac{S'_{eb}(x)}{2} + 2 Z_w(x, a) \frac{da}{dx} \right) \ln \sigma_1 \end{aligned} \quad (69)$$

Equation (69) could be now transformed back into physical variables; however, in evaluating the individual velocity components it is more convenient to retain the present expression.

The longitudinal velocity component of this flow is given by

$$u_{2,t} = \text{R.P.} \frac{\partial W_{2,t}}{\partial x} \quad (70)$$

and the lateral components by equation (66).

As before, the appearance of the Cauchy singularity on the wing surface, and the discontinuity of the derivatives of the velocity components at the wing-body junction require that separate treatment be given to these points. Because the symmetry properties stated by equations (26) and (27) remain valid for these shapes, we will restrict attention to points in the first quadrant of the crossflow plane.

If we define the following quantities

$$q_1 + iq_2 = \frac{1}{\sigma_1^2 - \frac{c^2}{4}} \quad (71)$$

$$q_3 + iq_4 = \frac{\sigma_1}{\sigma_1^2 - \frac{c^2}{4}} \quad (72)$$

$$q_5 + iq_6 = \frac{\sigma_1^2}{\sigma_1^2 - \frac{c^2}{4}} \quad (73)$$

then equations (66), (69), and (70) provide the following results. For a point at general location but not on the wing surface,

$$\begin{aligned} \frac{u_{2,t}}{U_\infty} = & \frac{1}{2\pi} \left(\int_{R_1}^{S_1} \frac{d^2 Z_w(x, \xi + \frac{c^2}{4\xi_1})}{dx^2} \times \right. \\ & \left. \ln \left\{ \frac{[z_1^2 + (y_1 - z_1)^2][z_1^2 + (y_1 + z_1)^2][z_1^2 + (y_1 - \frac{R_1^2}{\xi_1})^2][z_1^2 + (y_1 + \frac{R_1^2}{\xi_1})^2]}{(z_1^2 + y_1^2)^4} \right\} \times \right. \\ & \left. \left(1 - \frac{c^2}{4\xi_1^2}\right) d\xi_1 \right. \\ & + \left(\frac{\lambda^2 - 1}{\lambda^2} \right) a \frac{da}{dx} \left(-2 q_1 \int_a^S \frac{dZ_w(x, \xi)}{dx} d\xi \right. \\ & + \left(\frac{\lambda + 1}{\lambda - 1} \right) \left[-q_5 \int_{R_1}^{S_1} \frac{dZ_w(x, \xi_1 + \frac{c^2}{4\xi_1})}{dx} \frac{1}{\xi_1} \frac{(y_1 - \frac{R_1^2}{\xi_1})}{z_1^2 + (y_1 - \frac{R_1^2}{\xi_1})^2} d\xi_1 \right. \\ & \left. \left. - q_6 z_1 \int_{R_1}^{S_1} \frac{dZ_w(x, \xi_1 + \frac{c^2}{4\xi_1})}{dx} \frac{1}{\xi_1} \frac{d\xi_1}{z_1^2 + (y_1 - \frac{R_1^2}{\xi_1})^2} \right. \right. \end{aligned}$$

(Continued on next page)

$$\begin{aligned}
& + q_5 \int_{R_1}^{S_1} \frac{dZ_w(x, \xi_1 + \frac{c^2}{4\xi_1})}{dx} \frac{1}{\xi_1} \frac{Y_1 + \frac{R_1^2}{\xi_1}}{z_1^2 + (Y_1 + \frac{R_1^2}{\xi_1})^2} d\xi_1 \\
& + q_6 z_1 \int_{R_1}^{S_1} \frac{dZ_w(x, \xi_1 + \frac{c^2}{4\xi_1})}{dx} \frac{1}{\xi_1} \frac{d\xi_1}{z_1^2 + (Y_1 + \frac{R_1^2}{\xi_1})^2} \Bigg] \\
& + \frac{c^2}{4} \left[q_3 \int_{R_1}^{S_1} \frac{dZ_w(x, \xi_1 + \frac{c^2}{4\xi_1})}{dx} \frac{1}{\xi_1^2} \frac{(Y_1 - \frac{R_1^2}{\xi_1})}{z_1^2 + (Y_1 - \frac{R_1^2}{\xi_1})^2} d\xi_1 \right. \\
& + q_4 z_1 \int_{R_1}^{S_1} \frac{dZ_w(x, \xi_1 + \frac{c^2}{4\xi_1})}{dx} \frac{1}{\xi_1^2} \frac{d\xi_1}{z_1^2 + (Y_1 - \frac{R_1^2}{\xi_1})^2} \\
& + q_3 \int_{R_1}^{S_1} \frac{dZ_w(x, \xi_1 + \frac{c^2}{4\xi_1})}{dx} \frac{1}{\xi_1^2} \frac{(Y_1 + \frac{R_1^2}{\xi_1})}{z_1^2 + (Y_1 + \frac{R_1^2}{\xi_1})^2} d\xi_1 \\
& + q_4 z_1 \int_{R_1}^{S_1} \frac{dZ_w(x, \xi_1 + \frac{c^2}{4\xi_1})}{dx} \frac{1}{\xi_1^2} \frac{d\xi_1}{z_1^2 + (Y_1 + \frac{R_1^2}{\xi_1})^2} \Bigg] \Bigg) \\
& - \frac{\lambda^2 - 1}{\lambda^2} a \frac{da}{dx} q_1 \left(-4 \int_a^S \frac{dZ_w(x, \xi)}{dx} d\xi + \frac{S'_{eb}(x)}{2} + 2 z_w(x, a) \frac{da}{dx} \right) \\
& + \frac{dZ_w(x, s)}{dx} \frac{ds}{dx} \times
\end{aligned}$$

(Continued on next page)

$$\begin{aligned}
& \ln \left\{ \frac{[z_1^2 + (s_1 - y_1)^2][z_1^2 + (s_1 + y_1)^2][z_1^2 + (y_1 - \frac{R_1^2}{s_1})^2][z_1^2 + (y_1 + \frac{R_1^2}{s_1})^2]}{(z_1^2 + y_1^2)^4} \right\} \\
& - 2 \frac{dz_w(x, a)}{dx} \frac{da}{dx} \ln \left\{ \frac{[z_1^2 + (y_1 - R_1)^2][z_1^2 + (y_1 + R_1)^2]}{(z_1^2 + y_1^2)^2} \right\} \\
& + \left\{ \frac{S_{eb}''(x)}{2} + 2 \left[\left(\frac{dz_w(x, a)}{dx} + \frac{dz_w(x, a)}{dy} \frac{da}{dx} \right) \frac{da}{dx} \right. \right. \\
& \left. \left. + z_w(x, a) \frac{d^2 a}{dx^2} \right] \right\} \ln(z_1^2 + y_1^2) \quad (74)
\end{aligned}$$

$$\begin{aligned}
\frac{v_{2,t}}{U_\infty} &= \frac{1}{\pi} \left\{ q_5 \int_{R_1}^{s_1} \frac{dz_w(x, \xi_1 + \frac{c^2}{4\xi_1})}{dx} \left[\frac{y_1 - \xi_1}{z_1^2 + (y_1 - \xi_1)^2} + \frac{y_1 + \xi_1}{z_1^2 + (y_1 + \xi_1)^2} \right. \right. \\
&+ \frac{y_1 - \frac{R_1^2}{\xi_1}}{z_1^2 + (y_1 - \frac{R_1^2}{\xi_1})^2} + \frac{y_1 + \frac{R_1^2}{\xi_1}}{z_1^2 + (y_1 + \frac{R_1^2}{\xi_1})^2} \left. \left. \right] \left(1 - \frac{c^2}{4\xi_1^2} \right) d\xi_1 \right. \\
&+ q_6 z_1 \int_{R_1}^{s_1} \frac{dz_w(x, \xi_1 + \frac{c^2}{4\xi_1})}{dx} \left[\frac{1}{z_1^2 + (y_1 - \xi_1)^2} + \frac{1}{z_1^2 + (y_1 + \xi_1)^2} \right. \\
&+ \frac{1}{z_1^2 + (y_1 - \frac{R_1^2}{\xi_1})^2} + \frac{1}{z_1^2 + (y_1 + \frac{R_1^2}{\xi_1})^2} \left. \left. \right] \left(1 - \frac{c^2}{4\xi_1^2} \right) d\xi_1 \right. \\
&+ \frac{q_5 y_1 + q_6 z_1}{z_1^2 + y_1^2} \left(-4 \int_a^S \frac{dz_w(x, \xi)}{dx} d\xi + \frac{S_{eb}'(x)}{2} + 2 z_w(x, a) \frac{da}{dx} \right) \quad (75)
\end{aligned}$$

$$\begin{aligned}
\frac{w_{2,t}}{U_\infty} = \frac{1}{\pi} \left\{ -q_6 \int_{R_1}^{s_1} \frac{dZ_w(x, \xi_1 + \frac{c^2}{4\xi_1})}{dx} \left[\frac{Y_1 - \xi_1}{z_1^2 + (Y_1 - \xi_1)^2} + \frac{Y_1 + \xi_1}{z_1^2 + (Y_1 + \xi_1)^2} \right. \right. \\
+ \frac{Y_1 - \frac{R_1^2}{\xi_1}}{z_1^2 + (Y_1 - \frac{R_1^2}{\xi_1})^2} + \left. \frac{Y_1 + \frac{R_1^2}{\xi_1}}{z_1^2 + (Y_1 + \frac{R_1^2}{\xi_1})^2} \right] \left(1 - \frac{c^2}{4\xi_1^2} \right) d\xi_1 \\
+ q_5 z_1 \int_{R_1}^{s_1} \frac{dZ_w(x, \xi_1 + \frac{c^2}{4\xi_1})}{dx} \left[\frac{1}{z_1^2 + (Y_1 - z_1)^2} + \frac{1}{z_1^2 + (Y_1 + z_1)^2} \right. \\
+ \frac{1}{z_1^2 + (Y_1 - \frac{R_1^2}{\xi_1})^2} + \left. \frac{1}{z_1^2 + (Y_1 + \frac{R_1^2}{\xi_1})^2} \right] \left(1 - \frac{c^2}{4\xi_1^2} \right) d\xi_1 \\
+ \left. \frac{q_5 z_1 - q_6 Y_1}{z_1^2 + Y_1^2} \left(-4 \int_a^S \frac{dZ_w(x, \xi)}{dx} d\xi + \frac{S'_{eb}(x)}{2} + 2 Z_w(x, a) \frac{da}{dx} \right) \right\} \quad (76)
\end{aligned}$$

For points on the wing surface but not at the wing-body junction, that is $z = 0$, $a < y < s$ (or equivalently $z_1 = 0$, $R_1 < y_1 < s_1$),

$$\begin{aligned}
\frac{u_{2,t}}{U_\infty} = \frac{1}{2\pi} \left\{ \int_{R_1}^{s_1} \frac{d^2 Z_w(x, \xi_1 + \frac{c^2}{4\xi_1})}{dx^2} \ln \left[\frac{(Y_1 + \xi_1)^2 (Y_1 + \frac{R_1^2}{\xi_1})^2}{Y_1^4} \right] \left(1 - \frac{c^2}{4\xi_1^2} \right) d\xi_1 \right. \\
+ \int_{R_1}^{s_1} \left(\frac{d^2 Z_w(x, \xi_1 + \frac{c^2}{4\xi_1})}{dx^2} - \frac{d^2 Z_w(x, Y_1 + \frac{c^2}{4Y_1})}{dx^2} \right) \ln \left[\left(\frac{Y_1 - \xi_1}{Y_1} \right)^2 \right] \left(1 - \frac{c^2}{4\xi_1^2} \right) d\xi_1 \\
+ \int_{R_1}^{s_1} \left(\frac{d^2 Z_w(x, \xi_1 + \frac{c^2}{4\xi_1})}{dx^2} - \frac{d^2 Z_w(x, R_1 + \frac{c^2}{4R_1})}{dx^2} \right) \ln \left[\left(\frac{Y_1 - \frac{R_1^2}{\xi_1}}{Y_1} \right)^2 \right] \left(1 - \frac{c^2}{4\xi_1^2} \right) d\xi_1
\end{aligned}$$

(Continued on next page)

$$\begin{aligned}
& + \frac{d^2 Z_w(x, Y_1 + \frac{c^2}{4Y_1})}{dx^2} 2 \left\{ (s_1 - Y_1) \left[\ln \left(\frac{s_1 - Y_1}{Y_1} \right) - 1 \right] + (Y_1 - R_1) \left[\ln \left(\frac{Y_1 - R_1}{Y_1} \right) - 1 \right] \right. \\
& - \left. \frac{c^2}{4} \frac{1}{Y_1} \left[\left(\frac{s_1 - Y_1}{s_1} \right) \ln \left(\frac{s_1 - Y_1}{Y_1} \right) + \left(\frac{Y_1 - R_1}{R_1} \right) \ln \left(\frac{Y_1 - R_1}{Y_1} \right) - \ln \left(\frac{s_1}{R_1} \right) \right] \right\} \\
& + \frac{d^2 Z_w(x, R_1 + \frac{c^2}{4R_1})}{dx^2} 2 \left[s_1 \ln \left(\frac{s_1 - \frac{R_1^2}{Y_1}}{s_1} \right) - R_1 \ln \left(\frac{R_1 - \frac{R_1^2}{Y_1}}{R_1} \right) \right. \\
& - \left. \frac{R_1^2}{Y_1} \ln \left(\frac{s_1 - \frac{R_1^2}{Y_1}}{R_1 - \frac{R_1^2}{Y_1}} \right) \right. \\
& - \left. \frac{c^2}{4} \left\{ \frac{1}{s_1} \left[\left(\frac{s_1 - \frac{R_1^2}{Y_1}}{\frac{R_1^2}{Y_1}} \right) \ln \left(\frac{s_1 - \frac{R_1^2}{Y_1}}{s_1} \right) + 1 \right] - \frac{1}{R_1} \left[\left(\frac{R_1 - \frac{R_1^2}{Y_1}}{\frac{R_1^2}{Y_1}} \right) \ln \left(\frac{R_1 - \frac{R_1^2}{Y_1}}{R_1} \right) + 1 \right] \right\} \right] \\
& + \left(\frac{\lambda^2 - 1}{\lambda^2} \right) a \frac{da}{dx} \left[-2 q_1 \int_a^s \frac{dZ_w(x, \xi)}{dx} d\xi - q_1 \left(-4 \int_a^s \frac{dZ_w(x, \xi)}{dx} d\xi \right. \right. \\
& + \left. \left. \frac{S'_{eb}(x)}{2} + 2 Z_w(x, a) \frac{da}{dx} \right) \right. \\
& + \left(\frac{\lambda + 1}{\lambda - 1} \right) \frac{q_s}{Y_1} \left[- \int_{R_1}^{s_1} \frac{\left(\frac{dZ_w(x, \xi_1 + \frac{c^2}{4\xi_1})}{dx} - \frac{dZ_w(x, R_1 + \frac{c^2}{4R_1})}{dx} \right)}{\xi_1 - \frac{R_1^2}{Y_1}} d\xi_1 \right. \\
& + \left. \int_{R_1}^{s_1} \frac{\frac{dZ_w(x, \xi_1 + \frac{c^2}{4\xi_1})}{dx}}{\xi_1 + \frac{R_1^2}{Y_1}} d\xi_1 \right]
\end{aligned}$$

(Continued on next page)

$$\begin{aligned}
& + \frac{c^2}{4} \frac{q_3}{Y_1} \left[\int_{R_1}^{s_1} \frac{\left(\frac{dZ_w(x, \xi_1 + \frac{c^2}{4\xi_1})}{dx} - \frac{dZ_w(x, R_1 + \frac{c^2}{4R_1})}{dx} \right)}{\xi_1 - \frac{R_1^2}{Y_1}} d\xi_1 \right. \\
& + \left. \int_{R_1}^{s_1} \frac{\frac{dZ_w(x, \xi_1 + \frac{c^2}{4\xi_1})}{dx}}{\xi_1 (\xi_1 + \frac{R_1^2}{Y_1})} d\xi_1 \right] \\
& + \frac{dZ_w(x, s)}{dx} \frac{ds}{dx} \ln \left[\frac{(s_1 - Y_1)^2 (s_1 + Y_1)^2 (Y_1 - \frac{R_1^2}{s_1})^2 (Y_1 + \frac{R_1^2}{s_1})^2}{Y_1^8} \right] \\
& + \frac{dZ_w(x, a)}{dx} \frac{da}{dx} \left\{ -2 \ln \left[\frac{(Y_1 - R_1)^2 (Y_1 + R_1)^2}{Y_1^4} \right] - \frac{4 a q_3}{\lambda} \ln \left(\frac{s_1 - \frac{R_1^2}{Y_1}}{R_1 - \frac{R_1^2}{Y_1}} \right) \right. \\
& - \left. \left(\frac{\lambda - 1}{\lambda} \right)^2 \cdot a \cdot q_3 \cdot \ln \left(\frac{s_1}{R_1} \right) \right\} \\
& + \left\{ \frac{S_{eb}''(x)}{2} + 2 \left[\left(\frac{dZ_w(x, a)}{dx} + \frac{dZ_w(x, a)}{dx} \frac{da}{dx} \right) \frac{da}{dx} + Z_w(x, a) \frac{d^2 a}{dx^2} \right] \right\} \ln(Y_1^2)
\end{aligned}$$

(77)

$$\begin{aligned}
\frac{v_{2,t}}{U_\infty} = & \frac{q_5}{\pi} \left[\int_{R_1}^{s_1} \frac{dz_w(x, \xi_1 + \frac{c^2}{4\xi_1})}{dx} \left(\frac{1}{y_1 + \xi_1} + \frac{1}{y_1 + \frac{R_1^2}{\xi_1}} \right) \left(1 - \frac{c^2}{4\xi_1^2} \right) d\xi_1 \right. \\
& - \int_{R_1}^{s_1} \frac{\left(\frac{dz_w(x, \xi_1 + \frac{c^2}{4\xi_1})}{dx} - \frac{dz_w(x, y_1 + \frac{c^2}{4y_1})}{dx} \right)}{\xi_1 - y_1} \left(1 - \frac{c^2}{4\xi_1^2} \right) d\xi_1 \\
& + \frac{1}{y_1} \int_{R_1}^{s_1} \frac{\xi_1 \left(\frac{dz_w(x, \xi_1 + \frac{c^2}{4\xi_1})}{dx} - \frac{dz_w(x, R_1 + \frac{c^2}{4R_1})}{dx} \right)}{\xi_1 - \frac{R_1^2}{y_1}} \left(1 - \frac{c^2}{4\xi_1^2} \right) d\xi_1 \\
& - \frac{dz_w(x, \xi + \frac{c^2}{4\xi_1})}{dx} \left\{ \ln \left(\frac{s_1 - y_1}{y_1 - R_1} \right) + \frac{c^2}{4} \left[\frac{1}{y_1^2} \left[\ln \left(\frac{s_1}{R_1} \right) \right. \right. \right. \\
& \left. \left. \left. - \ln \left(\frac{s_1 - y_1}{y_1 - R_1} \right) \right] + \frac{1}{y_1} \left(\frac{s_1 - R_1}{s_1 \cdot R_1} \right) \right] \right\} \\
& + \frac{dz_w(x, R_1 + \frac{c^2}{4R_1})}{dx} \frac{1}{y_1} \left\{ s_1 - R_1 + \frac{R_1^2}{y_1} \ln \left(\frac{s_1 - \frac{R_1^2}{y_1}}{R_1 - \frac{R_1^2}{y_1}} \right) \right. \\
& \left. + \frac{c^2}{4} \frac{1}{\frac{R_1^2}{y_1}} \left[\ln \left(\frac{s_1}{R_1} \right) - \ln \left(\frac{s_1 - \frac{R_1^2}{y_1}}{R_1 - \frac{R_1^2}{y_1}} \right) \right] \right\} \\
& + \left(-4 \int_a^s \frac{dz_w(x, \xi)}{dx} d\xi + \frac{s'_{eb}(x)}{2} + 2 z_w(x, a) \frac{da}{dx} \right) \frac{1}{y_1} \Bigg] \quad (78)
\end{aligned}$$

$$\frac{w_{2,t}}{U_\infty} = \frac{dZ_w(x,y)}{dx} \quad (79)$$

and for points along the wing-body junction, i.e. $z = 0$, $y = a$
(or equivalently $z_1 = 0$, $y_1 = R_1$),

$$\begin{aligned} \frac{u_{2,t}}{U_\infty} = & \frac{1}{2\pi} \left\{ \int_{R_1}^{s_1} \frac{dZ_w(x, \xi_1 + \frac{c^2}{4\xi_1})}{dx^2} \ln \left[\frac{(y_1 + \xi_1)^2 (y_1 + \frac{R_1^2}{\xi_1})^2}{y_1^4} \right] \left(1 - \frac{c^2}{4\xi_1^2} \right) d\xi_1 \right. \\ & + \int_{R_1}^{s_1} \left(\frac{d^2 Z_w(x, \xi_1 + \frac{c^2}{4\xi_1})}{dx^2} - \frac{d^2 Z_w(x, R_1 + \frac{c^2}{4R_1})}{dx^2} \right) \ln \left[\left(\frac{R_1 - \xi_1}{R_1} \right)^2 \right] \left(1 - \frac{c^2}{4\xi_1^2} \right) d\xi_1 \\ & + \int_{R_1}^{s_1} \left(\frac{d^2 Z_w(x, \xi_1 + \frac{c^2}{4\xi_1})}{dx^2} - \frac{d^2 Z_w(x, R_1 + \frac{c^2}{4R_1})}{dx^2} \right) \ln \left[\left(\frac{R_1 - \frac{R_1^2}{\xi_1}}{R_1} \right)^2 \right] \left(1 - \frac{c^2}{4\xi_1^2} \right) d\xi_1 \\ & + \frac{d^2 Z_w(x, R_1 + \frac{c^2}{4R_1})}{dx^2} 2 \left[(s_1 - R_1) \left[\ln \left(\frac{s_1 - R_1}{R_1} \right) - 1 \right] + s_1 \ln \left(\frac{s_1 - R_1}{s_1} \right) \right. \\ & - R_1 \ln \left(\frac{s_1 - R_1}{R_1} \right) \\ & - \frac{c^2}{4} \left\{ \frac{1}{R_1} \left[\left(\frac{s_1 - R_1}{s_1} \right) \ln \left(\frac{s_1 - R_1}{R_1} \right) - \ln \left(\frac{s_1}{R_1} \right) \right] + \frac{1}{s_1} \left[\left(\frac{s_1 - R_1}{s_1} \right) \times \right. \right. \\ & \left. \left. \ln \left(\frac{s_1 - R_1}{s_1} \right) + 1 \right] \frac{1}{R_1} \right\} \\ & + \left(\frac{\lambda^2 - 1}{\lambda^2} \right) a \frac{da}{dx} \left\{ -2 q_1 \int_a^s \frac{dZ_w(x, \xi)}{dx} d\xi - q_1 \left(-4 \int_a^s \frac{dZ_w(x, \xi)}{dx} d\xi \right. \right. \end{aligned}$$

(Continued on next page)

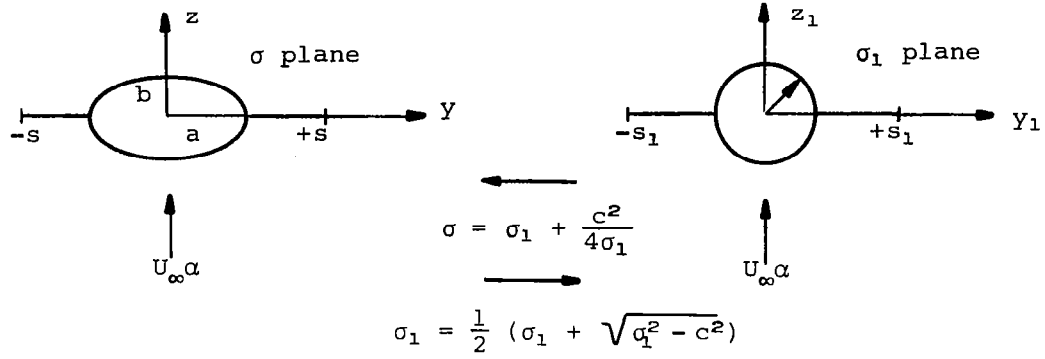
$$\begin{aligned}
& + \frac{s'_{eb}(x)}{2} + 2 Z_w(x, a) \frac{da}{dx} \Bigg) \\
& + \left(\frac{\lambda + 1}{\lambda - 1} \right) \frac{qs}{R_1} \left[- \int_{R_1}^{s_1} \frac{\left(\frac{dZ_w(x, \xi_1 + \frac{c^2}{4\xi_1})}{dx} - \frac{dZ_w(x, R_1 + \frac{c^2}{4R_1})}{dx} \right)}{\xi_1 - R_1} d\xi_1 \right. \\
& + \left. \int_{R_1}^{s_1} \frac{\frac{dZ_w(x, \xi_1 + \frac{c^2}{4\xi_1})}{dx}}{\xi_1 + R_1} d\xi_1 \right] \\
& + \frac{c^2}{4} \frac{q_3}{R_1} \left[\int_{R_1}^{s_1} \frac{\left(\frac{dZ_w(x, \xi_1 + \frac{c^2}{4\xi_1})}{dx} - \frac{dZ_w(x, R_1 + \frac{c^2}{4R_1})}{dx} \right)}{\xi_1 (\xi_1 - R_1)} d\xi_1 \right. \\
& + \left. \int_{R_1}^{s_1} \frac{\frac{dZ_w(x, \xi_1 + \frac{c^2}{4\xi_1})}{dx}}{\xi_1 + R_1} d\xi_1 \right] \Bigg\} \\
& + \frac{dZ_w(x, s)}{dx} \frac{ds}{dx} \ln \left[\frac{(s_1 - R_1)^2 (s_1 + R_1)^2 (R_1 - \frac{R_1^2}{s_1})^2 (R_1 + \frac{R_1^2}{s_1})^2}{R_1^8} \right] \\
& + \frac{dZ_w(x, a)}{dx} \frac{da}{dx} \left\{ -4 \ln \left[\frac{2 (s_1 - R_1)}{R_1} \right] - \frac{(\lambda - 1)^2}{\lambda} \ln \left(\frac{s_1}{R_1} \right) \right\} \\
& + \left\{ \frac{s''_{eb}(x)}{2} + 2 \left[\left(\frac{dZ_w(x, a)}{dx} + \frac{dZ_w(x, a)}{dy} \frac{da}{dx} \right) \frac{da}{dx} + Z_w(x, a) \frac{d^2 a}{dx^2} \right] \right\} \ln(R_1^2) \Bigg\}
\end{aligned}$$

(80)

$$\begin{aligned}
\frac{v_{z,t}}{U_\infty} = & \frac{q_5}{\pi} \left[\int_{R_1}^{s_1} \frac{dZ_w(x, \xi_1 + \frac{c^2}{4\xi_1})}{dx} \left(\frac{1}{R_1 + \xi_1} + \frac{1}{R_1^2 + \frac{1}{\xi_1}} \right) \left(1 - \frac{c^2}{4\xi_1^2} \right) d\xi_1 \right. \\
& - \int_{R_1}^{s_1} \frac{\left(\frac{dZ_w(x, \xi_1 + \frac{c^2}{4\xi_1})}{dx} - \frac{dZ_w(x_1, R_1 + \frac{c^2}{4R_1})}{dx} \right)}{\xi_1 - R_1} \left(1 - \frac{c^2}{4\xi_1^2} \right) d\xi_1 \\
& + \frac{1}{R_1} \int_{R_1}^{s_1} \frac{\xi_1 \left(\frac{dZ_w(x, \xi_1 + \frac{c^2}{4\xi_1})}{dx} - \frac{dZ_w(x, R_1 + \frac{c^2}{4R_1})}{dx} \right)}{\xi_1 - R_1} \left(1 - \frac{c^2}{4\xi_1^2} \right) d\xi_1 \\
& + \frac{dZ_w(x, R_1 + \frac{c^2}{4R_1})}{dx} \left(\frac{s_1 - R_1}{R_1} - \frac{c^2}{4} \frac{s_1 - R_1}{R_1^2 \cdot s_1} \right) \\
& \left. + \left(-4 \int_a^s \frac{dZ(x, \xi)}{dx} d\xi + \frac{S'_{eb}(x)}{2} + 2 Z_w(x, a) \frac{da}{dx} \right) \frac{1}{R_1} \right] \quad (81)
\end{aligned}$$

$$\frac{w_{z,t}}{U_\infty} = \frac{dZ_w(x, a)}{dx} \quad (82)$$

Lifting problem.— In order to solve the corresponding lifting problem for flows at small angles of attack about wing elliptic-body combinations, it is convenient to employ again the Joukowski transformation (eq. (59)) used in the thickness problem.



In order to preserve the body contour as a streamline in this transformation we first solve the cross flow problem for the complex potential having zero normal velocity at the contour surface and a velocity at infinity proportional to the angle of attack (see eq. (50)). In the transformed plane we have

$$\frac{w_{z_1}^{(1)}(\sigma_1)}{U_\infty} = -i\alpha \left[\left(\sigma_1 + \frac{R_1^2}{\sigma_1} \right)^2 - \left(s_1 + \frac{R_1^2}{s_1} \right)^2 \right]^{1/2} \quad (83)$$

then, by using the above Joukowski transformation to transfer back to the physical plane,

$$\begin{aligned} \frac{w_z^{(1)}(\sigma)}{U_\infty} = & -i\alpha \left\{ \left[\frac{\sigma + \sqrt{\sigma^2 - c^2}}{2} + \frac{(a+b)^2}{2(\sigma + \sqrt{\sigma^2 - c^2})} \right]^2 \right. \\ & \left. - \left[\frac{s + \sqrt{s^2 - c^2}}{2} + \frac{(a+b)^2}{2(s + \sqrt{s^2 - c^2})} \right]^2 \right\}^{1/2} \end{aligned} \quad (84)$$

and finally, by adding a uniform free stream $U_\infty \alpha$ in the negative z direction to obtain the desired potential for the wing-body cross section translating downward at the constant rate $U_\infty \alpha$, we arrive at the final result

$$\frac{w_{2,\alpha}(\sigma)}{U_\infty} = - \frac{i\alpha}{2} \left\{ \left[\left(\sigma + \sqrt{\sigma^2 - c^2} + \frac{(a+b)^2}{(\sigma + \sqrt{\sigma^2 - c^2})} \right)^2 - \left(s + \sqrt{s^2 - c^2} + \frac{(a+b)^2}{(s + \sqrt{s^2 - c^2})} \right)^2 \right]^{1/2} - 2\sigma \right\} \quad (85)$$

The velocity components associated with this flow are given by

$$\begin{aligned} \frac{u_{2,\alpha}}{U_\infty} = & \text{R.P.} \left(- \frac{i\alpha}{2} \left\{ - \left(\frac{\lambda^2 - 1}{\lambda^2} \right) \left[\sigma + \sqrt{\sigma^2 - c^2} + \frac{(a+b)^2}{(\sigma + \sqrt{\sigma^2 - c^2})} \right] \times \right. \right. \\ & \left[1 - \left(\frac{a+b}{\sigma + \sqrt{\sigma^2 - c^2}} \right)^2 \right] \frac{a \frac{da}{dx}}{\sqrt{\sigma^2 - c^2}} \\ & - \left[s + \sqrt{s^2 - c^2} + \frac{(a+b)^2}{(s + \sqrt{s^2 - c^2})} \right] \left[1 - \left(\frac{a+b}{s + \sqrt{s^2 - c^2}} \right)^2 \right] \times \\ & \left(\frac{(s + \sqrt{s^2 - c^2}) \frac{ds}{dx} - \left(\frac{\lambda^2 - 1}{\lambda^2} \right) a \frac{da}{dx}}{\sqrt{s^2 - c^2}} \right) \\ & + \left(\frac{\lambda + 1}{\lambda} \right) \left\{ \left[\sigma + \sqrt{\sigma^2 - c^2} + \frac{(a+b)^2}{(\sigma + \sqrt{\sigma^2 - c^2})} \right] \left(\frac{a+b}{\sigma + \sqrt{\sigma^2 - c^2}} \right) \right. \\ & - \left[s + \sqrt{s^2 - c^2} + \frac{(a+b)^2}{(s + \sqrt{s^2 - c^2})} \right] \left(\frac{a+b}{s + \sqrt{s^2 - c^2}} \right) \left. \right\} \frac{da}{dx} \Bigg\} \div \\ & \left(\left[\sigma + \sqrt{\sigma^2 - c^2} + \frac{(a+b)^2}{(\sigma + \sqrt{\sigma^2 - c^2})} \right]^2 - \left[s + \sqrt{s^2 - c^2} + \frac{(a+b)^2}{(s + \sqrt{s^2 - c^2})} \right]^2 \right)^{1/2} \end{aligned} \quad (86)$$

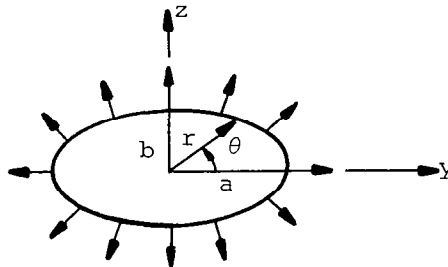
$$\frac{(v - iw)_{z,\alpha}}{U_\infty} = -i\alpha \times$$

$$\left\{ \frac{\left[\sigma + \sqrt{\sigma^2 - c^2} + \frac{(a+b)^2}{(\sigma + \sqrt{\sigma^2 - c^2})} \right] \left[1 - \left(\frac{a+b}{\sigma + \sqrt{\sigma^2 - c^2}} \right)^2 \right] (\sigma + \sqrt{\sigma^2 - c^2})}{2\sqrt{\sigma^2 - c^2} \left\{ \left[\sigma + \sqrt{\sigma^2 - c^2} + \frac{(a+b)^2}{(\sigma + \sqrt{\sigma^2 - c^2})} \right]^2 - \left[s + \sqrt{s^2 - c^2} + \frac{(a+b)^2}{(s + \sqrt{s^2 - c^2})} \right]^2 \right\}^{1/2}} - 1 \right\}$$

(87)

where again, the symmetry properties stated by equations (40) and (41) apply.

Aerodynamic characteristics.— For the case of nonlifting flows about these classes of symmetric configurations, no lateral forces or moments exist so that the only force present is the longitudinal drag force. This can be determined through the use of equation (42) where now the contributions of the two line integrals do not cancel since the contour over which the product $\phi_{2,t} \frac{\partial \phi_{2,t}}{\partial n}$ is evaluated is the elliptic cross section at the base of the body whereas the contour for evaluating $\phi_{2,B} \frac{\partial \phi_{2,B}}{\partial n}$ is, of course, the circular cross section of the equivalent body. In order to evaluate the integral over the ellipse, we require the potential for flow caused by an expanding (or contracting) elliptical cross section which maintains a constant ratio $\lambda = a/b$ of major to minor axis. This is given by (ref. 30)



$$\frac{\phi_{2,t}}{U_\infty} = \text{R.P.} \left(\frac{w_{2,t}}{U_\infty} \right) = \text{R.P.} \left[\frac{S'_{eb}(x)}{2\pi} \ln \left(\sigma + \frac{\sqrt{\sigma^2 - c^2}}{2} \right) \right] \quad (88)$$

Now, it can be shown that

$$\phi_{2,t} \Big|_{\text{surface}} = \frac{U_\infty S'_{eb}(x)}{2\pi} \ln \left[\frac{a(\lambda + 1)}{2\lambda} \right] \quad (89)$$

$$\frac{\partial \phi_{2,t}}{\partial n} \Big|_{\text{surface}} = \frac{U_\infty S'_{eb}(x)}{2\pi} \frac{\lambda}{a} \sqrt{\frac{\cos^2 \theta + \lambda^2 \sin^2 \theta}{\cos^2 \theta + \lambda^4 \sin^2 \theta}} \quad (90)$$

$$r(\theta) = \frac{a}{\sqrt{\cos^2 \theta + \lambda^2 \sin^2 \theta}} \quad (91)$$

and since

$$\int_{C_t} \phi_{2,t} \frac{\partial \phi_{2,t}}{\partial n} d\sigma_t = \int_0^{2\pi} \phi_{2,t} \frac{\partial \phi_{2,t}}{\partial n} r(\theta) d\theta \quad (92)$$

we find that

$$\int_C \phi_{2,t} \frac{\partial \phi_{2,t}}{\partial n} d\sigma_c = \left(\frac{U_\infty S'_{eb}(x)}{2\pi} \right)^2 \frac{4}{\lambda} \ln \left[\frac{a(\lambda + 1)}{2\lambda} \right] K \left(\frac{\sqrt{\lambda^4 - 1}}{\lambda^2} \right) \quad (93)$$

where $K(\xi)$ is the complete elliptic integral of the first kind (ref. 31).

To evaluate the line integral of $\phi_{2,B} \frac{\partial \phi_{2,B}}{\partial n}$ we can simply place $\lambda = 1$, $a = R_{eb}$ in equation (93). Thus,

$$\int_{C_B} \phi_{2,B} \frac{\partial \phi_{2,B}}{\partial n} d\sigma_B = \left(\frac{U_\infty S'_{eb}(x)}{2\pi} \right)^2 2\pi \ln (R_{eb}) \quad (94)$$

so that the drag coefficient of this general class of nonlifting elliptic body combinations is

$$C_{D_{\alpha=0}} = C_{D_{eb}} - \frac{1}{S_m} \left(\frac{S'_{eb}(x)}{2\pi} \right)^2 \frac{2}{\lambda} \ln \left(\frac{a(\lambda+1)}{2\lambda} \right) K \left(\frac{\sqrt{\lambda^4-1}}{\lambda^2} \right) - \pi \ln R_{eb} \quad (95)$$

where $C_{D_{eb}}$ is the drag coefficient of the nonlifting equivalent body and is given by equation (44).

For lifting flows at small angles of attack about these configurations, if we apply the same assumptions regarding the trailing vortex wake as were made for the circular body case, then the evaluation of equations (46), (47), and (48) provides the following results for the lift, pitching moment, and drag coefficients.

$$C_L = \frac{2\pi\alpha}{S_m} \left\{ \left(\frac{s + \sqrt{s^2 - c^2}}{2} \right)^2 \left[1 + \frac{2c^2}{(s + \sqrt{s^2 - c^2})^2} + \left(\frac{a+b}{(s + \sqrt{s^2 - c^2})} \right)^4 \right] - R_{eb}^2 \right\} \Big|_{x=X_{sm}} \quad (96)$$

$$C_m = \frac{2\pi\alpha}{S_m \cdot \ell} \left(-x \left\{ \left(\frac{s + \sqrt{s^2 - c^2}}{2} \right)^2 \left[1 + \frac{2c^2}{(s + \sqrt{s^2 - c^2})^2} + \left(\frac{a+b}{(s + \sqrt{s^2 - c^2})} \right)^4 \right] - R_{eb}^2 \right\} \Big|_{x=X_{sm}} + \lambda \int_0^{X_{rle1}} R_{eb}^2(x) dx + \int_{X_{rle1}}^{X_{sm}} \left\{ \left(\frac{s + \sqrt{s^2 - c^2}}{2} \right)^2 \left[1 + \frac{2c^2}{(s + \sqrt{s^2 - c^2})^2} + \left(\frac{a+b}{(s + \sqrt{s^2 - c^2})} \right)^4 \right] - R_{eb}^2 \right\} dx \right) \quad (97)$$

$$C_{D_t} = C_{D_{\alpha=0}} + \frac{\alpha}{2} C_L \quad (98)$$

where $C_{D_{\alpha=0}}$ is the drag coefficient at zero lift and is given by equation (95).

Bumpy and Indented Bodies

In order to evaluate the extent to which the present techniques can be applied to configurations composed of finite thickness wings and smooth rather than indented bodies (so that the equivalent bodies are bumpy), the final application of this study is toward shapes having a bump (or indentation) superimposed upon an otherwise smooth body profile. Since shapes of this category have been studied experimentally in reference 32, attention will be directed primarily toward parabolic-arc bodies having a sinusoidal bump (or indentation) superimposed upon their midsections. The equation of the bump is given by

$$\frac{\Delta R}{\ell} = \frac{\Delta R_{\max}}{\ell} \sin^2 \left(\frac{\pi(x - x_1)}{x_2 - x_1} \right) \quad (99)$$

where x_1 and x_2 represent the axial locations of the start and end of the bump. While the total area distribution $S(x)$ and its first derivative $S'(x)$ are continuous at all points on the body, the second derivative $S''(x)$ is discontinuous at x_1 and x_2 and this fact must be taken into account in the analysis.

To determine the local linearization solution for this class of body shapes, it is convenient to split the area distribution $S(x)$ into two parts, i.e. (1) a contribution from the basic body $\bar{S}(x)$ and, (2) a contribution from the bump, $\Delta S(x)$. This is done both to facilitate numerical evaluation and also to exhibit clearly the effects of the bump. Since the basic bodies are parabolic-arcs, the two area distributions are given by the expressions

$$\bar{S}(x) = \pi \bar{R}^2 \quad (100)$$

$$\Delta S = \left\{ \begin{array}{ll} 0 & 0 \leq x \leq x_1 \\ \pi (2\bar{R} \Delta R + \Delta R^2) & x_1 \leq x \leq x_2 \\ 0 & x_2 < x \leq \lambda \end{array} \right\} \quad (101)$$

where \bar{R} is given by equation (12) with $n = 2$ and ΔR is given by equation (99).

The technique of applying the local linearization method to axisymmetric shapes is discussed in detail in reference 9 and can be summarized briefly as follows. For the purely subsonic and supersonic cases, the total coefficient of the quantity ϕ_{xx} in equation (2) is replaced by a positive constant λ . Thus, for subsonic flows, we have,

$$\lambda \equiv 1 - M_{\infty}^2 - \frac{M_{\infty}^2(\gamma + 1)}{U_{\infty}} \phi_x \quad (102)$$

while for supersonic flows,

$$\lambda \equiv M_{\infty}^2 - 1 + \frac{M_{\infty}^2(\gamma + 1)}{U_{\infty}} \phi_x \quad (103)$$

Next, the resulting linear differential equation is solved for ϕ and then differentiated to obtain the longitudinal velocity component

$$u = \phi_x(x, r; \lambda) \quad (104)$$

That expression is then evaluated at points on the surface of the slender body, giving $u_s(x, R(x); \lambda)$. The final step consists of differentiating the surface velocity u_s assuming that λ varies sufficiently slowly that its derivatives can be disregarded (this is equivalent to assuming that the surface acceleration du_s/dx is small), replacing λ by the quantity it originally represented, i.e. either equation (102) or (103), and then integrating the resulting first order nonlinear ordinary differential equation for u_s . For the $M_{\infty} \approx 1$ case, λ is taken to replace the coefficient of ϕ_x in the nonlinear term of equation (2) rather than ϕ_{xx} , thus

$$\lambda = \frac{M_{\infty}^2(\gamma + 1)}{U_{\infty}} \phi_{xx} \quad (105)$$

The procedure described above would then be repeated in a similar fashion.

Starting with the expressions which are valid even for discontinuous $\Delta S''(x)$, for the linearized longitudinal velocity component u_s , for purely subsonic flows

$$\frac{u_s}{U_\infty} = -\frac{1}{4\pi} \int_0^\ell \frac{\bar{S}''(\xi) d\xi}{\sqrt{(x-\xi)^2 + \beta_\ell^2 R^2}} - \frac{1}{4\pi} \int_{x_1}^{x_2} \frac{\Delta S''(\xi) d\xi}{\sqrt{(x-\xi)^2 + \beta_\ell^2 R^2}} \quad (106)$$

and for purely supersonic flows,

$$\frac{u_s}{U_\infty} = \frac{1}{2\pi} \int_0^{x-\beta_\ell R} \frac{\bar{S}(\xi) d\xi}{\sqrt{(x-\xi)^2 - \beta_\ell^2 R^2}} - \frac{1}{2\pi} \int_{x_1}^{x-\beta_\ell R} \frac{\Delta S''(\xi) d\xi}{\sqrt{(x-\xi)^2 + \beta_\ell^2 R^2}} \quad (107)$$

where

$$\beta_\ell = \sqrt{M_\infty^2 - 1} \quad (108)$$

we obtain the following results valid within the approximations of slender body theory. For free stream Mach numbers less than the lower critical, $M_\infty < M_{cr,\ell}$ (purely subsonic flows)

$$\begin{aligned} \frac{d}{dx} \left(\frac{u}{U_\infty} \right) &= \frac{\bar{S}'''(x)}{4\pi} \ln(\beta^2) + \frac{d}{dx} \left[\frac{\bar{S}''(x)}{4\pi} \ln \left(\frac{R^2}{4x(\ell-x)} \right) + \frac{1}{4\pi} \int_0^\ell \frac{\bar{S}''(x) - \bar{S}''(\xi)}{|x-\xi|} d\xi \right] \\ &+ \frac{1}{2\pi} \frac{\Delta S''(x_2)}{\sqrt{(x-x_2)^2 + \beta^2 R^2}} - \frac{1}{2\pi} \frac{\Delta S''(x_1)}{\sqrt{(x-x_1)^2 + \beta^2 R^2}} + \frac{1}{2\pi} \int_{x_1}^{x_2} \frac{\Delta S''(x) - \Delta S''(\xi)}{|x-\xi|} d\xi \\ &+ \frac{\Delta S'''(x)}{2\pi} \ln \left(\frac{x-x_2 + \sqrt{(x-x_2)^2 + \beta^2 R^2}}{x-x_1 + \sqrt{(x-x_1)^2 + \beta^2 R^2}} \right) + \frac{(\bar{S}''(x) + \Delta S''(x))(\bar{S}'(x) + \Delta S'(x))}{4\pi(\bar{S}(x) + \Delta S(x))} \end{aligned} \quad (109)$$

where

$$\beta^2 \equiv 1 - M_\infty^2 - (\gamma + 1) M_\infty^2 \frac{u}{U_\infty} \quad (110)$$

and

$$R = \bar{R} + \Delta R \quad (111)$$

and for free stream Mach numbers greater than the upper critical, $M_{cr,u} < M_\infty$ (purely supersonic flows)

$$\frac{d}{dx} \left(\frac{u}{U_\infty} \right) = \frac{\bar{S}'''(x)}{2\pi} \ln(\beta^2) - \frac{\bar{S}''(0)}{2\pi x} + \frac{1}{2\pi} \int_0^x \frac{\bar{S}'''(x) - \bar{S}'''(\xi)}{x - \xi} d\xi + \frac{\bar{S}'(x) \bar{S}''(x)}{4\pi \bar{S}(x)}$$

($x \leq x + \beta R$)

$$\begin{aligned} \frac{d}{dx} \left(\frac{u}{U_\infty} \right) &= \frac{\bar{S}'''(x)}{2\pi} \ln(\beta^2) - \frac{\bar{S}''(0)}{2\pi x} + \frac{1}{2\pi} \int_0^x \frac{\bar{S}'''(x) - \bar{S}'''(\xi)}{x - \xi} d\xi \\ &\quad - \frac{\Delta S''(x_1)}{\sqrt{(x - x_1)^2 - \beta^2 R^2}} + \frac{1}{2\pi} \int_{x_1}^x \frac{\Delta S'''(x) - \Delta S'''(\xi)}{x - \xi} d\xi \\ &\quad + \frac{\Delta S'''(x)}{2\pi} \ln \left(\frac{\beta R}{x - x_1 + \sqrt{(x - x_1)^2 - \beta^2 R^2}} \right) + \frac{(\bar{S}'' + \Delta S'')(\bar{S}' + \Delta S')}{4\pi(\bar{S} + \Delta S)} \end{aligned}$$

($x_1 + \beta R \leq x \leq x_2 + \beta R$)

$$\begin{aligned} \frac{d}{dx} \left(\frac{u}{U_\infty} \right) &= \frac{\bar{S}'''(x)}{2\pi} \ln(\beta^2) - \frac{\bar{S}''(0)}{2\pi x} + \frac{1}{2\pi} \int_0^x \frac{\bar{S}'''(x) - \bar{S}'''(\xi)}{x - \xi} d\xi \\ &\quad + \frac{\Delta S''(x_2)}{\sqrt{(x - x_2)^2 - \beta^2 R^2}} - \frac{\Delta S''(x_1)}{\sqrt{(x - x_1)^2 - \beta^2 R^2}} + \frac{1}{2\pi} \int_{x_1}^{x_2} \frac{\Delta S'''(x) - \Delta S'''(\xi)}{x - \xi} d\xi \\ &\quad + \frac{\Delta S'''(x)}{2\pi} \ln \left(\frac{x - x_2 + \sqrt{(x - x_2)^2 - \beta^2 R^2}}{x - x_1 + \sqrt{(x - x_1)^2 - \beta^2 R^2}} \right) + \frac{\bar{S}'(x) \cdot \bar{S}''(x)}{4\pi \bar{S}(x)} \end{aligned}$$

($x_2 + \beta R \leq x < \ell$)

(112)

where, depending upon the axial location, the various forms of the differential equation are necessary to account properly for the absence of upstream influence, and where in the last two expressions in equation (112) it is convenient to extend $\Delta S(x)$ and its derivatives analytically for $x > x_2$.

The boundary conditions necessary to start the integration of these equations are given by the following relations (see refs. 3, 9) for subsonic flow

$$\begin{aligned} \frac{u}{U_\infty} = & \frac{1}{4\pi} \int_0^{\ell} \frac{\bar{S}''(x) - \bar{S}''(\xi)}{|x - \xi|} d\xi + \frac{1}{4\pi} \int_{x_1}^{x_2} \frac{\Delta S''(x) - \Delta S''(\xi)}{|x - \xi|} d\xi \\ & + \frac{\Delta S''(x)}{4\pi} \ln \left(\frac{x - x_2 + \sqrt{(x - x_2)^2 + \beta_\ell^2 R^2}}{x - x_1 + \sqrt{(x - x_1)^2 + \beta_\ell^2 R^2}} \right) \text{ at } x = x_s \end{aligned} \quad (113)$$

and for supersonic flow

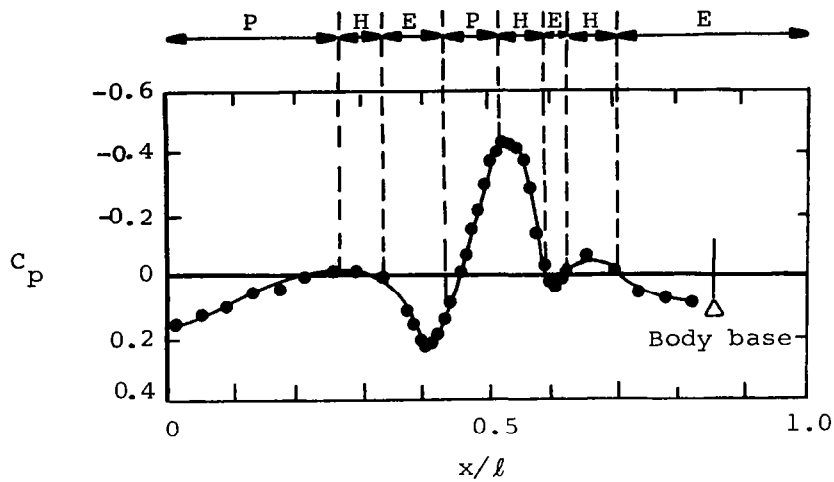
$$\frac{u}{U_\infty} = \frac{1}{2\pi} \int_0^x \frac{\bar{S}''(x) - \bar{S}''(\xi)}{x - \xi} d\xi \quad \text{at } x = x_s \quad (114)$$

where the starting point x_s of the integrations is the positive root of the equation

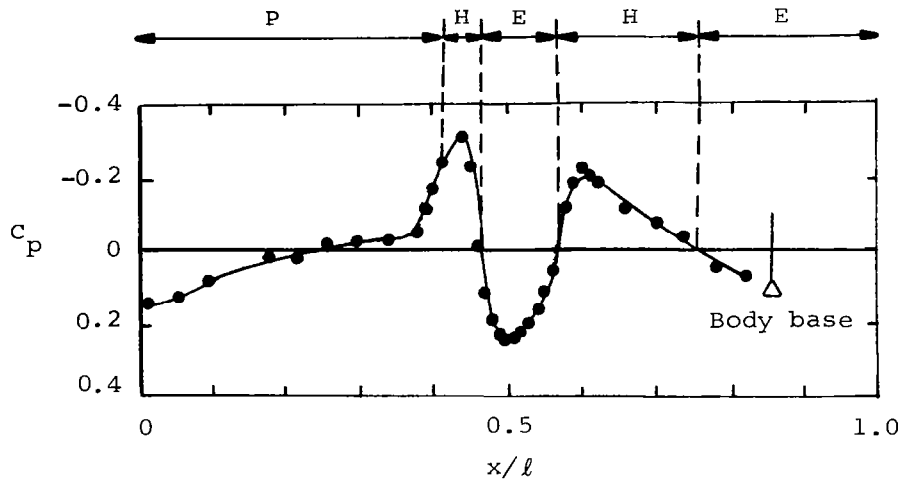
$$\bar{S}''(x) = 0 \quad (115)$$

that is closest to the origin.

As presently constituted, the local linearization method for determining flows at $M_\infty \approx 1$ about slender axisymmetric bodies utilizes the solution to a parabolic differential equation valid for accelerating flows. In order to treat properly regions of recompression or deceleration in these flows it is necessary to transfer from the solution determined by integrating that parabolic equation to those found by integrating the limiting forms (as $M_\infty \rightarrow 1$) of the corresponding hyperbolic and elliptic differential equations (see ref. 9). Consequently, to calculate completely flows at $M_\infty \approx 1$ about arbitrary slender shapes, transitions between the solutions to all three differential equations are required. This is illustrated graphically on the two figures below which are the experimental surface pressure distributions from reference 32 at $M_\infty = 1$ for a basic parabolic-arc body of thickness ratio $D/\ell = 1/14$ having a bump or indentation given by equation (99) with $\Delta R_{\max}/\ell = 1/70$.



Bumpy Body



Indented Body

Shown superimposed upon those curves are the different flow regimes according to whether the flow is locally governed by the transonic (parabolic, denoted P), the supersonic (hyperbolic, denoted H), or the subsonic (elliptic, denoted E) equations. Thus, a prerequisite for obtaining the local linearization solution at $M_\infty \approx 1$ about these classes of bodies is the possession of the corresponding subsonic and supersonic solutions.

For the particular shapes under consideration, however, comparisons of the theoretical and experimental results, particularly for the supersonic

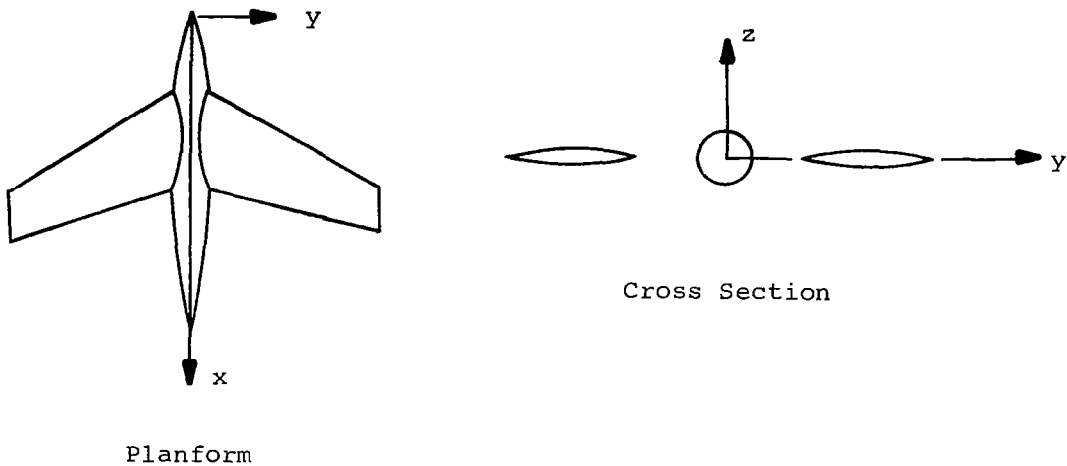
case, indicates that serious deficiencies are caused by the slender body approximations inherent in the present theories. Consequently, the discussion of the $M_\infty \approx 1$ case will be deferred until the next section.

RESULTS AND DISCUSSION

Wing-Body Combinations

As discussed previously, because the results of reference 3 are to be used in the present work as a means of providing solutions to the non-linear transonic equation (eq. (2)) for flows about the nonlifting equivalent body, the wing-body combinations being considered here consist of finite thickness wings and bodies which are area-rule indented in such a manner that the resultant equivalent body remains smooth. In order to provide experimental verification of the theory, a parallel experimental program was originally considered for a certain member of the particular class of wing-circular body combinations shown in figure 2. This configuration was to consist of an indented parabolic-arc body having an equivalent body thickness ratio $D/\ell = 1/10$ and symmetric diamond planform wings with leading and trailing edges swept at the same angle $\beta_{le} = \beta_{te} = \tan^{-1}(1/2)$, and with parabolic-arc wing profiles having a thickness/chord ratio $t/c_w = 0.04$. The root chord of the wing was to extend from $x/\ell = 1/3$ to $x/\ell = 2/3$ with the result that the entire configuration would be symmetric about the body midpoint. That program, unfortunately, has been delayed. Consequently, experimental verification of the theory, particularly for pressure distribution comparisons which are so vital in assessing the applicability of the assumptions of the theory within the various regions (body surface, wing surface, wing-body junction, wing leading and trailing edges, etc.) of the near flow field of these configurations, will have to be deferred. While experimental data for transonic flows about wing-indented body combinations already exists in the literature--for example, references 33 to 40--the majority of this data is for gross aerodynamic properties (lift, drag, pitching moment) with very little information available for pressure distributions. Even for that small amount that does exist (see refs. 35, 39) there are several factors which preclude its use for comparison with the theory developed in this report. The most important source of difficulty arises from the swept-back nature of the trailing edge of the wings used in

those tests. As a consequence, a typical wing-body cross section would appear in the cross flow plane as shown below



While it seems that solutions to the thickness problem associated with this type of configuration have not been given previously, the lifting problem has received prior attention, for example, in references 41 through 43. Although the analysis of the thickness problem would require some modification of the techniques used here (in order to account for the absence of a solid boundary between the body and wing cross sections), no fundamental difficulties should arise in its solution. For the corresponding lifting problem, however, a significant distinction does appear for wings with swept-back rather than straight or swept-forward trailing edges. In fact, Mangler (ref. 43) has shown that in order to account properly for the vortex sheet springing from the sections of the trailing edge ahead of the axial station in question, (even with the assumption that the vortex sheet proceeds parallel to the x -axis) the numerical solution of an integral equation is required.

Another factor which hinders comparison of the theory with the data referred to above is the magnitude of the aspect ratio of the wings tested. It was ascertained in reference 11 that the aspect ratio range over which slender body theory can be expected to provide reasonable results ought to be greater at $M_\infty = 1$ than at any other Mach number. In this regard, experimental information is known most completely for families of affinely related wings of rectangular planform (ref. 44)

and triangular planform (ref. 45). Through application of the transonic similarity rules it was observed that wings for which the product of aspect ratio times wing thickness ratio to the one-third power is less than approximately unity ($AR\tau_w^{1/3} < 1$), the experimental values for lift coincide with that predicted by the theory. This implies, for example, that for wings of thickness ratio $\tau_w = .04$, the aspect ratio should not be much greater than 3 for the theory to be valid, whereas for a ten percent thick wing the corresponding aspect ratio should not be greater than about 2. To the extent that these criteria can be applied to the configurations tested in references 33 to 40, it is clear that none of that data is applicable.

In order to illustrate the general behavior of transonic flows about the slender wing-body combinations considered, the surface and flow field pressure distributions for several members of the classes of configuration described previously are given in figures 4 through 9. For example, in figure 4 pressure distributions are presented for a finite thickness wing-indented circular body combination in which the equivalent body is a parabolic-arc of thickness ratio $D/\ell = 1/12$, the wings are triangular in planform with an aspect ratio $AR = 2$ (so that $\beta_{le} = \tan^{-1}(2)$, $\beta_{te} = 0$) and have parabolic-arc profiles of thickness/chord ratio $t/c_w = 0.04$. The wing root chord extends from $X_{rle}/\ell = 0.25$ to $X_{rte}/\ell = 0.75$ and the body base is taken to be at $X_{b/\ell} = 0.86$ (corresponding to the base location of the bodies tested in ref. 16). The longitudinal pressure distributions given in figure 4 are for the free-stream conditions $M_\infty = 1$, $\alpha = 0^\circ$ and are presented at the two angular positions $\theta = 0^\circ, 90^\circ$ in the cross flow plane and at locations on the body surface and also along lines parallel to body axis but removed laterally from it by distances of 1, 2, and 4 times the maximum equivalent body diameter D . Thus, the pressure distributions given for $\theta = 0^\circ$ and $r/D = 1, 2$ cut across the wing surface, intersecting the leading edge at the axial positions $x/\ell = 0.416, 0.583$, respectively.

The wing-body surface pressure distributions shown in the first plot of figure 4, when compared to the pressure distribution on the equivalent body alone, demonstrate the large effect that the wing has upon the body pressure distribution. Moreover, it clearly shows the rapid variation of the pressure distributions caused by the singularities at the points $(x/\ell = 0.322, 0.75)$ where the wing leading and trailing

edges pierce the body surface. These discontinuities are related to the characteristic logarithmic singularity associated with the two-dimensional thickness problem (i.e. $\phi_{2,t}$) of flow at a sharp edge. The flow field distributions shown at $r/D = 1, 2$, and 4 illustrate several interesting effects. Perhaps most prominent is the propagation into the flow field of the singularities which occur in the surface pressure distributions at the points where the leading and trailing edges intersect the body surface. This is a direct consequence of using the transonic equivalence rule to provide flow-field information based upon knowledge of flow properties on the body surface. Also evident in the distributions along the lines $r/D = 1, 2, \theta = 0^\circ$ are the logarithmic singularities at $x/l = 0.416, 0.583$, respectively, as those lines cross the wing leading edge. Further insight into that nature of these distributions is provided by the cross plot of spanwise pressures given in the last graph of figure 5. The longitudinal flow field distributions shown along the lines $r/D = 1, 2, 4, \theta = 90^\circ$ clearly exhibit the rapidity at which the flow field becomes axisymmetric and equal to that about the equivalent body. At the lateral distance of $r/D = 4$, the pressure distribution at $\theta = 90^\circ$ is virtually indistinguishable from that about the equivalent body (except for the exponentially small region of influence of the logarithmic singularities propagating from the body surface), while the corresponding distribution at $\theta = 0^\circ$, which would be most strongly influenced by the wing, shows that the effect of the wing on the flow field is negligible at all axial locations except in those in the near vicinity of its maximum span. Knowledge of the region in which the flow about geometrically complex configurations of this type can be considered axisymmetric and equal to that about the equivalent body is quite important and can, for example, provide useful information for a completely numerical finite difference solution in applying the far-field boundary condition. The drag coefficient for this configuration, which is provided by evaluating the integral given by equation (44), is found to be $C_D = 0.0750$.

Analogous results are given in figure 5 for a lifting flow about this same configuration for the free stream conditions $M_\infty = 1$ and $\alpha = 2^\circ$. We note again that the singularities discussed with regard to the nonlifting case also appear here. Moreover, due to the nature of lifting flows near a sharp edge, the logarithmic singularities associated with the thickness problem are further reinforced by the inverse square

root behavior of the lifting problem. The net effect, of course, is the more rapid variation in pressure evident in those regions. Nevertheless, the flow field distributions again display the strong tendency to return to those generated by the equivalent body alone. This point is most apparent in the spanwise distributions shown in figure 5 at various axial locations for the upper and lower surfaces of the wing-body combination and also at locations out in the flow field. The large pressures generated in the region close to the trailing edge and near the maximum span of the wing, as shown in these plots, results in loadings there which are particularly large. This is exhibited by the last plot given in figure 5 which shows the difference in pressure between the lower and upper surface of the wing-body at various axial locations. At this angle of attack, equations (53), (56), and (58) provide the following values for the aerodynamic coefficients:

$$C_L = 2.475, C_D = 0.118, C_m = 0.1454$$

Corresponding results of nonlifting purely subsonic and purely supersonic flow for this same configuration are presented in figures 6 and 7. Figure 6 exhibits the surface and flow-field pressure distributions at $M_\infty = 0.80$ while figure 7 gives the analogous results at $M_\infty = 1.20$. Because the two-dimensional cross flow potentials $\phi_{2,\alpha}$, $\phi_{2,t}$, and $\phi_{2,B}$ are all independent of free stream Mach number, the sole difference in the pressure coefficient for the same configuration at $M_\infty = 1$ and those at purely subsonic and supersonic Mach numbers arises from the u_B/U_∞ term associated with the solution to the full transonic equation (2) for flow about the equivalent nonlifting body of revolution. Consequently, the pressure coefficients shown in figures 4, 6, and 7 exhibit the same general behavior and differ from one another only in level. Hence, the loadings shown in figure 5 for $M_\infty = 1$ would be identical to those at $M_\infty = 0.80$, and 1.20 at the same angle of attack, as would the lift and pitching moment, but the drag would not be. Thus, we have the following aerodynamic characteristics for this configuration

M_∞	α (deg.)	C_D	C_L	C_m
1.00	0	0.074	0	0
1.00	2	0.118	2.475	- 1.454
0.80	0	0.014	0	0
0.80	2	0.058	2.475	- 1.454
1.20	0	0.084	0	0
1.20	2	0.128	2.475	- 1.454

where the drag for the nonlifting subsonic case ($M_\infty = 0.80$, $\alpha = 0^\circ$) differs from zero because of the truncated nature ($X_b/l = 0.86$) of the body.

In order to illustrate to some degree the effect that wing-body geometry changes have upon transonic pressure distributions, figure 8 presents the nonlifting surface and flow field pressure distributions at $M_\infty = 1$ for the wing-circular body configuration which was planned for experimental evaluation as discussed above, while figure 9 exhibits analogous results for a wing-body combination composed of a parabolic-arc body having an elliptic cross section that maintains a constant ratio of major to minor axis $\lambda = 3$ but with a wing and an equivalent body identical to that of the configuration studied in figures 4 through 7.

In figure 7, the extremely rapid variations in surface pressure displayed near the body midpoint are due to the discontinuity in slope of the indented body at that point. (This discontinuity occurs since in order to keep the equivalent body area distribution together with its corresponding derivatives smooth, it is necessary for the indented body to have a slope discontinuity at $x/l = 0.5$ to compensate for the one due to the wing.) The flow field pressure distributions given in that figure point out that this peaky behavior persists well into the flow field. Consequently, the rapid variational nature of these results indicates that wing configurations of this type with the attendant body slope discontinuities are probably not well-suited for experimental verification of the theory and that configurations having wings with

straight trailing edges which cause no indented body slope discontinuities would be more satisfactory.

The surface pressure distributions presented in figure 9 for the wing-indented elliptic body combination described above are similar in behavior to those shown in figure 4 for the corresponding circular body, with the one exception being a small neighborhood near the rear of the indentation in which a slight expansion occurs in an otherwise monotonic compression. This is undoubtedly caused by the occurrence of a zero body slope on the indented body in that region. The flow field distributions given in that figure indicate that this behavior persists into the flow field so that at $r/D = 4$ it still produces a slight asymmetry in an almost axisymmetric flow field. We note that in reference 3 it was shown that for a smooth elliptic body alone having $\lambda = 3$ the flow field becomes essentially axisymmetric at $r/D = 1$.

Bumpy and Indented Bodies

The experimental surface pressure distribution at $M_\infty = 0.8$ from reference 32 together with the theoretical results provided by integrating the local linearization equation for purely subsonic flow (eq. (109)) and then using equation (3) with $\alpha = 0$ are shown in the lower plot in figure 10 for a body of revolution consisting of a basic parabolic-arc shape having a thickness ratio $D/\ell = 1/14$ and a bump with ordinates described by equation (89) superimposed upon its midsection. The axial extent of the bump runs from $x_1/\ell = 0.393$ to $x_2/\ell = 0.607$, and its maximum height is equal to 10 percent of the maximum basic body diameter, so that for this case $\Delta R_{\max}/\ell = 1/140$. Results are given in the upper plot in figure 10 for the corresponding indented body. It can be seen from these two figures that while the theoretical curves follow the general trend of the data reasonably well, discrepancies with the experimental results are evident for the compression and/or expansion peaks. In the case of the bumpy body, the theory underpredicts the compression peaks near the start and end of the bump, and it underpredicts the expansion at the crest of the bump. For the indented body, the expansion peaks near the beginning and end of the indentation are underestimated, while the compression peak at the trough of the indentation is in good agreement with the data.

Corresponding results for these same bodies are given in figure 11 for purely supersonic flow. The experimental pressure distribution for $M_\infty = 1.20$ from reference 32 together with that obtained from integrating the set of supersonic local linearization expressions (eq. (112)) are shown in the lower plot of figure 10 for the bumpy parabolic-arc body and in the upper plot for the indented one. Again, while the theory follows the trend of the experimental results, the compression and expansion peaks are generally not well predicted. For the bumpy body, we note that the compression peak at the start of the bump is underestimated while the expansion crest is far overpredicted. Because of this large over expansion, the pressure is unable to recover sufficiently on the rear of the bump, so that when the point $x = x_2 + \beta R$ is reached and the transfer made to the last of the set of three differential equations in equation (112), the resultant expansion over the rear of the basic parabolic-arc body carries the theoretical result far above the data. A similar behavior is evident for the indented body shown in figure 11. Here the expansion peak at the start of the indentation is somewhat underpredicted, the compression peak at the trough of the indentation is in good agreement with the data, but the expansion near the rear of the bump is too large resulting in the same general behavior over that portion of the body as evidenced in the case of the bumpy body.

For these supersonic flows we also note that the occurrence of two effects not present in the corresponding subsonic cases. First, because for supersonic flows information regarding the body (or any field point, for that matter) is transmitted along the nonlinear characteristics defined by

$$\frac{dx}{dr} = \beta \quad (116)$$

and since the sources representing the body are placed on the axis rather than the surface, the theoretical surface pressure distribution lags the body geometry by approximately βR . In comparisons with data, this phenomenon is most clearly evident in figure 11 at points near the beginning of the bump or indentation and somewhat less noticeable at the rear of these distortions. Second, although the surface velocity is continuous, the discontinuities in the second derivative of the area

distribution $S''(x)$ at x_1 and x_2 result in singularities in the fluid acceleration on the body, du_s/dx , at the points

$$x = x_1 + \beta R \quad (117)$$

$$x = x_2 + \beta R$$

i.e., the locations at which transfer is made between the various differential forms in equation (112). We note the presence of these singularities by the rapid variation in the predicted pressure coefficients shown in figure 11 in the regions immediately behind those two points. It is important to realize that these singularities are not unique to the local linearization method but occur as well in the linearized solution. This point is discussed in more detail below.

With regard to the discrepancies in peak values which occur in both the subsonic and supersonic comparisons, there exist two possible sources which may be acting separately or in combination. One factor is the inability of sources and sinks located on the body axis (rather than on the body surface) to represent adequately the flow behavior caused by the relatively rapid change in body geometry in those regions. The other factor involves the occurrence of sudden curvature changes on these bodies which could result in the violation, over a significant portion of the body length, of one of the basic assumptions made in deriving the local linearization equations (109) and (112), i.e. that the fluid acceleration on the body surface du_s/dx remains small.

As might be expected, both of these factors are more strongly evident for the supersonic cases studied than for the corresponding subsonic ones. Thus, the greatest effect on the local linearization solutions of these factors can be evaluated by comparing those solutions to the related linearized supersonic solutions.

Starting with the expression for the linearized solution

$$\frac{u_\ell}{U_\infty} = -\frac{1}{2\pi} \int_0^{x-\beta_\ell R} \frac{\bar{S}''(\xi) d\xi}{\sqrt{(x-\xi)^2 - \beta_\ell^2 R^2}} - \frac{1}{2\pi} \int_{x_1}^{x-\beta_\ell R} \frac{\Delta S''(\xi) d\xi}{\sqrt{(x-\xi)^2 - \beta_\ell^2 R^2}} \quad (118)$$

it is possible to derive the following form valid within the approximations of slender body theory,

$$\frac{u_\ell}{U_\infty} = \frac{\bar{S}''(x)}{2\pi} \ln \left(\frac{\beta_\ell R}{2x} \right) + \frac{1}{2\pi} \int_0^x \frac{\bar{S}''(x) - \bar{S}''(\xi)}{x - \xi} d\xi \quad (0 < x \leq x_1 + \beta_\ell R)$$

$$\begin{aligned} \frac{u_\ell}{U_\infty} = & \frac{\bar{S}''(x)}{2\pi} \ln \left(\frac{\beta_\ell R}{2x} \right) + \frac{1}{2\pi} \int_0^x \frac{\bar{S}''(x) - \bar{S}''(\xi)}{x - \xi} d\xi \\ & + \frac{1}{2\pi} \int_{x_1}^{x - \beta_\ell R} \frac{\Delta S''(x) - \Delta S''(\xi)}{x - \xi} d\xi + \frac{\Delta S''(x)}{2\pi} \ln \left(\frac{\beta_\ell R}{x - x_1 + \sqrt{(x - x_1)^2 - \beta_\ell^2 R^2}} \right) \\ & (x_1 + \beta_\ell R \leq x \leq x_2 + \beta_\ell R) \end{aligned}$$

$$\begin{aligned} \frac{u_\ell}{U_\infty} = & \frac{\bar{S}''(x)}{2\pi} \ln \left(\frac{\beta_\ell R}{2x} \right) + \frac{1}{2\pi} \int_0^x \frac{\bar{S}''(x) - \bar{S}''(\xi)}{x - \xi} d\xi \\ & + \frac{1}{2\pi} \int_{x_1}^{x_2} \frac{\Delta S''(x) - \Delta S''(\xi)}{x - \xi} d\xi + \frac{\Delta S''(x)}{2\pi} \ln \left(\frac{x - x_2 + \sqrt{(x - x_2)^2 - \beta_\ell^2 R^2}}{x - x_1 + \sqrt{(x - x_1)^2 - \beta_\ell^2 R^2}} \right) \\ & (x_2 + \beta_\ell R \leq x < \ell) \end{aligned} \quad (119)$$

From these expressions, it is clear that while the linearized velocity, u_ℓ/U_∞ is continuous on the body surface, its first derivative du_ℓ/dx is not and has, in fact, a square root singularity at the points $x = x_1 + \beta_\ell R$ and $x = x_2 + \beta_\ell R$. These singularities will always occur at points where the body curvature is discontinuous. The linearized pressure distribution given by equations (119) and (3) with $\alpha = 0$ have been calculated for the two bodies under consideration and are presented in figure 12. For the case of the bumpy body shown in the lower plot of figure 12 it is immediately apparent that the linear solution follows the data more closely than the local linearization

solution in the region near the crest of the bump and also further aft of it. However, in addition to the βR lag mentioned previously, the linear solution still slightly underpredicts the compression peak at the start of the bump and while it reaches the proper level in the region farther behind the bump, it badly overpredicts the compression near $x = x_2 + \beta R$. A similar behavior is noted for the indented body shown in figure 11 where, as in the case of the bumpy body, the pressure in the vicinity of the rear of the indentation is badly overpredicted. Two conclusions can immediately be drawn. First, the better general agreement exhibited by the linear solution as compared with the local linearization solutions indicates that the large accelerations induced by the rapid curvature changes extend over a substantial portion of the body, and, therefore, cannot be assumed negligible. Secondly, the discrepancies near the start and end of the distortions clearly demonstrate the inadequacy of the slender body approximation in accounting for the rapid changes in surface geometry associated with these distortions and suggest that a quasi-cylindrical theory is necessary. Before discussing a quasi-cylindrical approach to the problem, however, one final point with regard to the slender body approach should be made. In the derivation of the local linearization equation (112) and also the linearized equation (119), several terms were approximated within the framework of slender body theory. The question could be raised whether these approximations may in fact cause the discrepancies with data rather than the placement of sources and sinks on the body axis.

To investigate this possibility the "exact" linear solution given by equation (118) was determined together with the corresponding "exact" local linearization solution, which is given by the expression,

$$\begin{aligned} \frac{d}{dx} \left(\frac{u}{U_\infty} \right) = \frac{d}{dx} \left(\frac{u}{U_\infty} \right)_1 = & - \frac{\bar{S}''(0)}{2\pi} \frac{\left(1 - \frac{x}{R} \frac{dR}{dx} \right)}{\sqrt{x^2 - \beta^2 R^2}} - \frac{\bar{S}'''(x - \beta R)}{2\pi} \left[\ln \left\{ \frac{x + \sqrt{x^2 - \beta^2 R^2}}{\beta R} \right\} \right. \\ & \left. + \frac{\sqrt{x^2 - \beta^2 R^2}}{R} \frac{dR}{dx} \right] + \frac{1}{2\pi} \int_0^{x - \beta R} \frac{(\bar{S}'''(x - \beta R) - \bar{S}'''(\xi))}{\sqrt{(x - \xi)^2 - \beta^2 R^2}} \left(1 - \frac{x - \xi}{R} \frac{dR}{dx} \right) d\xi \\ & (x \leq x_1 + \beta R) \end{aligned}$$

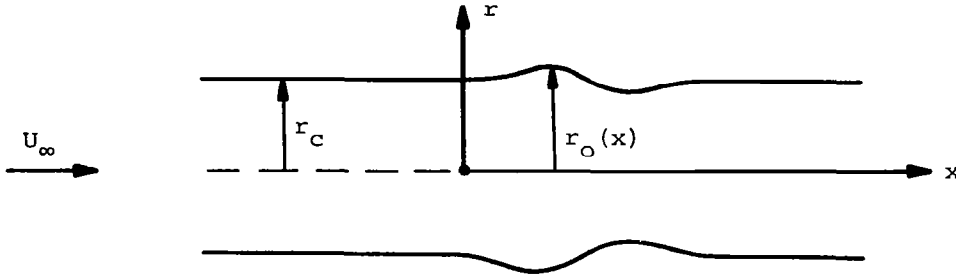
(Continued on next page)

$$\begin{aligned}
\frac{d}{dx} \left(\frac{u}{U_\infty} \right) &= \frac{d}{dx} \left(\frac{u}{U_\infty} \right)_1 - \frac{\Delta S''(x_1)}{2\pi} \frac{\left(1 - \frac{x-x_1}{R} \frac{dR}{dx}\right)}{\sqrt{(x-x_1)^2 - \beta^2 R^2}} \\
&\quad - \frac{\Delta S'''(x-\beta R)}{2\pi} \left\{ \ln \left[\frac{x-x_1 + \sqrt{(x-x_1)^2 - \beta^2 R^2}}{\beta R} \right] + \frac{\sqrt{(x-x_1)^2 - \beta^2 R^2}}{R} \frac{dR}{dx} \right\} \\
&\quad + \frac{1}{2\pi} \int_{x_1}^{x-\beta R} \frac{(\Delta S'''(x-\beta R) - \Delta S'''(\xi))}{\sqrt{(x-\xi)^2 - \beta^2 R^2}} \left(1 - \frac{x-\xi}{R} \frac{dR}{dx}\right) d\xi \\
&\hspace{15em} (x_1 + \beta R \leq x \leq x_2 + \beta R)
\end{aligned}$$

$$\begin{aligned}
\frac{d}{dx} \left(\frac{u}{U_\infty} \right) &= \frac{d}{dx} \left(\frac{u}{U_\infty} \right)_1 + \frac{\Delta S''(x_2)}{2\pi} \frac{\left(1 - \frac{x-x_2}{R} \frac{dR}{dx}\right)}{\sqrt{(x-x_2)^2 - \beta^2 R^2}} - \frac{\Delta S''(x_1)}{2\pi} \frac{\left(1 - \frac{x-x_1}{R} \frac{dR}{dx}\right)}{\sqrt{(x-x_1)^2 - \beta^2 R^2}} \\
&\quad - \frac{\Delta S'''(x-\beta R)}{2\pi} \left\{ \ln \left[\frac{x-x_1 + \sqrt{(x-x_1)^2 - \beta^2 R^2}}{x-x_2 + \sqrt{(x-x_2)^2 - \beta^2 R^2}} \right] \right. \\
&\quad \left. + \left[\frac{\sqrt{(x-x_1)^2 - \beta^2 R^2} - \sqrt{(x-x_2)^2 - \beta^2 R^2}}{R} \right] \frac{dR}{dx} \right\} \\
&\quad + \frac{1}{2\pi} \int_{x_1}^{x_2} \frac{\Delta S'''(x-\beta R) - \Delta S'''(\xi)}{\sqrt{(x-\xi)^2 - \beta^2 R^2}} \left(1 - \frac{x-\xi}{R} \frac{dR}{dx}\right) d\xi \\
&\hspace{15em} (x_2 + \beta R \leq x < l) \\
&\hspace{18em} (120)
\end{aligned}$$

where $d(u/U_\infty)_1/dx$ represents the contribution from the basic body. These results are presented in figure 13 for the bumpy body and indicate that the results become even more spurious than those of the approximated equations. Consequently, we conclude that slender body theory is simply not adequate to cope with these classes of shapes and recourse must be made to quasi-cylindrical theory.

While only very preliminary work has been done along analytical lines for developing a quasi-cylindrical theory at transonic speeds (see ref. 46), Nielsen (refs: 47, 48) has investigated in depth the linearized quasi-cylindrical supersonic problem. For that situation, it can be shown that the pressure distribution due to an axisymmetric distortion $r_o(x)$ of a cylinder of radius r_c



is given by

$$c_p = \frac{2}{\beta_\ell} \left[\frac{dr_o(x)}{dx} - \frac{1}{\beta_\ell r_c} \int_0^x \frac{dr_o(\xi)}{d\xi} w_o \left(\frac{x-\xi}{\beta_\ell r_c}; 1 \right) d\xi \right] \quad (121)$$

where the interference function w_o is defined as

$$w_o(x, r) \equiv L^{-1} \left[e^{s(r-1)} \frac{K_m(sr)}{K_m'(s)} + \frac{1}{\sqrt{r}} \right] \quad (122)$$

L^{-1} signifies the inverse Laplace transform of the bracketed quantity and $K_m(x)$ is the modified Bessel function of the second kind of order m . This formulation was applied to the bumpy and indented bodies under consideration by passing a quasi-cylinder through the maximum thickness point of the basic parabolic-arc body and then assuming that the pressure distribution due to the basic body alone (which is nearly constant in the region near the midsection) could be calculated by using linearized slender body theory, while that of the distortion could be found from equation (121) with $r_c = D/2$. The results of this calculation are

shown in figure 14. The good agreement at all intermediate and peak values for the compressions and expansions on both bodies is evident. Moreover, no βR lag exists as in the case of purely axial distributions of sources and sinks with the consequence that the surface geometry and pressure are now "in phase." Consequently, for the particular shapes under consideration a quasi-cylindrical theory does accurately predict the surface and flow field properties. In order to calculate the $M_\infty \approx 1$ case, it is necessary to develop the corresponding quasi-cylindrical local linearization solutions.

Before describing a possible procedure for carrying this out, one final point with regard to the slender body approach should be made. Although the slender body approximation is not valid for the present shapes (which have a maximum height of the distortion ΔR_{\max} equal to one-tenth of the maximum body diameter) there does exist some smaller distortion height at which that approximation would be accurate. Knowledge of this height is important since, if the additional cross-sectional area of the bump is associated with the area of finite thickness wing, then it is of interest to determine what limitations are imposed on the span and thickness of that wing by this constraint. A good estimate for the largest value of ΔR_{\max} at which slender body theory remains valid can be found by calculating (by the method of local linearization) the flow at $M_\infty = 1$ for the basic parabolic-arc body up to $x = x_1$, transferring at that point to the hyperbolic equation (112), and then integrating toward the tail with successively smaller values of ΔR_{\max} until the flow over the entire distortion does not change character, i.e. remains supersonic rather than oscillating between subsonic and supersonic as shown in the two figures on page 52. These calculations were carried out and it appears that for the above behavior to prevail the value of ΔR_{\max} must be smaller than its present value by an order of magnitude. Now if the cross-sectional area of the bump is associated with the area of, say, a simple triangular planform wedge wing of thickness/chord ratio $t/c = 0.04$ and root chord equal to one-half the body length, then the maximum semispan of this wing is 1.5 times the maximum body diameter for the original value of ΔR_{\max} --already a small enough value to be of only marginal practical value. Reducing the size of ΔR_{\max} by an order of magnitude would reduce the maximum span to 0.75 times the maximum body diameter, so that the slender body solution would have little practical significance.

A logical procedure for developing the local linearization method in the quasi-cylindrical sense at $M_\infty \approx 1$ would be to determine first the corresponding nonlinear subsonic and supersonic solutions. The general theoretical approach to solving the supersonic case is clear. If the same technique for deriving the local linearization solution used in the slender body axisymmetric flows (i.e. assuming small surface accelerations) is again employed for the quasi-cylindrical case, then direct application to equation (121) leads to the following expression for purely supersonic flows

$$\frac{d}{dx} \left(\frac{u}{U_\infty} \right) = - \frac{1}{\beta} \left[\frac{d^2 r_o(x)}{dx^2} - \frac{1}{\beta r_c} \int_0^x \frac{d^2 r_o(\xi)}{d\xi^2} w_o \left(\frac{x-\xi}{\beta r_c}, 1 \right) d\xi \right] \quad (123)$$

where β is given by equation (110). However, we have applied equation (123) to the bodies studied herein and it appears that the assumption of small surface accelerations should not be made. Consequently, the local linearization theory would have to be rederived along these lines. Application to purely subsonic quasi-cylindrical flows would follow the same general technique used in deriving the supersonic result and would start with the analogous subsonic expression corresponding to equation (121). In this case, the interference function would involve inverse Fourier transforms of Bessel functions of the first kind $J_m(x)$ rather than the inverse Laplace transforms of modified Bessel functions of the second kind $K_m(x)$ (as given by equation (122)). Solution of the $M_\infty \approx 1$ case would then involve consideration of the parabolic heat equation for accelerating flows given in reference 9 but now satisfying boundary conditions on a cylindrical surface rather than on the body axis. Treatment of regions of decelerating flow for this case would involve use of the limiting forms ($M_\infty \rightarrow 1$) of the quasi-cylindrical subsonic and supersonic solutions discussed above. While there remain several questions of detail, the versatility of the local linearization method as shown by its successful application to thin airfoils (ref. 3, 21), slender bodies of revolution (refs. 3, 8, 9, 10) and wings of finite span (ref. 49) strongly suggests that this theory should be developed in the quasi-cylindrical sense and that the resultant predictions will be both accurate and useful in a variety of significant aerodynamic applications.

CONCLUDING REMARKS

Analysis and development of associated computer programs have been conducted in order to develop calculative techniques for predicting properties of transonic flows about certain classes of slender wing-body combinations. The theoretical analysis is based upon a combination of the local linearization method and the transonic equivalence rule and applies to flows with free stream Mach numbers $M_\infty \approx 1$, below the lower critical, and above the upper critical.

Computational programs, which are documented under separate cover in a general user's manual, have been developed for finite thickness wing-body combinations in which the bodies are area-rule indented in such a manner that the resultant equivalent bodies remain smooth. These indented bodies are derived from two basic types of smooth body shapes, i.e.,

- Bodies of revolution having $R \sim x/\ell - (x/\ell)^n$ or $1 - x/\ell - (1 - x/\ell)^n$
- Parabolic-arc bodies having elliptic cross sections which maintain a constant ratio $\lambda (=a/b)$ of major to minor axes along the entire body length

The general class of wings considered are symmetric in planform about the azimuthal body meridian ($x - z$ plane) and consist of straight leading and trailing edges swept at arbitrary angles (with the restriction that the trailing edge be either straight or swept-forward), with the positions of the leading and trailing edges of the root-chord located at arbitrary locations on the body axis, and with profiles described by $Z_w \sim \frac{\bar{x}}{c_w} - (\frac{\bar{x}}{c_w})^m$ or $1 - \frac{\bar{x}}{c_w} - (1 - \frac{\bar{x}}{c_w})^m$ where \bar{x} is the axial distance from the leading edge and c_w is the local chord.

These programs provide longitudinal pressure distributions for both nonlifting and lifting situations, at arbitrary angular positions in the cross flow plane at points along the body and wing surface and also along lines parallel to the body axis but removed at arbitrarily-specified lateral distances from it. In addition to the pressure distributions, the aerodynamic characteristics of lift, drag, and pitching moment are also provided.

The theoretical pressure distributions predicted by these programs for certain members of the class of configurations described above indicate quantitatively the relatively large effects of wing thickness and lift on

both the body and flow field pressures, and also serve to point out the singularities characteristic to the theory as it is presently constituted. In addition, these results demonstrate the rapidity with which the flow field becomes axisymmetric and equal to that about the equivalent body. Finally, it is observed that wing-body combinations having wings with swept-forward rather than straight trailing edges produce very peaky surface and flow field pressure distributions and, consequently, are not as well suited for experimental verification of the theory as combinations having wings with straight trailing edges.

Comparisons of theoretical and experimental results for axisymmetric bodies having bumps (or indentations) superimposed upon an otherwise smooth profile demonstrate the inadequacy of the slender body approximation of placing sources and sinks on the body axis rather than the surface to account for the rapid changes in geometry associated with these distortions; furthermore, these results suggest that a quasi-cylindrical theory is necessary to determine flows about these classes of shapes. Calculation of the linearized quasi-cylindrical supersonic solution confirms this conjecture. Moreover, comparisons of the linear and local linearized solutions indicate that large accelerations extending over a substantial portion of the body length are caused by the rapid curvature changes of these distortions, so that a modification of the local linearization method (which as presently constituted assumes small surface accelerations) is required in applications to these types of shapes. Nevertheless, development of that method in the quasi-cylindrical sense appears feasible, and its already demonstrated versatility and success in previous two- and three-dimensional applications strongly suggests the usefulness and importance of this as a contribution to modern transonic theory.

In conclusion, we emphasize that the techniques employed to obtain the results for the wing-body combinations presented here are not restricted to the particular classes of wings and bodies selected for study in this report, but possess much greater generality. Moreover, the solutions to the two-dimensional cross flow problems given are independent of Mach number and, consequently, can be combined with solutions other than those provided by the local linearization method (for example, finite difference solutions) for transonic flow about the nonlifting equivalent body. We suggest, furthermore, that experimental work be conducted to determine surface and flow-field pressure distributions on selected wing-

body combinations in order to more clearly define the extent to which the theory applies to configurations of this nature and, also, that consideration be given to developing the local linearization method in the quasi-cylindrical sense in order that theoretical results can be determined for transonic flows about practically important shapes of this category.

Nielsen Engineering & Research, Inc.
Mountain View, California
November, 1971

REFERENCES

1. Spreiter, J. R., Stahara, S. S., and Frey, W. H.: Calculative Techniques for Transonic Flows. NASA SP-228, 1969, pp. 53-73.
2. Spreiter, J. R. and Stahara, S. S.: Developments in Transonic Flow Theory. Zeits. für Flugwiss., Bd. 18, Heft 2/3, 1970, pp. 33-40.
3. Spreiter, J. R. and Stahara, S. S.: Calculative Techniques for Transonic Flows About Certain Classes of Airfoils and Slender Bodies. NASA CR-1722, 1971.
4. Steger, J. L. and Lomax, H.: Numerical Calculation of Transonic Flow about Two-Dimensional Airfoils by Relaxation Procedures. AIAA Paper No. 71-569, presented at AIAA 4th Fluid and Plasma Dynamics Conference, Palo Alto, Calif. June 21-23, 1971.
5. Bowley, W. W. and Prince, J. F.: Finite Element Analysis of General Fluid Flow Problems. AIAA Paper No. 71-602, presented at AIAA 4th Fluid and Plasma Dynamics Conference, Palo Alto, Calif., June 21-23, 1971.
6. Tai, T. C.: Application of the Method of Integral Relations to Transonic Airfoil Problems. AIAA Paper No. 71-98, presented at AIAA 4th Fluid and Plasma Dynamics Conference, Palo Alto, Calif., June 21-23, 1971.
7. Krupp, J. A. and Murman, E. M.: The Numerical Calculation of Steady Transonic Flows Past Thin Lifting Airfoils and Slender Bodies. AIAA Paper No. 71-566, presented at AIAA 4th Fluid and Plasma Dynamics Conference, Palo Alto, Calif., June 21-23, 1971.
8. Spreiter, J. R.: Aerodynamics of Wings and Bodies at Transonic Speeds. J. Aero-Space Sci., vol. 26, no. 8, Aug. 1969, pp. 465-487.
9. Spreiter, J. R. and Alksne, A.: Slender Body Theory Based on Approximate Solution of the Transonic Flow Equation. NASA TR R-2, 1959.
10. Spreiter, J. R., Smith, D. W., and Hyett, B. J.: A Study of the Simulation of Flow with Free-Stream Mach Number 1 in a Choked Wind Tunnel. NASA TR R-73, 1960.
11. Heaslet, M. A. and Spreiter, J. R.: Three-Dimensional Transonic Flow Theory Applied to Slender Wings and Bodies. NACA Rep. 1318, 1957.
12. Spreiter, J. R.: On the Application of Transonic Similarity Rules to Wings of Finite Span. NACA Rep. 1153, 1953. (Supersedes NACA TN 2726).
13. Liepmann, H. W. and Roshko, A.: Elements of Gasdynamics. John Wiley and Sons, Inc., New York, N. Y., 1957, pp. 202-205.

14. Oswatitsch, K.: Die Theoretischen Arbeiten Über Schallnahe Strömungen am Flugtechnischen Institut der Kungl. Tekniska Högskolan, Stockholm. Proc. Eighth Int. Cong. on Theo. and Appl. Mech., 1953.
15. Spreiter, J. R.: Theoretical and Experimental Analysis of Transonic Flow Fields. NACA-University Conference on Aerodynamics, Construction, and Propulsion, Vol. II, "Aerodynamics," 1954, pp. 18/1 - 18/17.
16. Spreiter, J. R.: The Aerodynamic Forces on Slender Plane and Cruciform-Wing and Body Combinations. NACA Rep. 962, 1950.
17. Heaslet, M. A., Lomax, H., and Spreiter, J. R.: Linearized Compressible-Flow Theory for Sonic Flight Speeds. NACA Rep. 956, 1950.
18. Taylor, R. A. and McDevitt, J. B.: Pressure Distributions at Transonic Speeds for Parabolic-Arc Bodies of Revolution Having Fineness Ratios of 10, 12, and 14. NACA TN 4234, 1958.
19. McDevitt, J. B. and Taylor, R. A.: Pressure Distributions at Transonic Speeds for Slender Bodies Having Various Axial Locations of Maximum Diameter. NACA TN 4280, 1958.
20. McDevitt, J. B. and Taylor, R. A.: Force and Pressure Measurements at Transonic Speeds for Several Bodies Having Elliptical Cross Sections. NACA TN 4362, 1958.
21. Spreiter, J. R. and Alksne, A.: Thin Airfoil Theory Based on Approximate Solution of the Transonic Flow Equation. NACA Rep. 1359, 1958. (Supersedes NACA TN 3970).
22. Lighthill, M. J.: Supersonic Flow Past Bodies of Revolution. Aero. Res. Council, R. & M. 2003, 1945.
23. Ward, G. N.: Supersonic Flow Past Slender Pointed Bodies. Jour. Mech. and App. Math., vol. II, part 1, 1949, pp. 75-97.
24. Stocker, P. M.: Supersonic Flow Past Bodies of Revolution with Thin Wings of Small Aspect Ratio. Aero. Quart., vol. III, May 1951, pp. 61-79.
25. Spreiter, J. R.: The Aerodynamic Forces on Slender Plane and Cruciform-Wing and Body Combinations. NACA Rep. 962, 1950.
26. Spreiter, J. R. and Sacks, A. H.: A Theoretical Study of the Aerodynamics of Slender Cruciform-Wing Arrangements and Their Wakes. NACA Rep. 1296, 1957.
27. Adams, M. C. and Sears, W. R.: Slender-Body Theory - Review and Extensions. J. Aero. Sci., vol. 20, no. 2, 1953, pp. 85-98.
28. Ashley, H. and Landahl, M.: Aerodynamics of Wings and Bodies. Addison-Wesley Publishing Co., Reading, Mass., 1965, p. 121.

29. Ward, G. H.: Linearized Theory of Steady High-Speed Flow, Cambridge University Press, 1955.
30. Nielsen, J. N.: Missile Aerodynamics. McGraw-Hill Book Co., Inc., New York, N. Y. 1960, p. 30.
31. Byrd, P. F. and Friedman, M. D.: Handbook of Elliptic Integrals. Springer-Verlag, Berlin/Göttingen/Heidelberg, 1954.
32. Taylor, R. A.: Pressure Distributions at Transonic Speeds for Bumpy and Indented Midsections of a Basic Parabolic-Arc Body. NASA Memo. 1-22-59A, 1959.
33. Loving, K. L. and Williams, C. V.: Aerodynamic Loading Characteristics of a Wing-Fuselage Combination Having a Wing of 45° Sweepback Measured in the Langley 8-Foot Transonic Tunnel. NACA RM L52B27, 1952.
34. Bielat, R. P.: A Transonic Wind-Tunnel Investigation of the Aerodynamic Characteristics of Three 4-Percent-Thick Wings of Sweepback Angles 10.8° and 47° , Aspect Ratio 3.5, and Taper Ratio 0.2 in Combination with a Body. NACA RM L52B08, 1952.
35. McDevitt, J. B.: An Experimental Investigation of Two Methods for Reducing Transonic Drag of Swept-Wing and Body Combinations. NACA RM A55B21, 1955.
36. Walker, H. J. and Maillard, W. C.: A Correlation of Airfoil Section Data with the Aerodynamic Loads Measured on a 45° Sweptback Wing Model at Subsonic Mach Numbers. NACA RM A55C08, 1955.
37. McDevitt, J. B. and Haire, W. M.: Investigation at High Subsonic Speeds of a Body-Contouring Method for Alleviating the Adverse Interference at the Root of a Sweptback Wing. NACA TN 3672, 1956.
38. Whitcomb, R. T.: A Study of the Zero-Lift Drag-Rise Characteristics of Wing-Body Combinations Near the Speed of Sound. NACA TR 1273, 1956.
39. McDevitt, J. B.: The Linearized Subsonic Flow About Symmetrical Nonlifting Wing-Body Combinations. NACA TN 3964, 1957.
40. McDevitt, J. B. and Taylor, R. A.: An Investigation of Wing-Body Juncture Interference Effects at Transonic Speeds for Several Swept-Wing and Body Combinations. NACA RM A57A02, 1957.
41. Lomax, H. and Byrd, P.: Theoretical Aerodynamic Characteristics of a Family of Slender Wing-Tail-Body Combinations. NACA TN 2554, 1951.
42. Sears, W. R.: General Theory of High Speed Aerodynamics. Princeton Univ. Press, Princeton, N. J., 1954, pp. 254-275.
43. Mangler, K. W.: Calculation of the Load Distribution Over a Wing with Arbitrary Camber and Twist at Sonic Speed. British A.R.C., R. & M. 3102, 1955.

44. McDevitt, J. B.: A Correlation by Means of Transonic Similarity Rules of Experimentally Determined Characteristics of a Series of Symmetrical and Cambered Wings of Rectangular Planform. NACA TR 1253, 1955.
45. Page, W. A.: Experimental Study of the Equivalence of Transonic Flow About Slender Cone-Cylinders of Circular and Elliptic Cross Section. NACA TN 4233, 1958.
46. Maeder, P. F.: The Linear Approximation to the Transonic Small Disturbance Equation. In Symposium Transsonicum, K. Oswatitsch, ed., Springer-Verlag, Berlin/Göttingen/Heidelberg, 1964, pp. 112-125.
47. Nielsen, J. N.: Supersonic Wing-Body Interference. Ph. D. Thesis, Cal. Inst. of Tech., 1951.
48. Nielsen, J. N.: Tables of Characteristic Functions for Solving Boundary-Value Problems of the Wave Equation with Application to Supersonic Interference. NACA TN 3873, Feb. 1957.
49. Alksne, A. Y. and Spreiter, J. R.: Theoretical Pressure Distributions on Wings of Finite Span at Zero Incidence for Mach Numbers Near 1. NASA Rep. R-88, 1961.

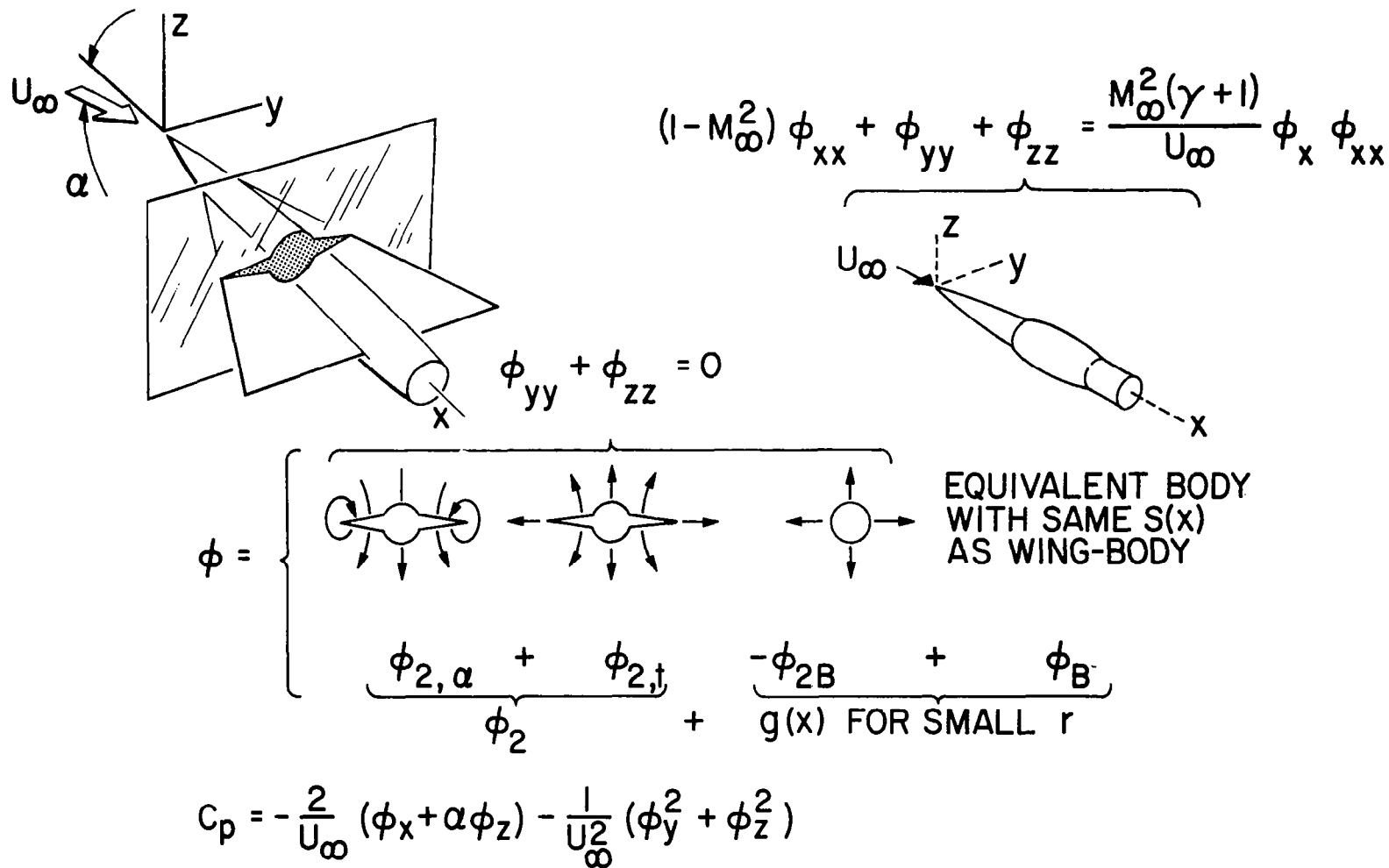


Figure 1.- Transonic equivalence rule for slender wing-body combinations.

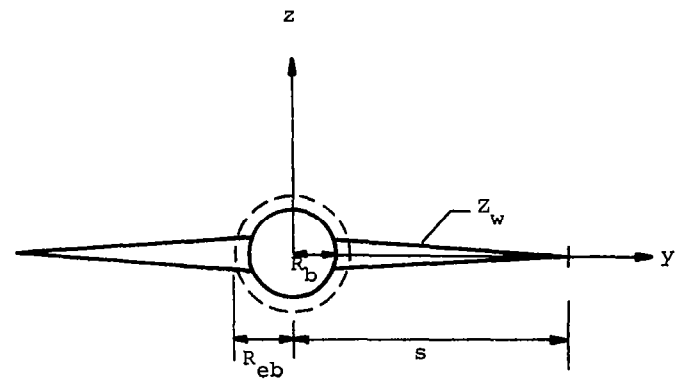


Figure 2.- General configuration of finite thickness wing-indented circular body combinations.

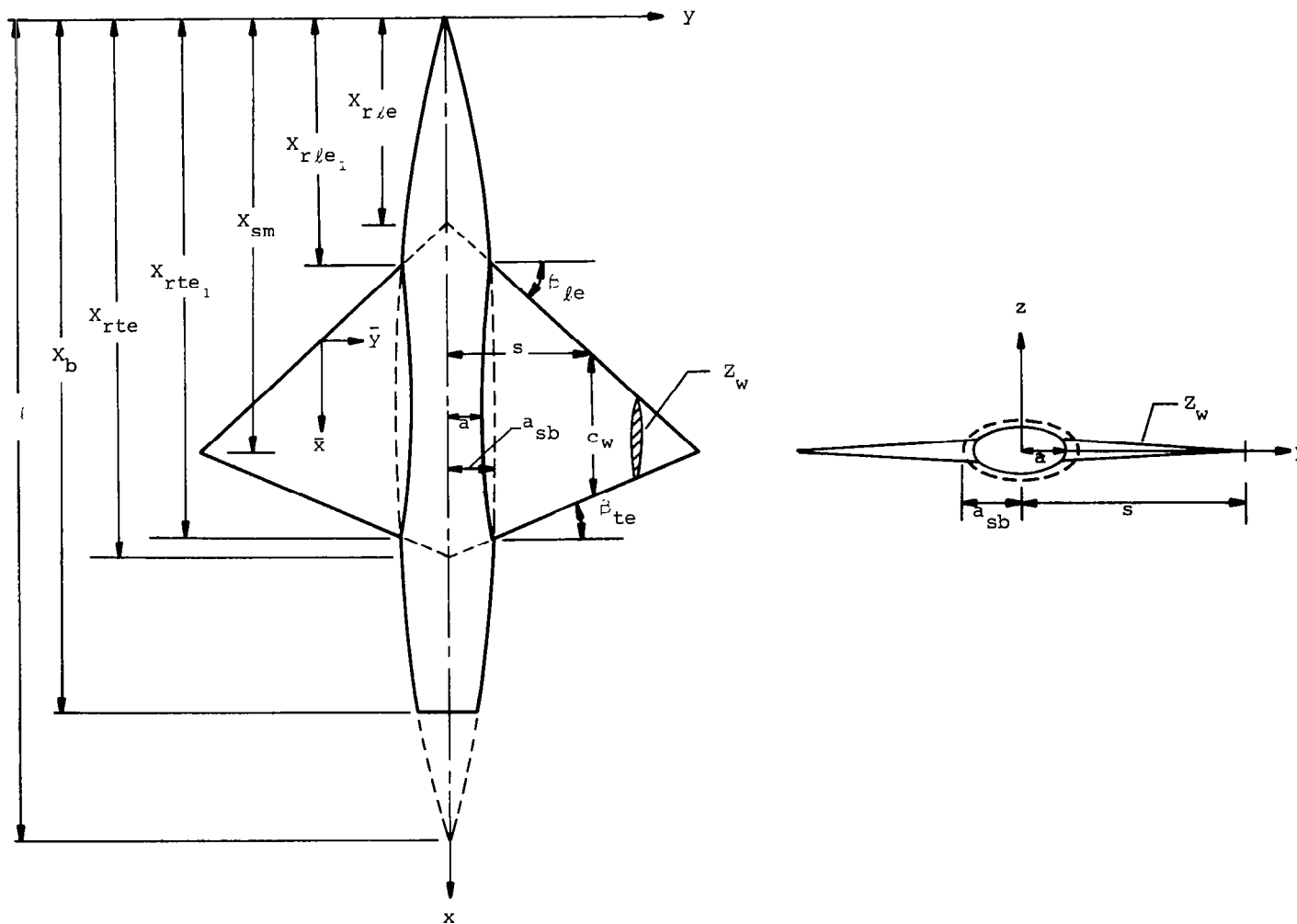


Figure 3.- General configuration of finite thickness wing-indented elliptic body combinations.

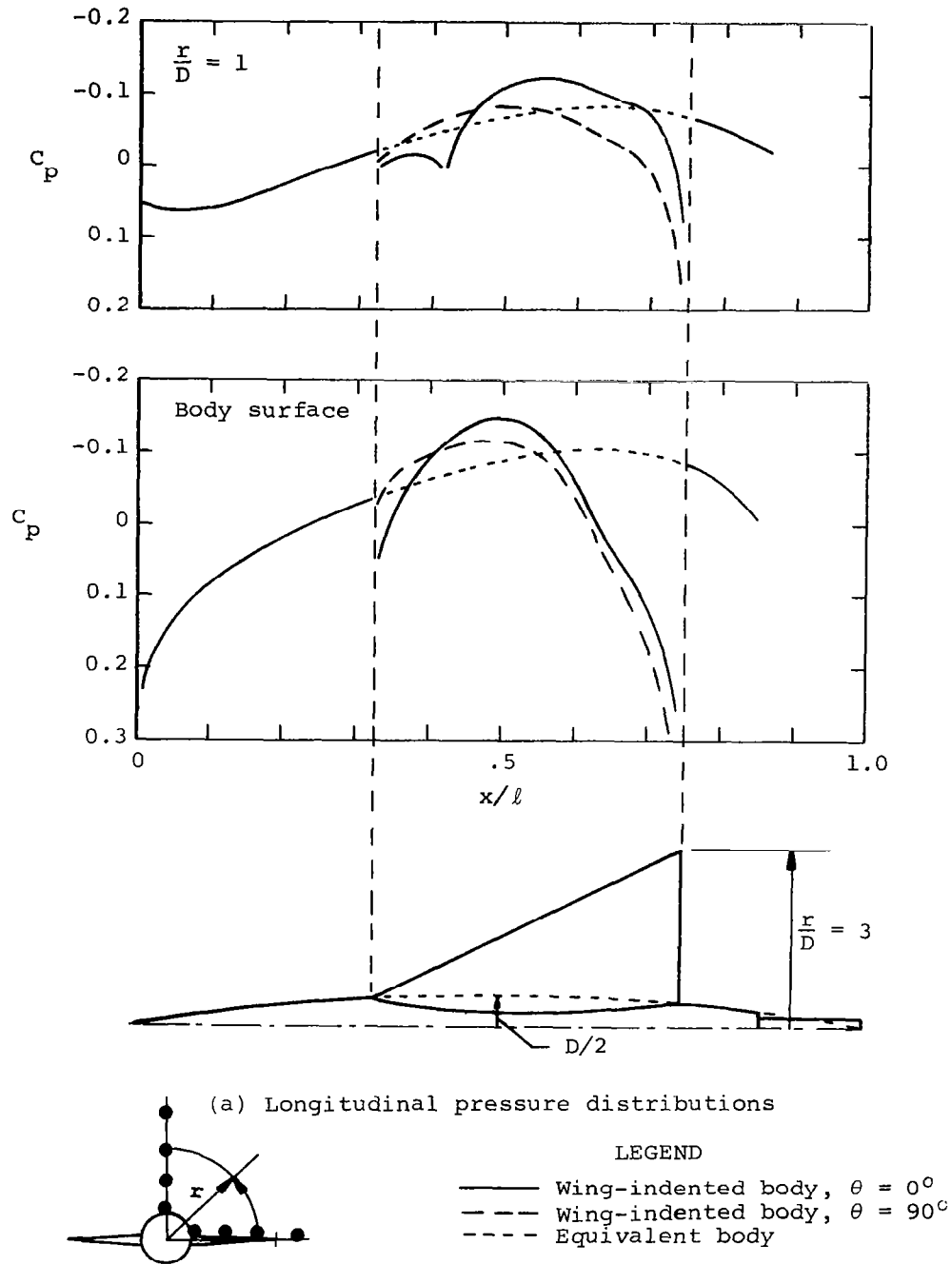


Figure 4.- Theoretical surface and flow field pressure distributions at $M_\infty = 1$ for a nonlifting parabolic-arc profile wing--indented parabolic-arc body combination; equivalent body thickness ratio $D/\ell = 1/12$, wing aspect ratio $AR = 2$, thickness/chord ratio $t/c_w = 0.04$, and with $X_{rle}/\ell = 0.25$
 $X_{rte}/\ell = 0.75$, $X_{b/\ell} = 0.86$.

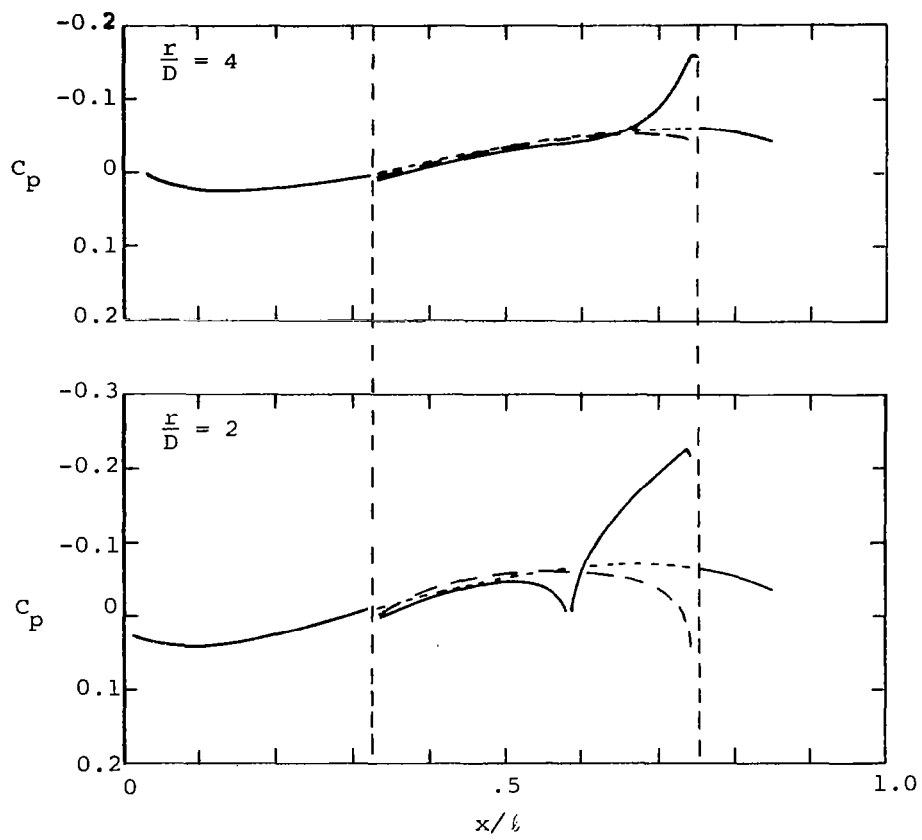
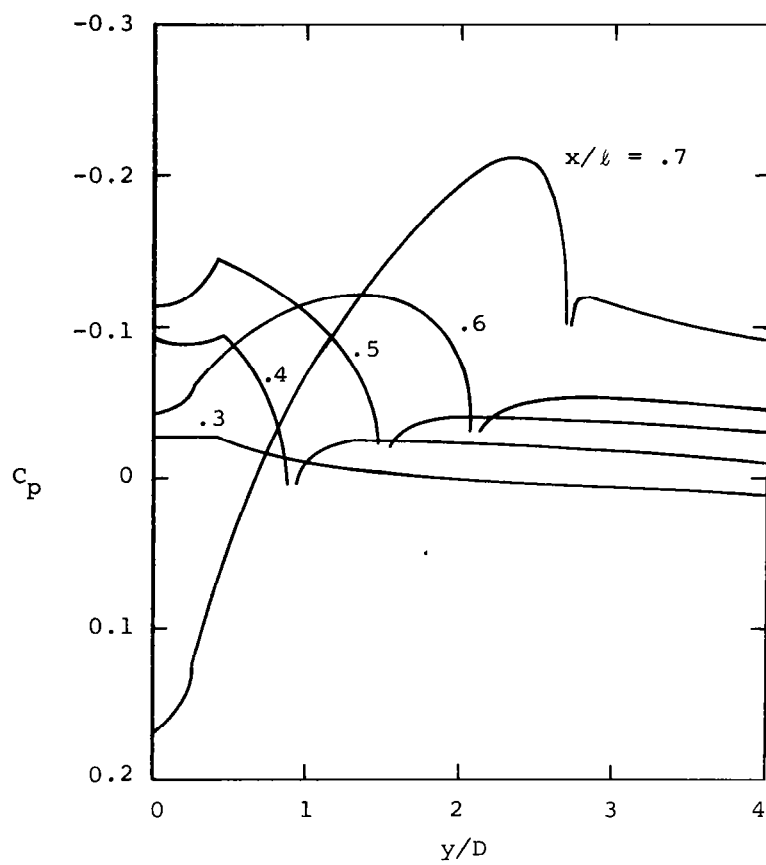
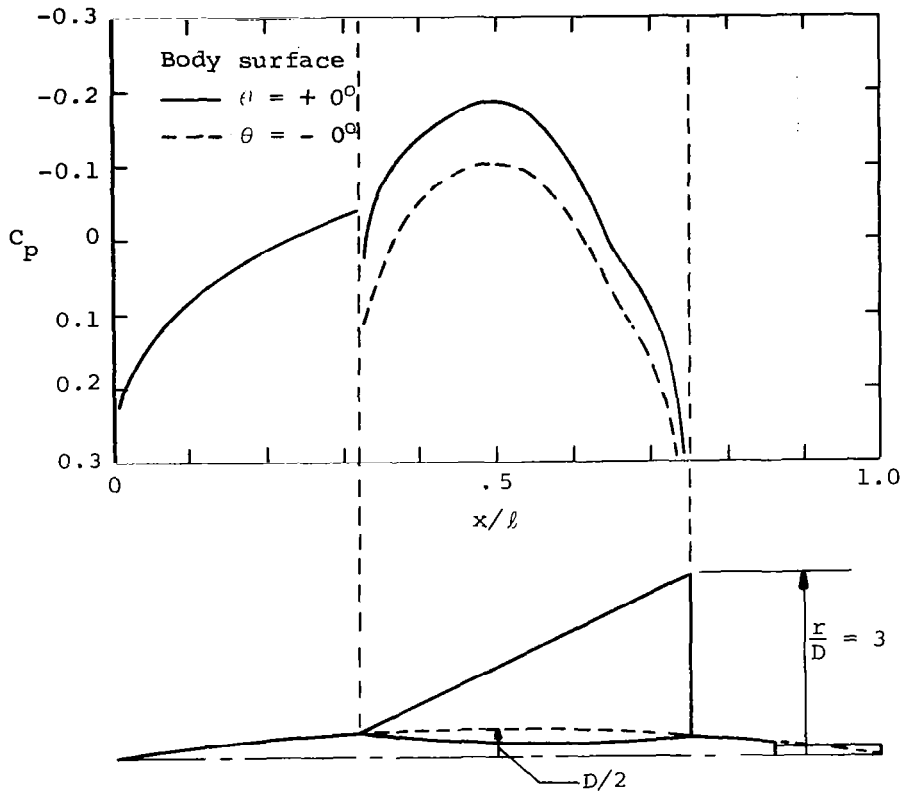


Figure 4.- Continued.



(b) Spanwise pressure distributions

Figure 4.- Concluded



(a) Longitudinal pressure distributions

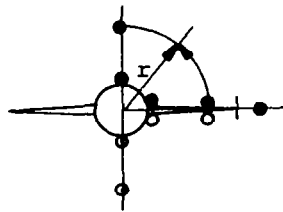
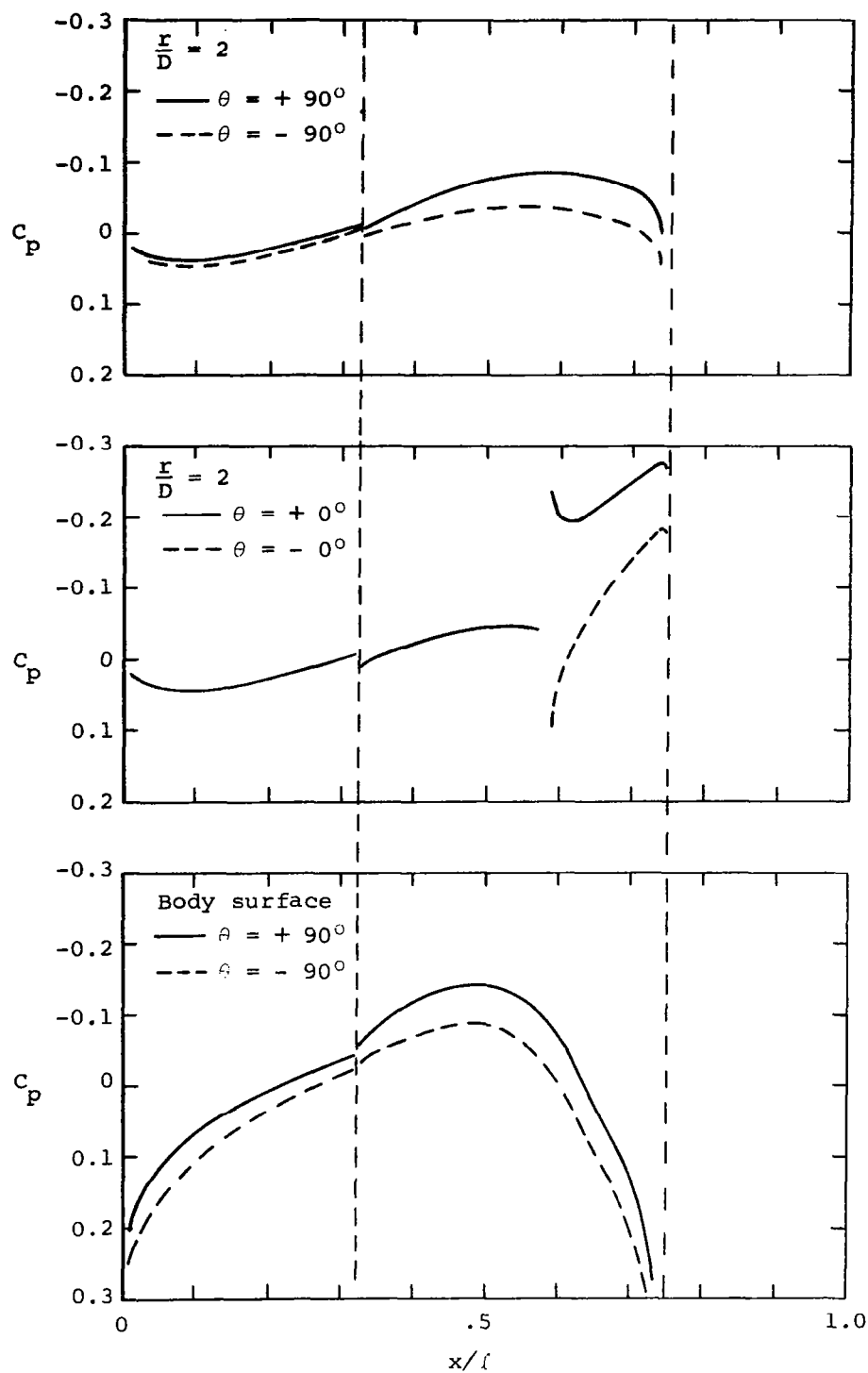


Figure 5.- Theoretical surface and flow field pressure distributions and loadings at $M_\infty = 1$ and $\alpha = 2^\circ$ for a parabolic-arc profile wing--indented parabolic-arc body combination; equivalent body thickness ratio $D/k = 1/12$, wing aspect ratio $AR = 2$, thickness/chord ratio $t/c_w = 0.04$, and with $X_{rte}/l = 0.25$, $X_{rte}/l = 0.75$, $X_b/l = 0.86$.



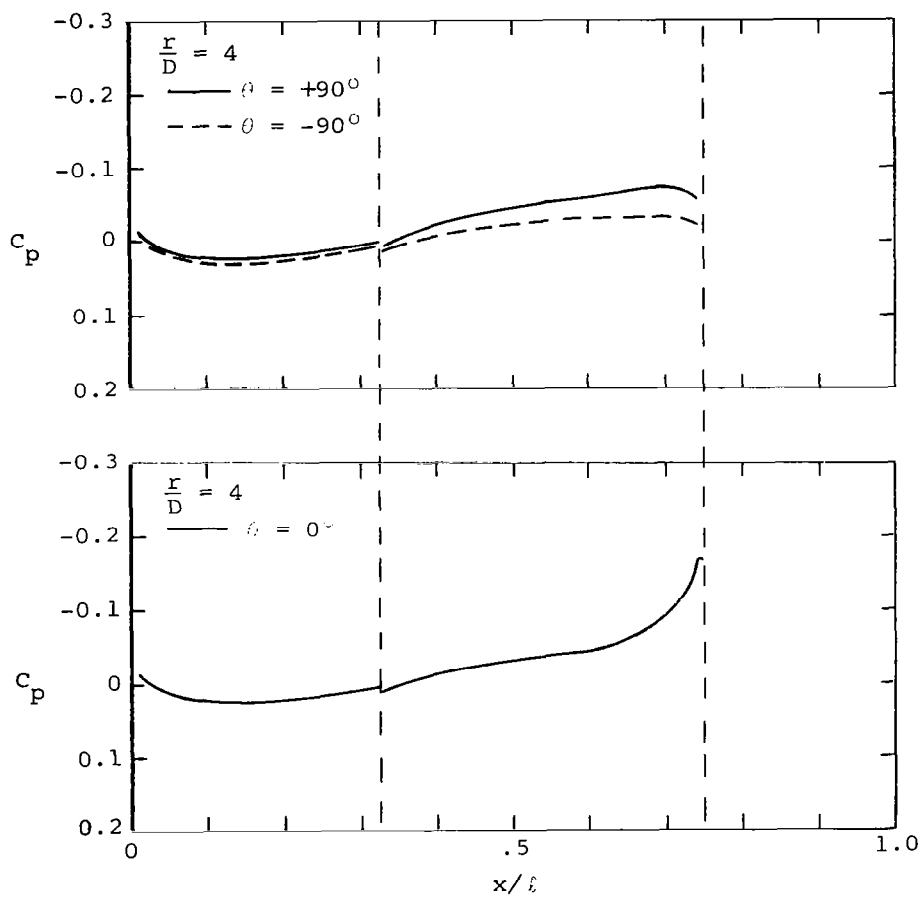
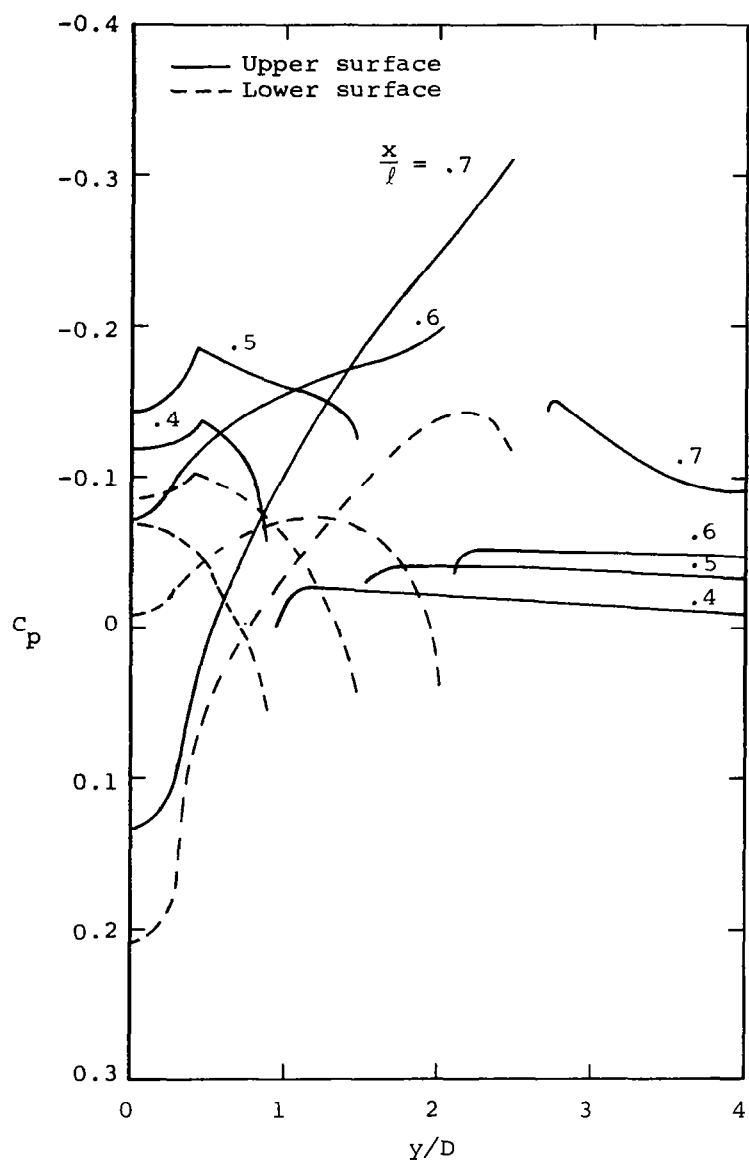
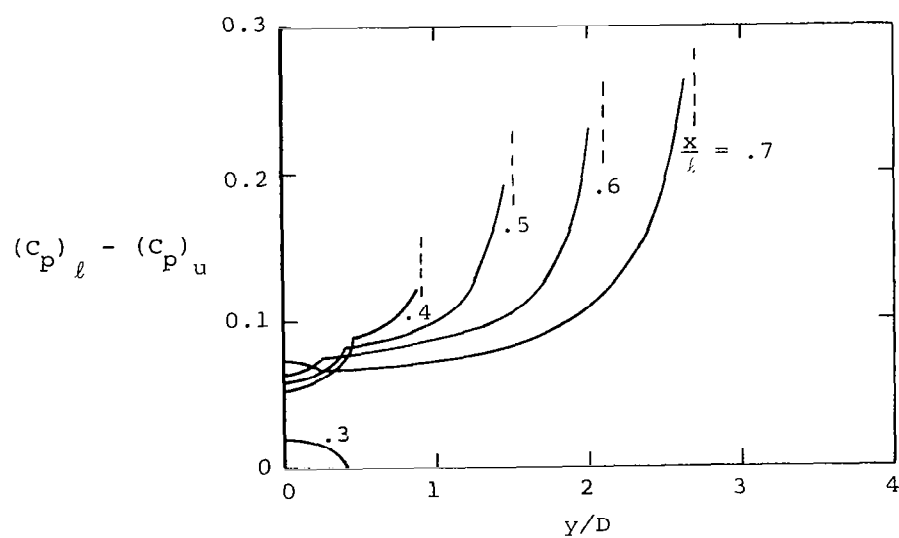


Figure 5.- Continued.



(b) Spanwise pressure distributions

Figure 5.- Continued.



(c) Spanwise loading distributions

Figure 5.- Concluded.

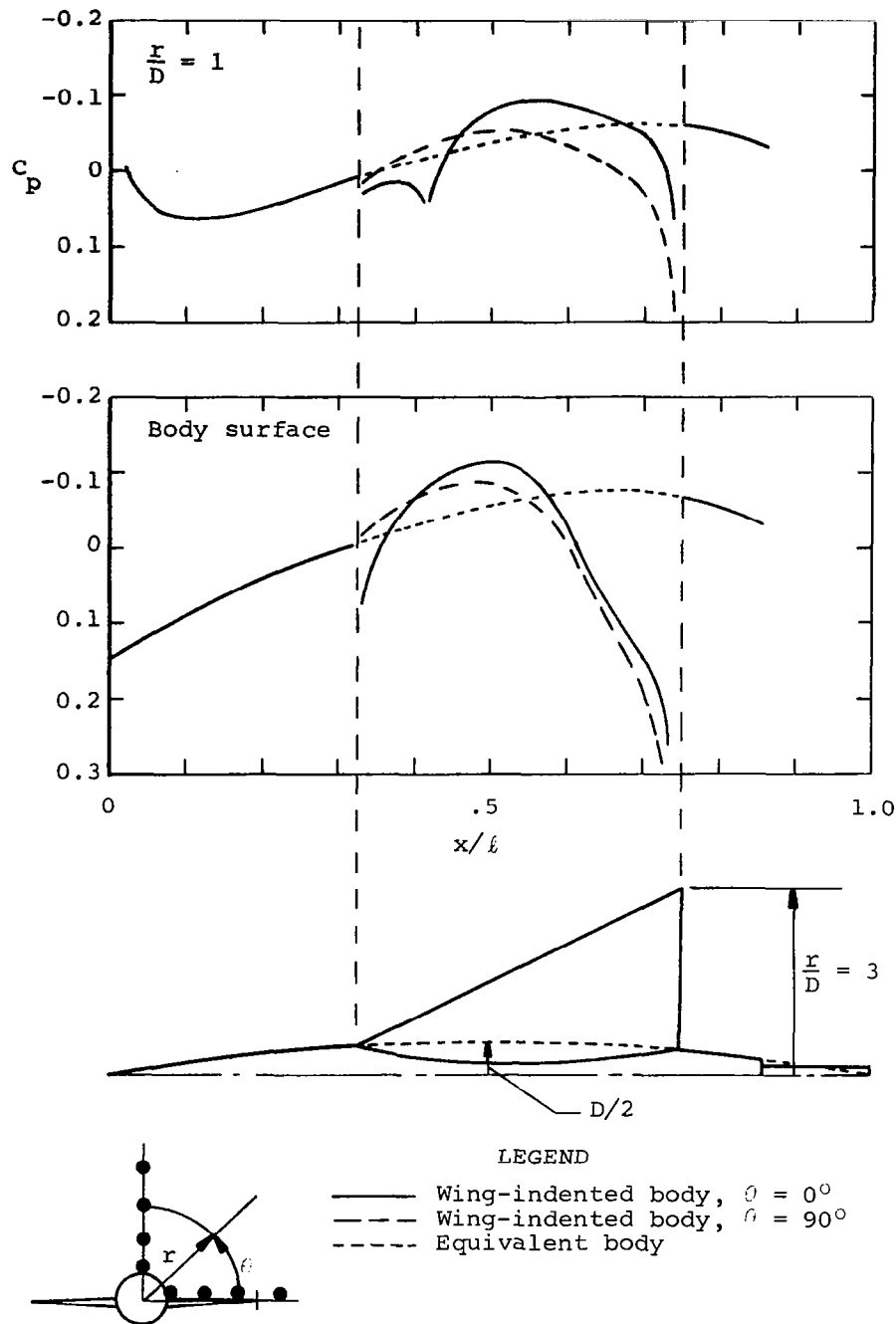


Figure 6.- Theoretical surface and flow field pressure distributions at $M_\infty = 0.80$ (purely subsonic flow) for a nonlifting parabolic-arc profile wing--indented parabolic-arc body combination; equivalent body thickness ratio $D/\ell = 1/12$, wing aspect ratio $AR = 2$, thickness/chord ratio $t/c_w = 0.04$, and with $X_{r/\ell e}/\ell = 0.25$, $X_{r/\ell e} = 0.75$, $X_{b/\ell} = 0.86$.

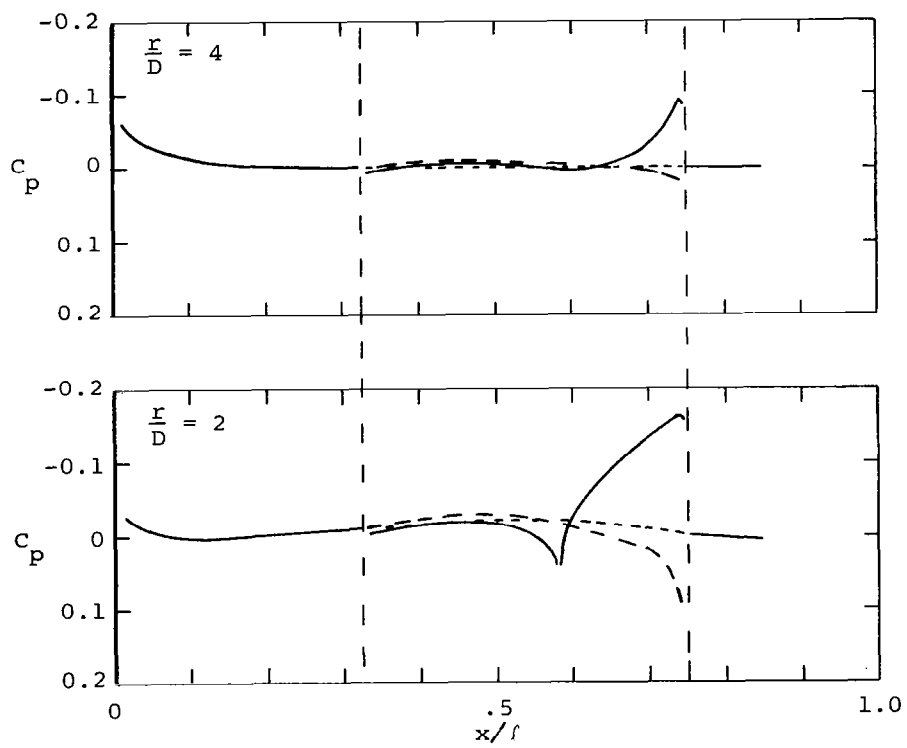


Figure 6.- Concluded

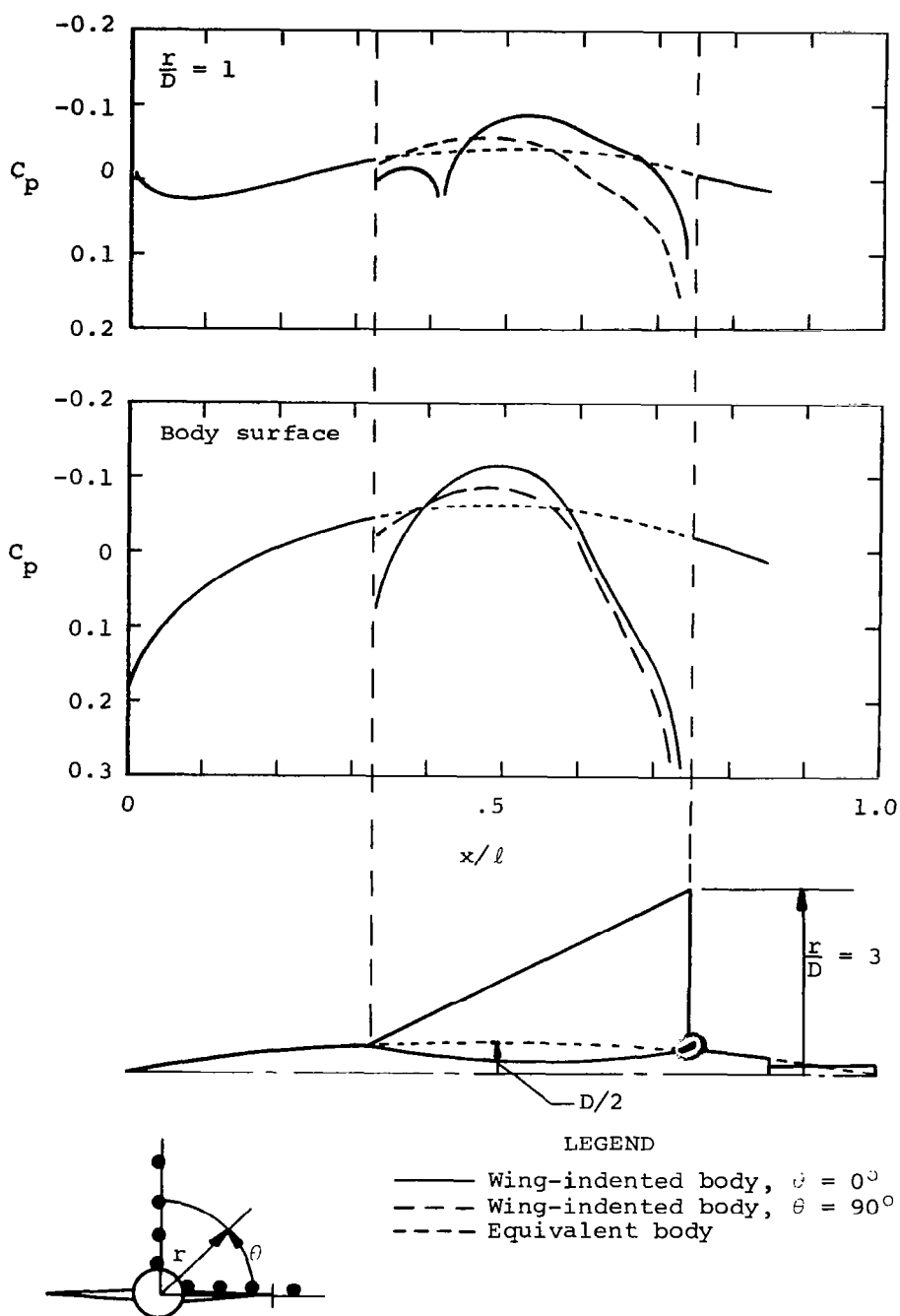


Figure 7.- Theoretical surface and flow field pressure distributions at $M_\infty = 1.20$ (purely supersonic flow) for a nonlifting parabolic-arc profile wing--indented parabolic-arc body combination; equivalent body thickness ratio $D/\ell = 1/12$, wing aspect ratio $AR = 2$, thickness ratio $t/c_w = 0.04$, and with $X_{rle}/\ell = 0.25$, $X_{rte}/\ell = 0.75$, $X_{b/\ell} = 0.86$.

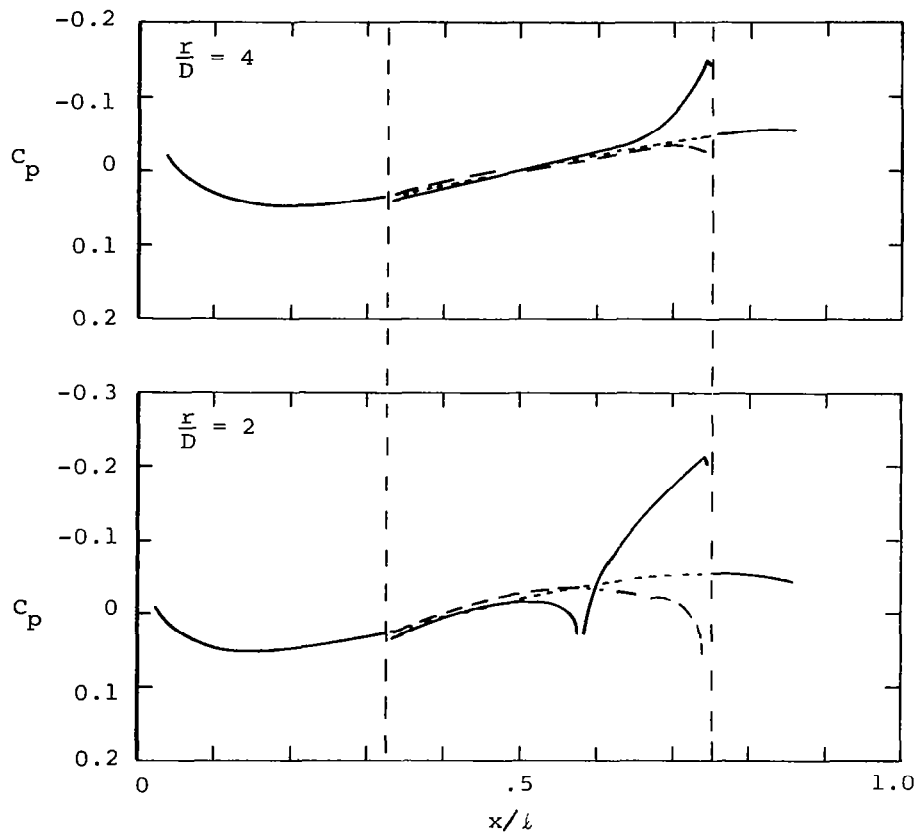


Figure 7.- Concluded.

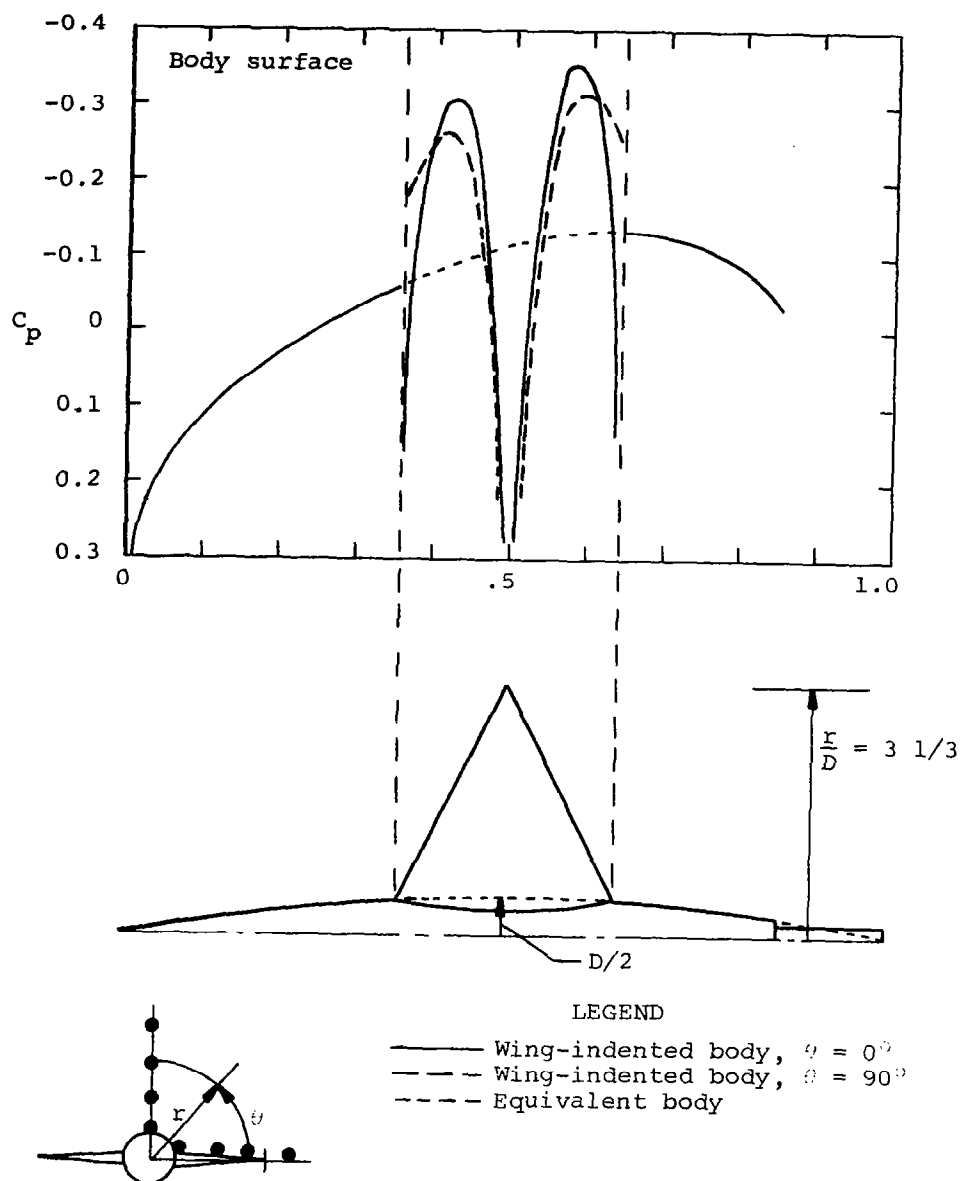


Figure 8.- Theoretical surface and flow field pressure distributions at $M_\infty = 1.0$ for a nonlifting parabolic-arc profile wing-indent parabolic-arc body combination; equivalent body thickness ratio $D/\ell = 1/12$, wing thickness ratio $t/c_w = 0.04$, and with $\beta_{le} = \beta_{te} = \tan^{-1}(.5)$, $x_{rle}/\ell = 1/3$, $x_{rte}/\ell = 2/3$, $x_{b/\ell} = 0.86$.

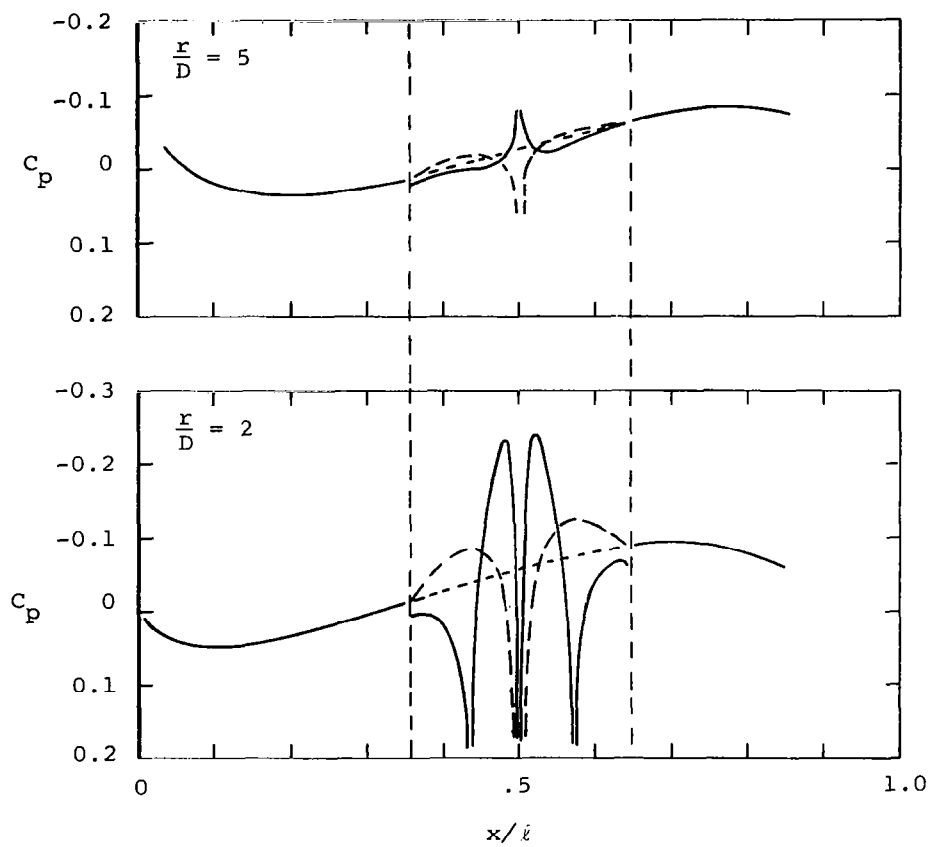


Figure 8.- Concluded.

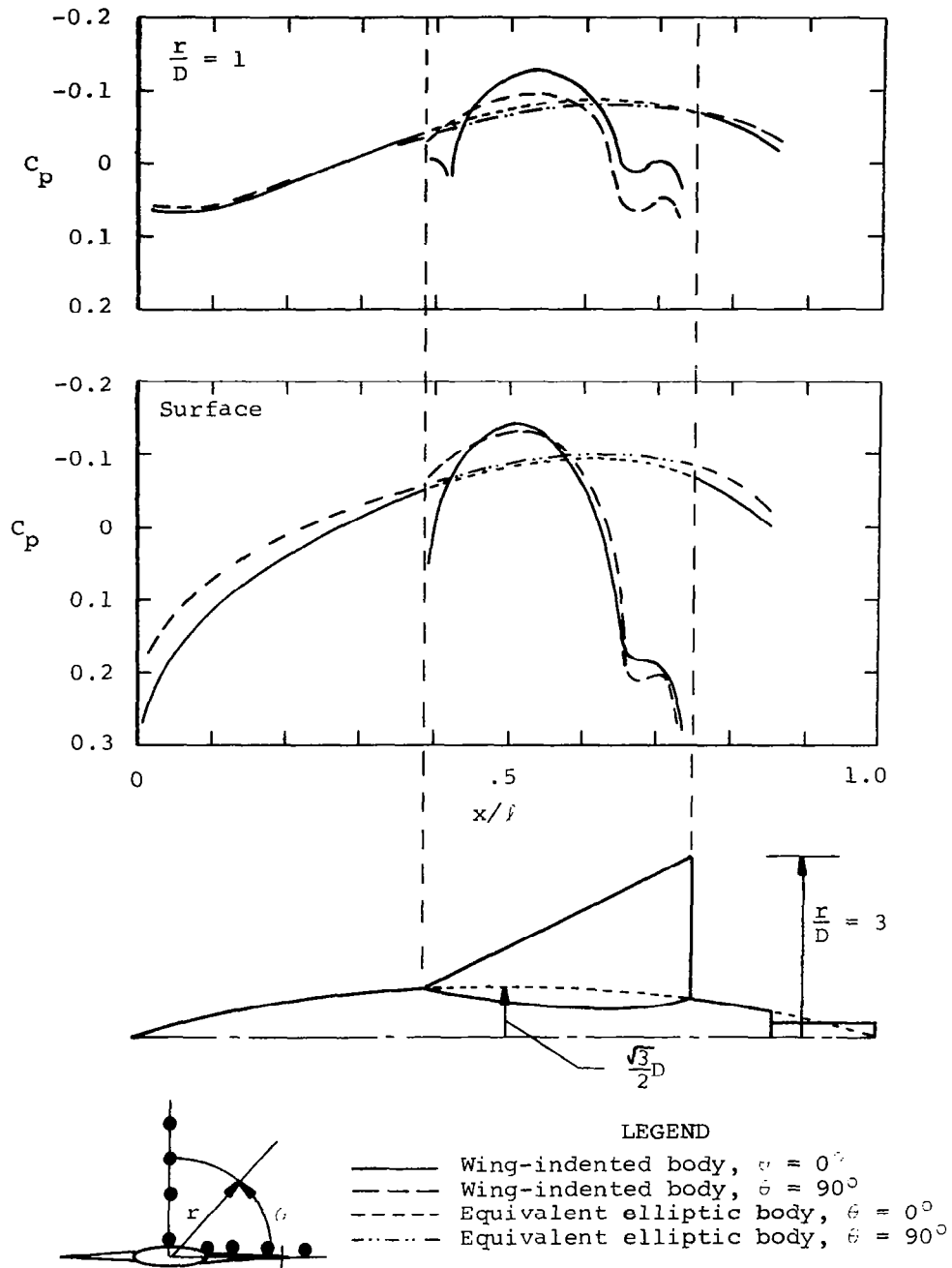


Figure 9.- Theoretical surface and flow field pressure distributions at $M_\infty = 1$ for a nonlifting parabolic-arc profile wing-indentated parabolic-arc body combination; having a body of elliptical cross section with $\lambda = 3$; equivalent body thickness ratio $D/l = 1/12$, wing aspect ratio $AR = 2$, thickness ratio $t/c_w = 0.04$, and with $X_{rte}/l = 0.25$, $X_{rte}/l = 0.75$, $X_{b/l} = 0.86$.

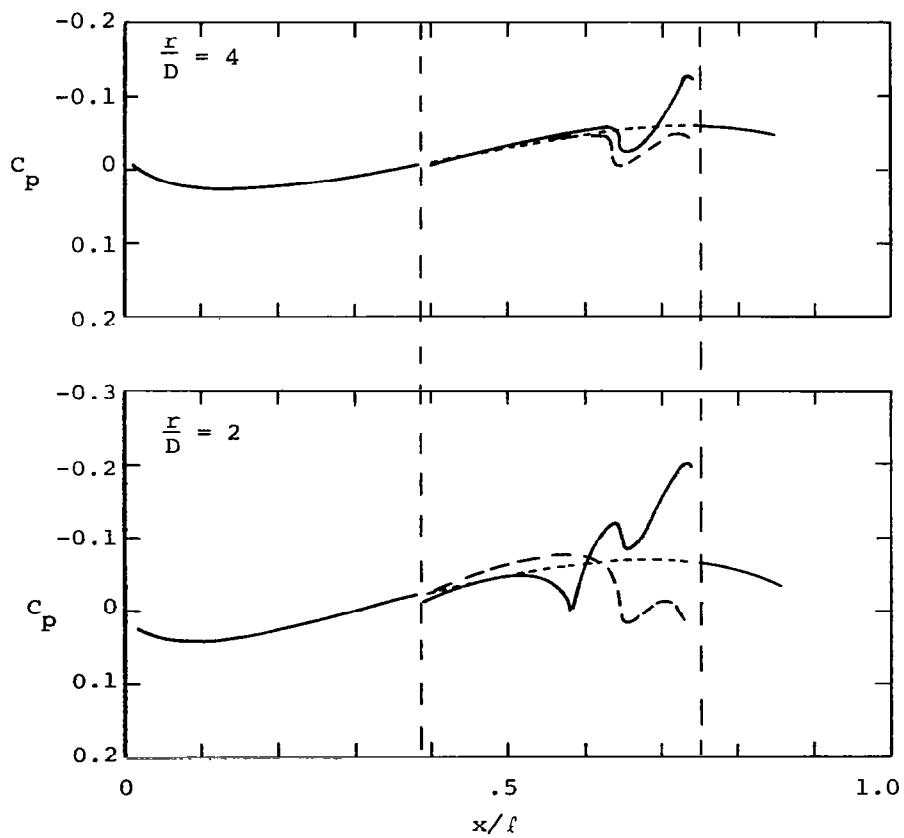


Figure 9.- Concluded.

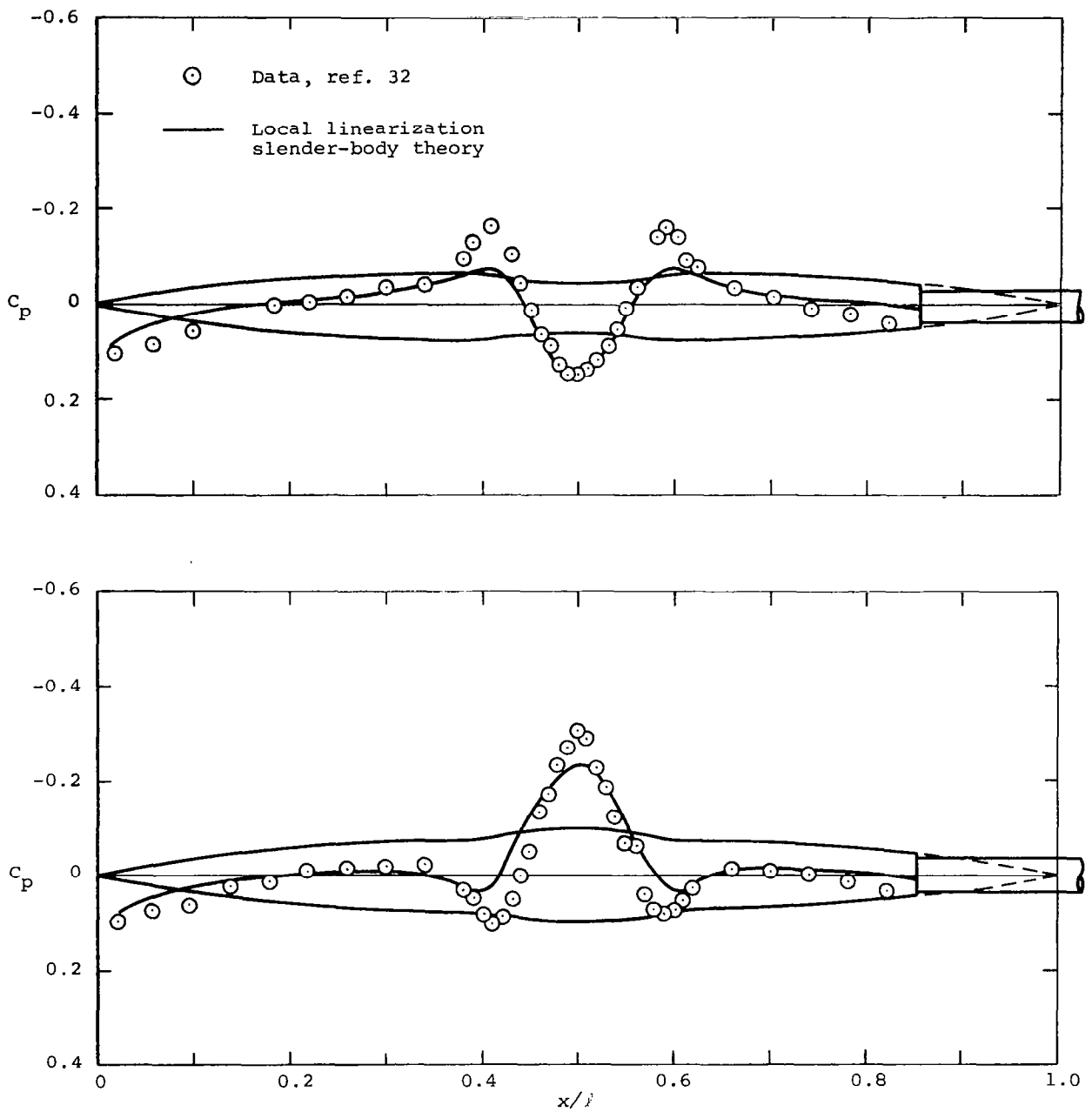


Figure 10.- Theoretical and experimental surface pressure distributions at $M_\infty = 0.80$ on a bumpy and indented parabolic-arc body of revolution; basic body thickness ratio $D/l = 1/14$, maximum distortion height $\Delta R_{\max}/l = 1/70$.

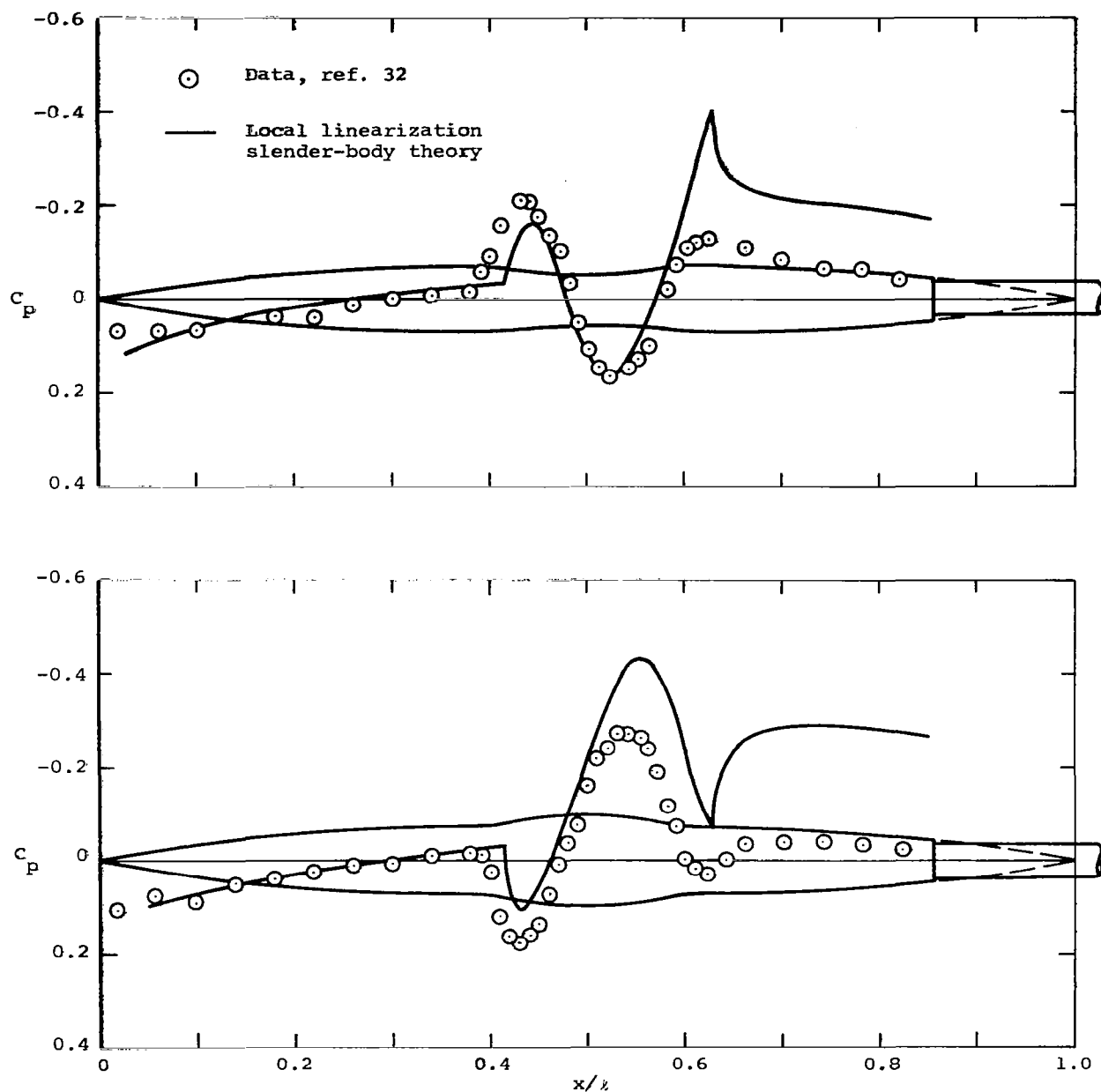


Figure 11.- Theoretical and experimental surface pressure distributions at $M_\infty = 1.20$ on a bumpy and indented parabolic-arc body of revolution; basic body thickness ratio $D/l = 1/14$, maximum distortion height $\Delta R_{\max}/l = 1/70$.

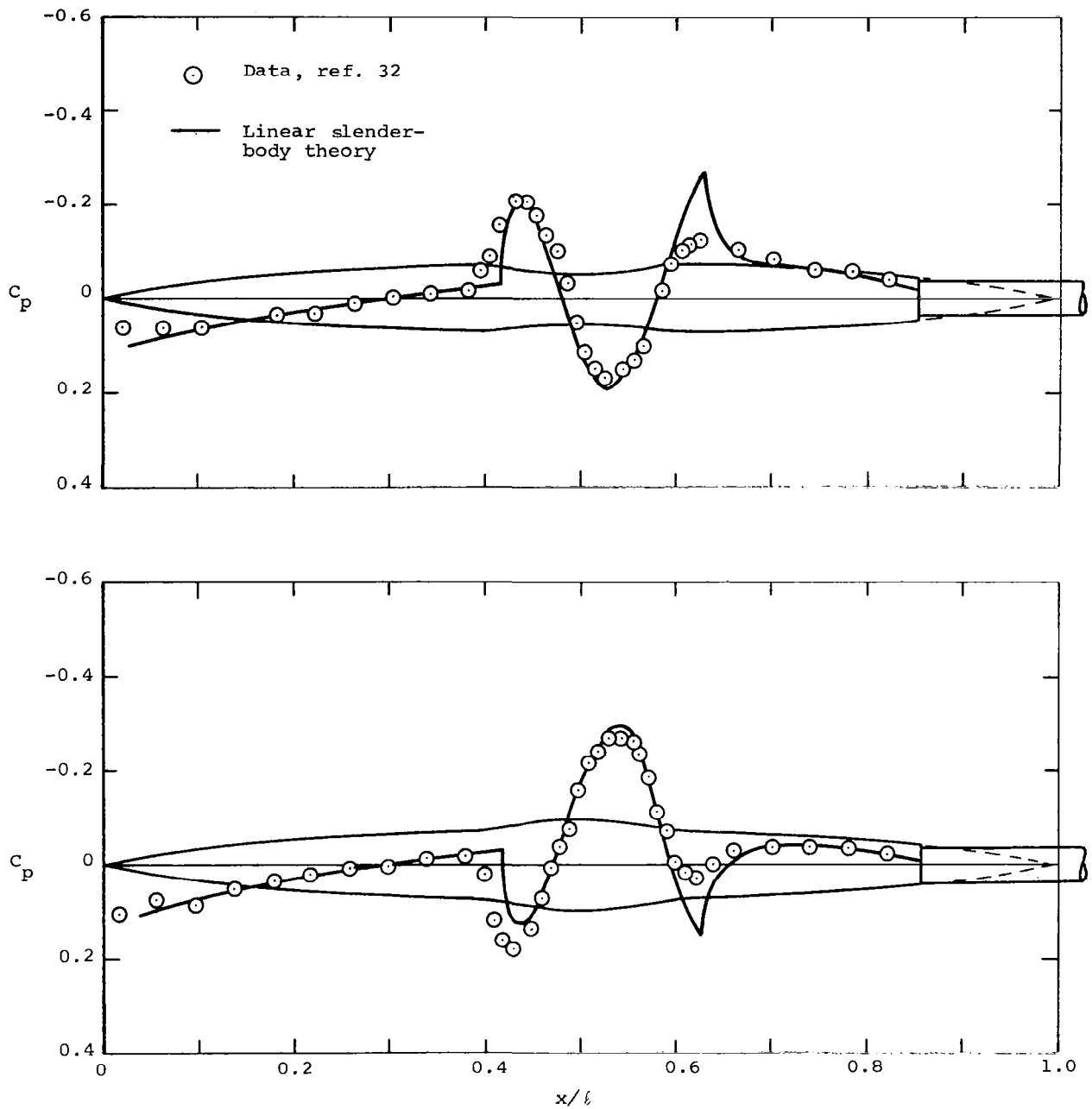


Figure 12.- Theoretical and experimental surface pressure distributions at $M_\infty = 1.20$ on a bumpy and indented parabolic-arc body of revolution; basic body thickness ratio $D/i = 1/14$, maximum distortion height $\Delta R_{\max}/i = 1/70$.

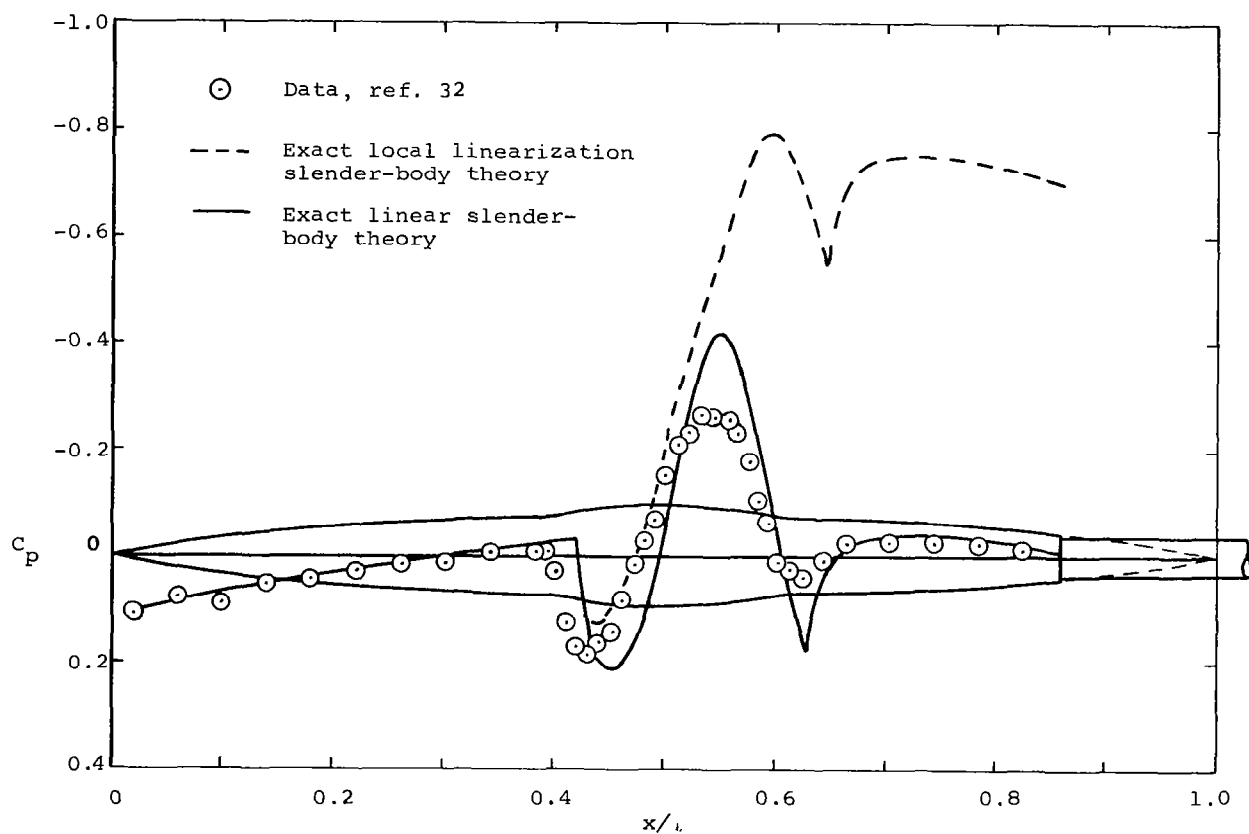


Figure 13.- Theoretical and experimental surface pressure distributions at $M_x = 1.20$ on a bumpy parabolic-arc body of revolution; basic body thickness ratio $D/l = 1/14$, maximum bump height $\Delta R_{max}/l = 1/70$.

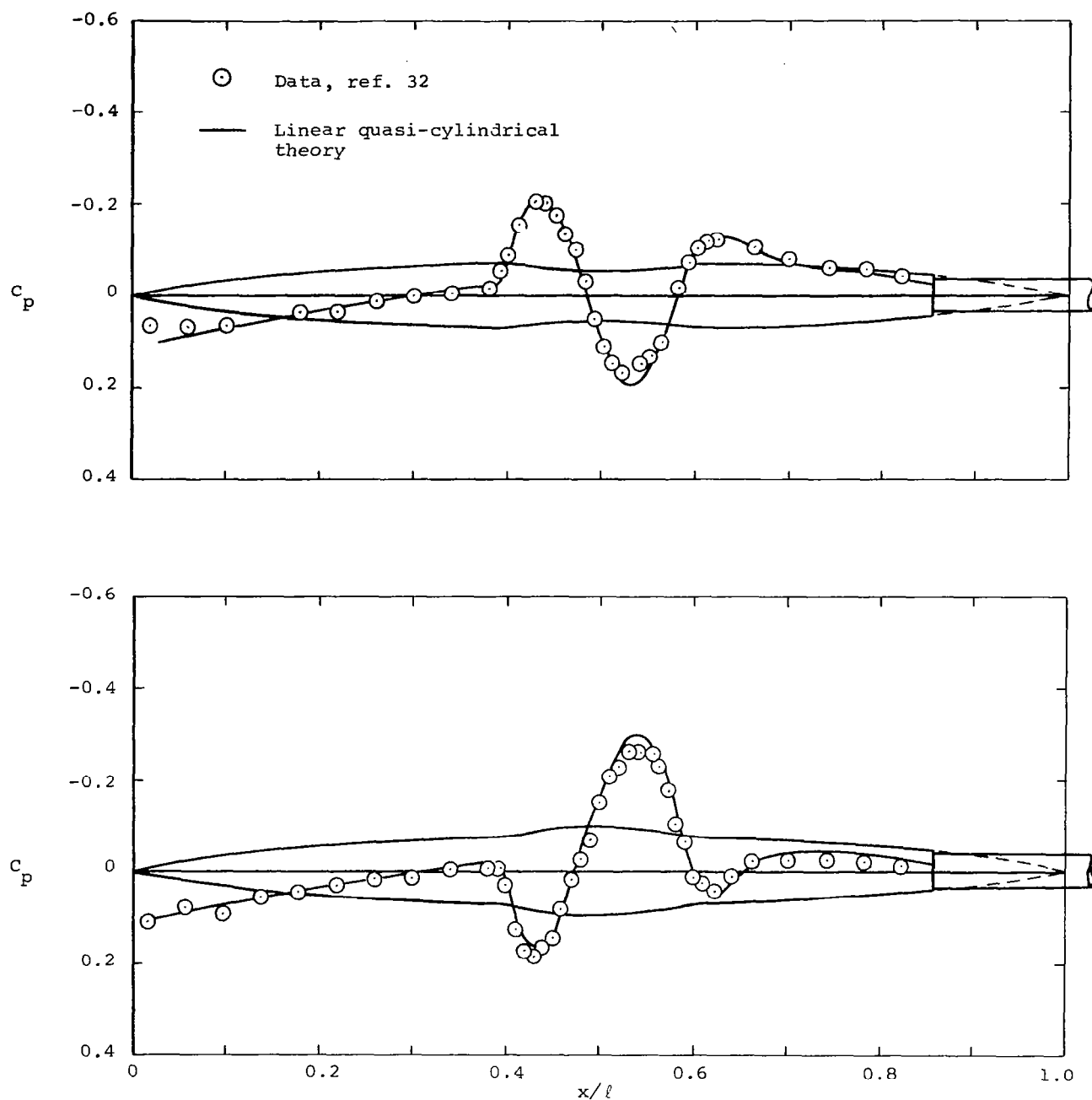


Figure 14.- Theoretical and experimental surface pressure distributions at $M_\infty = 1.20$ on a bumpy and indented parabolic-arc body of revolution; basic body thickness ratio $D/\ell = 1/14$, maximum distortion height $\Delta R_{\max}/\ell = 1/70$.